SAINT PETERSBURG STATE UNIVERSITY

Daria Magomedova

FRACTURE REGULARITIES OF THE ALLOY OF THE AL-MG-SI SYSTEM IN THE COARSE-GRAIN AND ULTRAFINE-GRAIN STATE

Scientific specialty 1.1.8 - Solid Mechanics

Dissertation is submitted for the degree of candidate physical and mathematical sciences

Translation from Russian

Scientific supervisor:
Doctor of Physical and Mathematical Sciences
Dmitry V. Gunderov

Saint Petersburg
2023

CONTENS

INTRODUCTION

Relevance of the research topic

The modern world's dynamism and the development of its various disciplines, such as heavy and light industry, aircraft engineering, electrical engineering, etc., necessitate a broader application of aluminum alloys. Due to the combination of the following material properties, aluminum alloys are of great importance: high conductivity, corrosion resistance, technological ductility, high specific strength, heat resistance, etc. [1] After hardening and aging, alloys of the Al-Mg-Si system used in industry have a high level of technical performance [2]. The alloy grade 6101 is included in this composition. This alloy wire segment used in Russian manufacturing is an innovative import-substituting product designed to produce wire for electrical and other applications. The improvement of the properties of these materials is one of the most important areas of modern materials science because these alloys are a crucial technical component in numerous product sectors [3].

In addition to quenching and aging, a variety of SPD techniques [4-6] are used to enhance the properties of metallic materials. SPD techniques are distinguished by a high degree of modification to the material's structure, phase composition, and physical and mechanical properties. A significant increase in the strength properties of the materials while maintaining their plasticity is an essential characteristic of these methods. SPD techniques include Equal Channel Angular Pressing (ECAP), ARB (Accumulative Bonded Rolling) combined with solid welding, all-round forging, the "twist" process, shear drawing, and shear rolling [7]. The ECAP procedure [8] was the most practical way to produce experimental ultrafine-grained (UFG) samples. Numerous modern studies on the properties of aluminum alloys, including alloy 6101, derived by SPD, and ECAP, indicate that the application of these techniques improves the strength properties [9–15]. The characteristics of mechanical behavior and fracture character during static experiments of UFG alloy 6101 obtained by SPD methods have, however, been little studied up to this point.

The fracture process of coarse-grained materials under static loading has been investigated in sufficient depth and continues to be supplemented by additional data describing the material's behavior on the micro- and macroscales [16]. Less thoroughly

investigated is the fracture process of UFG alloys, including the stage of fissure formation within the material when the strength limits have been exceeded but the fracture has not yet occurred. For a more complete description of the properties of UFG materials, it is necessary to examine material behavior at this stage of fracture. **The objective** of the present research is to examine the fracture behavior of the Al-6101 UFG alloy and compare it to the fracture behavior of the Al-6101 alloy following standard procedures, , in its CG condition.

To achieve the goal of the study, the following **tasks** were set:

1. Investigation of the mechanical behavior of Al 6101 alloy specimens with various structures: after artificial aging and in the UFG state.
2. Numerical modeling of the stress-strain state of Al 6101 specimens under static tension.
3. A research investigation of the fracture characteristics of Al-6101 alloy specimens in the CG and UFG states.
4. An investigation of the structure along the length of specimens after tension to varying degrees of deformation to disclose the moment of pore/crack initiation as the initial stage of the fracture process.

Scientific novelty this study is:

1) The true strains before failure and the true stress of fracture under tension are determined σ_{true} for alloy 6101 in various states, including UFG; and it is shown that σ_{true} in the UFG state is much higher than the true fracture stress in the CG state, and the true strains before fracture are close in all states.

2) Proposed explanation for growth true fracture stress of samples during grain refinement based on the compilation of the Hall-Petch law and the Zener-Strote model.

3) It has been established that in the CG state after artificial aging, Al-Fe particles are the areas of predominant pore nucleation and subsequent destruction, while in the UFG state these particles do not play the main role in the formation of pores.

4) The first stage of the destruction process begins at deformation $\varepsilon \approx 40\%$, this corresponds to the true deformation $e^* \approx 0.7$, in the CG and UFG states.

5) It is shown that the impact of the method of equal-channel angular pressing according to the "Comform" scheme (ECAP-C) according to the selected modes leads

to the grinding of Al-Fe particles: in the CG state, the particle sizes are up to 7 μm, in UFG - up to 2 μm.

Practical and theoretical significance of the work:

The results of the work are of great theoretical significance, since they can be used to describe the process of destruction of alloys of the Al-Mg-Si system. The paper proposes a mechanism for increasing the true fracture stress of UFG alloys. The generalization of these data will make it possible to create new fracture models and refine existing ones, taking into account the structure of alloys. The results of the work are of great practical importance, since they can be used to obtain strong aluminum alloys with high electrical conductivity.

A model is proposed to explain the increase in the true fracture stress of the UFG alloy, which can be used to analyze the mechanical properties of other alloys in the UFG state.

Provisions for defense:

1. The true fracture stress of the 6101 alloy in the UFG state, with a grain size of 500 nm, obtained by ECAP-C according to the selected modes, is 50% higher than the true fracture stress of the alloy in the coarse-grained state after artificial aging, and the true deformations before fracture in both states are close.
2. The true fracture stress of samples during grain refinement is explained on the basis of the compilation of the Hall-Petch law and the Zener-Strote model: with a decrease in grain size, a greater external stress is required to set the flow of dislocations.
3. The first stage of the process the destruction phase - the appearance of pores - begins at strain values $\varepsilon^* \approx 40\%$, which corresponds to the true strain $e^* \approx 0.7$ for CG and UFG states.
4. In the zone near the fracture region, after static mechanical tension, pores with a size of 1–2μm, in samples in the short-circuit state - 3-7 μm.

Reliability and reliability of the obtained results:

The high level of quality and reliability of the presented results is ensured using a combination of physical methods for studying the microstructure of the material, a good correlation of experimental results on changes in physical and mechanical properties with theoretical estimates of the presented material.

The reliability of the obtained results is also confirmed by the publication of research results in peer-reviewed scientific journals from the list of VAK included in the IDB (international databases), Scopus and WoS, as well as the presentation of the data obtained at thematic conferences.

Applicant's personal contribution:

The applicant was directly involved in the discussion and setting of research objectives, obtaining, and analyzing the results, writing articles. She personally conducted sample preparation of materials, mechanical experiments, and theoretical calculations, participated in the processing of SEM analysis data.

About sample processing ECAP-C was held at ISPMS USATU (Ufa State Aviation Technical University) by a group of prof. Raaba G.I.

Approbation of work.

The main provisions and results of the dissertation work were presented at the following conferences:11/27/2018 – 11/29/2018, Moscow, Russian Federation, Fourth interdisciplinary scientific forum with international participation "New materials and advanced technologies"; 01/29/2018 - 02/02/2018, St. Petersburg, Russian Federation,Eighth Polyakhov Readings: International Scientific Conference on Mechanics;07/09/2018 - 07/12/2018, Paris, France, international scientific conference THERMEC 2018; 09/25/2019 - 09/27/2019, Ufa, RF The Sixth International Symposium "BULK NANOMATERIALS: from fundamentals to innovations. BNM-2019"; 1.10.2019 - 6.10.2019, Dilijan, Armenia, international scientific conference TOPICAL PROBLEMS OF CONTINUUM MECHANICS; 9.10.2019 -11.10.2019, Belgorod, Russian Federation, School of Young Scientists "Structure and properties of high-entropy alloys"; 10/14/2020 - 10/16/2020, Belgorod, Russian Federation, International Conference and School of Young Scientists "Obtaining, structure and properties of high-entropy materials"; 03/22/2021 - 03/25/2021 Ufa, Russian Federation, V International Scientific and Technical Conference "MAVLYUTOV READINGS"; 05/17/2021 - 05/20/2021, Yalta, Russian Federation, international scientific-practical conference "Materials science, forming technologies and equipment 2021";09/04/2021 - 09/08/2021, Tsaghkadzor, Armenia, international scientific conference VII INTERNATIONAL CONFERENCE ON TOPICAL PROBLEMS OF

CONTINUUM MECHANICS;26.09.2022-30.09.2022,Chernogolovka, Russian Federation, IV International School-Conference "Promising high-entropy materials"; 3.10.2022-7.10.2022 Ufa, Russian Federation, open school-conference of the CIS countries "Ultrafine-grained and nanostructured materials"

On the topic of the dissertation work, 14 scientific articles were published, two are in peer-reviewed publications from the list of the Higher Attestation Commission of the Russian Federation, 9 - in Scopus / WoS collections:

1. Polyakov, A.V. Influence of grain boundary misorientations on the mechanical behavior of a near-α Ti-6Al-7Nb alloy processed by ECAP // Polyakova V.V., Semenova I.P., Polyakov A.V.,Magomedova D.K., Huang Y, Langdon T.G.// Materials Letters. 2017. 190(4). pp 256-259 DOI 10.1016/j.matlet.2016.12.083.
2. Magomedova, D.K., Churakova, A.A., Stress distribution in static tension of cylindrical samples from ultrafine- and coarse-grained aluminum alloy 6101 // Nanoindustriya. 2021. Issue 1. DOI10.22184/1993-8578.2021.14.1.30.34.
3. Gunderov, DV True fracture stress of UFG samples of Al 6101 alloy / Gunderov DV, Gunderova SD, Magomedova DK // Letters on Materials. 2022.12(4s). pp. 24-427DOI10.22226/2410-3535-2022-4-424-427.
4. Magomedova, DK Influence of grain size and second phase particles on the process of void initiation / Magomedova DK, Murashkin, MY// Journal of Physics: Conference Series. 2018.991.1.012055.DOI10.1088/1742-6596/991/1/012055.
5. Magomedova, DK Technique development for conducting mechanical tests to study the pore formation process in case of material fracture / Magomedova DK, Efimov MA, Murashkin, MY //AIP Conference Proceedings. 2018. 1959. 070021 DOI10.1063/1.5034696.
6. Magomedova, D.K. INFLUENCE OF GRAIN SIZE ON THE PROCESS OF PORE FORMATION IN AL-6101 / Magomedova D.K. // COLLECTION OF MATERIALS "FOURTH INTERDISCIPLINARY SCIENTIFIC FORUM WITH INTERNATIONAL PARTICIPATION "NEW MATERIALS AND PERSPECTIVE TECHNOLOGIES"". 2018. Volume 1. P. 319-321.
7. Magomedova, D.K. INVESTIGATION OF THE MECHANICAL PROPERTIES OF COARSE- AND FINE-GRAINED AL-6101 UNDER STATIC STRETCHING /

Magomedova, D.K., Efimov, M.A., Ryabokon, D.V. // Technical program and theses of the school of young scientists " STRUCTURE AND PROPERTIES OF HIGH-ENTROPY ALLOYS AND COATINGS". 2019 . C.43-44.

8. Magomedova, DK Mechanical behavior of coarse- and fine-grained Al-6101 samples of different geometry under tension / Magomedova DK, Gunderov, DV, Efimov, MA // IOP Conference Series: Materials Science and Engineering. 2019.672.DOI10.1088/1757-899X/672/1/012037.

9. Magomedova, DK Critical stresses determination in case of pores formation for coarse and ultra-fine grained Al-6101 under static tension / Magomedova DK, Efimov, MA, Churakova, AA, Ryabokon, DV, Gunderov, DV // Journal of Physics: Conference Series. 2020. 1474. 012027. DOI10.1088/1742-6596/1474/1/012027.

10. Magomedova, D.K. Influence of geometry and grain size on the mechanical properties of Al 6101 under static tension of cylindrical samples / Magomedova D.K. // materials. technologies. Design, Ufa. Volume 3. No. 2(4). C.20-24.

11. Magomedova, DK The dependence of mechanical properties of Al-6101 alloy on geometry of the samples with a groove during tensile tests / Magomedova DK, Gunderov DV , Mavlutov AM //Journal of Physics: Conference Series. 2021. 1967(1). 012023.DOI10.1088/1742-6596/1967/1/012023.

12. Magomedova, D.K. Study of the mechanical properties and fracture surface of Al-6101 cylindrical specimens under static tension / Magomedova, D.K., Churakova, A.A., Gunderov, D.V. // Proceedings of the VII International Conference "Actual Problems continuum mechanics". 2021. pp.167-171.

13. Magomedova, DK Investigation of mechanical properties and fracture surface of cylindrical samples Al-6101 under static tension / Magomedova DK, Churakova AA, Gunderov DV // Journal of Physics: Conference Series. 2022.012023.DOI10.1088/1742-6596/2231/1/012018.

14. Magomedova, D.K. Influence of the Al 6101 alloy structure on the formation of pores during static tension as a structural change during deformation / Magomedova D.K. // materials. technologies. Design, Ufa. 2022. Volume 4. No. 1(7). C. 24-29.

The structure and scope of the dissertation.

The dissertation consists of an introduction and 5 chapters, a conclusion, a list of references, is presented on 103 pages and contains 52 figures and 13 tables.

Communication with scientific projects.

The author conducted dissertation research at the Research Laboratory of Mechanics of Massive Advanced Nanomaterials for Innovative Engineering Applications of St. Petersburg State University and at the Laboratory "Dynamics and Extreme Characteristics of Advanced Nanostructured Materials" of St. Petersburg State University.

The research was carried out within the framework of the RSF Grant 17-19-01311 "Development of principles for obtaining aluminum-based nanostructured conductive materials with enhanced mechanical properties" (2017-2021) and with the support of Megagrant (Agreement 075-15-2022-1114 dated June 30, 2022)

Material structure studies by SEM methods were carried out at the Interdisciplinary Resource Center in the direction of "Nanotechnology" of St. Petersburg State University.

The manufacture of samples for mechanical testing was carried out at the Center for Applied Aerodynamics of St. Petersburg State University.

The author expresses his deep gratitude to Ph.D. Murashkin M.Yu. (UUNiT) Ph.D. Bobruk E.V. (UUNiT), Dr. of Phys. and Math. Sciences Resnina N.N. (St. Petersburg State University) and Dr. of Phys. and Math. Sciences Atroshenko S.A. (St. Petersburg State University) for practical assistance in the work and fruitful discussion of the results.

Chapter 1. Literature Review

Aluminum (Al) is one of the most common elements in our world, its content in the earth's crust is approximately 8.8%. It is not found in its pure form in nature due to its high chemical activity. In the modern world, aluminum alloys are one of the main materials for creating various structures and / or elements in the field of mechanical engineering, aircraft industry, energy, etc. [1]. Aluminum alloys are highly valued for their performance properties (resistance to atmospheric corrosion, good electrical conductivity, technological ductility, etc.) [1]. Modern technology is actively developing, as a result, the requirements are increasing and the quality of alloys is improving. Al is the mostcommon from non-ferrous metals, if measured by the scale and volume of production. Al has a fairly high latent heat of fusion, relatively low density and low melting point (658°C) [1]. This metal has a high thermal conductivity and electrical conductivity, perfectly formed. It is characterized by high corrosion resistance both in air and in other media. Aluminum alloys are widely used as conductor materials [1].

Conductive Al alloys also have a disadvantage - compared to copper alloys, they have much lower strength. Improving the properties of such materials, as well as finding ways to improve the properties of the material that will be acceptable under the conditions of certain operations, is an urgent task of the modern world. It is possible to achieve an increase in the properties of aluminum alloys in various ways, for example, by alloying with various components, heat treatment and grinding of the material structure [6,17,18].

1.1. Alloys Al-Mg-Si, Al-Fe systems

Initially, alloys of the Al-Mg-Si system contained only Mg and Si, later they were also alloyed with other elements. In the modern world, the components of industrial alloys of this group (AD31, AB, AD33, AD35) are located near the Al-Mg_2Si quasi-binary section and fit within the limits of %: (0.4-1.4) Mg; (0.15-0.6) Cu; (0.3-1.2) Si; (0.5-0.9) Mn; (0.10-0.5) Cr [2]. The Mg_2Si phase is the main hardener in these alloys; it

is this phase that has high strength and hardness. The solubility of this phase is variable and depends on temperature. The Mg/Si ratio in the Mg_2Si phase is 1.73. If this ratio is reduced in the structure in the as-cast state, then Si can be present along with Mg_2Si. The alloys also contain different amounts of Mn, Cr, Cu and Fe; therefore, intermetallics AlFeSi, AlCrFeSi, AlMnFeSi can be present in the structure [19, 20]. If the Mg content is increased, then the strength properties will increase, but the ductility and deformability will decrease [21]. If alloys are alloyed with copper, then it will have a similar effect. To improve the mechanical properties, chromium and manganese are added, which neutralize the harmful effects of iron. That is why it is possible to regulate the ratio between strength and ductility over a wide range, as well as change them due to the degree, method of deformation, as well as the heat treatment mode: σ_v = 150-400 MPa; $\sigma_{0.2}$=60-300MPa; δ=10-30% [21], depending on the composition of the alloys. These alloys are characterized by high corrosion resistance, they are also well welded and susceptible to various coatings. To improve the mechanical properties, chromium and manganese are added, which neutralize the harmful effects of iron. That is why it is possible to regulate the ratio between strength and ductility over a wide range, as well as change them due to the degree, method of deformation, as well as the heat treatment mode: σ_v = 150-400 MPa; $\sigma_{0.2}$=60-300MPa; δ=10-30% [21], depending on the composition of the alloys. These alloys are characterized by high corrosion resistance, they are also well welded and susceptible to various coatings. To improve the mechanical properties, chromium and manganese are added, which neutralize the harmful effects of iron. That is why it is possible to regulate the ratio between strength and ductility over a wide range, as well as change them due to the degree, method of deformation, as well as the heat treatment mode: σ_v = 150-400 MPa; $\sigma_{0.2}$=60-300MPa; δ=10-30% [21], depending on the composition of the alloys. These alloys are characterized by high corrosion resistance, they are also well welded and susceptible to various coatings. depending on the composition of the alloys. These alloys are characterized by high corrosion resistance, they are also well welded and susceptible to various coatings. depending on the composition of the alloys. These alloys are characterized by high corrosion resistance, they are also well welded and susceptible to various coatings.

Alloy 6101 is a medium to high strength grade; has good corrosion resistance; well deformable; heat-strengthened; well-welded (but with low strength in the welding zone); has medium fatigue strength; well formed in the T4 state (natural aging at 20 ºC for at least 8 days after heating for hardening), but is formed to a limited extent in the state T6(hardening with water after heating for hardening at 540 ºC and artificial aging at 175 ºC for 8 hours); this alloy is a complete analog of AD33 alloy (GOST 4784-97) [2,22].

Alloys 6101 are used for the manufacture of electrical wire lines, also in the production of trucks, bicycle frames, passenger cars, structural pipes, car seat frames and bumpers, sports equipment, as well as various structural parts that require increased strength, high corrosion resistance and good weldability.

Mechanical properties of alloy 6101

Normalized mechanical properties are presented in Table 1.1. [23]. The melting temperature range is 575 - 650°C. The standard hardening temperature is 530°C. Heat treatment by artificial aging for rolled and drawn products consists of annealing at 160 °C for 18 hours; - for pressed or forged products - 175 °C for 8 hours.

Table 1.1. Requirements for the mechanical properties of aluminum alloy 6101 according to EN 573-3 [23].

Состояние	Толщина стенки, мм	Предел прочности при растяжении		Предел текучести 0,2 %		Удлинение A
		МПа				%
		мин.	макс.	мин.	макс.	мин.
T4[1)]	≤ 25	180	-	110	-	14
T6[1)]	≤ 5 5 < e ≤ 25	260 260	- -	240 240	- -	9 10
1) Эти механические свойства могут быть получены с применением закалки на прессе						

The hardening of alloy 6101 has certain features that are easy to determine by comparing them with the features of hardening, for example, alloy 6060. Alloy 6060 is an analogue of alloy AD31 (with a minimum content of silicon and magnesium). Figures 1.1 and 1.2. schematically shows the differences in the required cooling rates of the alloys under consideration in order to provide hardening - to create a solid solution of Mg and Si by preventing the precipitation of Mg_2Si particles [2,22,23].

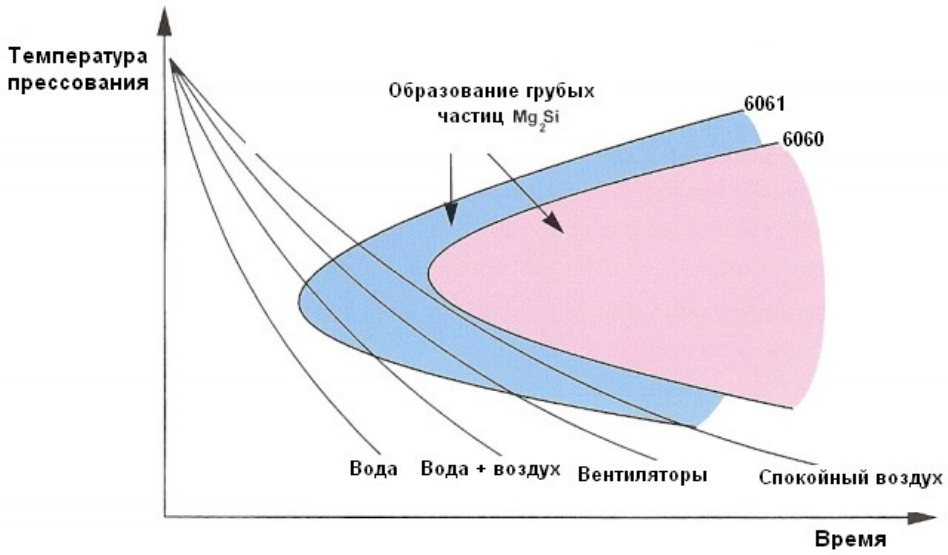

Figure 1.1. Scheme of the required cooling regimes and regions for the precipitation of Mg_2Si particles (alloys 6060 and 6101) [22].

Figure 1.2. Scheme of separation of particles of alloy 6101 of different phases during aging (t, min - T, °) [23].

Iron impurities are present in all Al alloys, the effect of iron must be considered in more detail and this can be done by considering Al-Fe alloys themselves. In industrial iron is up to a few tenths of a percent of the entire composition. It is sparingly soluble in hard aluminum alloys. The solubility of iron is 0.052% (and even less) at

temperatures below 650º C, and at 400-450º C it is practically insoluble. The hardness and tensile strength of the alloys increase due to the heterogenization of the structure by Al-Fe particles, but the ductility decreases sharply. With an increase in the iron content from 0.1 to 0.5%, the corrosiveness of aluminum in an acidic environment increases, and the impact strength also decreases. That is why iron impurities affect the properties of aluminum alloys in a complex way [24].

The FeAl3 intermetallic compound is the second phase in the eutectic in the Al–Fe system; it is released in the form of needles or plates [25]. The Al-Fe phase consists of Fe (40.83%) and Al (59.17%) [24]. The density of the Al-Fe phase is 3.811 kg/m3, its melting point corresponds to 1158ºC, and its microhardness is 9400 MPa.

These alloys have two features that are in demand in electrical engineering. The first is that in order to obtain an alloy where iron will be the main alloying element, it is not necessary to additionally alloy the alloy, because. iron up to 30% is contained in bauxite ore in the form of iron oxide Fe3O3.

The second is good electrical conductivity due to the fact that the alloys of this system almost do not form solid solutions, because iron is practically insoluble in equilibrium at ordinary temperature; its solubility is 0.025 wt.% [26]. Iron also cleans the alloy from silicon impurities, combining it into AlFeSi particles.

Alloys of the Al-Fe system have been actively studied and developed for more than 30 years, and during this time a lot of research has been carried out and many applications based on them have been introduced [23,24,27-29].In some countries, alloys of the Al-Fe system are used as a material for the manufacture of wires in the electrical systems of motor vehicles [27,28]. In addition to Al-Fe alloys, a team of researchers [20] proposed an alloy of the aluminum-iron system modified by zirconium: with an Fe content of up to 0.6 wt.% and a Zr content of up to 0.5 wt.%, it turned out to be much stronger and more ductile.

Structural components, incl. morphology, chemical composition, distribution of intermetallic particles determine the main properties of the alloys of this system, i.e. strength and electrical conductivity. In works [21,30,31], devoted to alloys of these systems, various intermetallic compounds are considered, which go through different cycles of transformations under different material processing conditions: most of the

intermetallic phases are unstable and have a short life span. Various factors, such as the temperature and conditions of melt crystallization [20, 29, 32], determine the types and morphology of the forming phases. The alloy studied in this work was also previously considered in [33], and the presence of Si, Mg, and Fe particles was confirmed.

Silicon in the alloys of the Al-Mg-Si system is characterized by high equilibrium solubility (1.65%) in aluminum at the eutectic temperature. The eutectic passes into a liquid state when the metal is heated for plastic deformation, and this complicates or makes it completely impossible to carry out plastic deformation, since cracks appear on the products during deformation. If the Fe content exceeds the Si content, then it will be possible to avoid the appearance of cracks on the products - then AlFeSi ternary compounds are formed.

1.2. Hardening mechanisms in alloys Al-Mg-Si, Al-Fe systems

There are two main strengthening mechanisms for Al alloys that can become complementary to each other: work hardening and thermal hardening (obtained by aging of the material). The strength characteristics of the alloy in its state after complete annealing are the initial indicator for assessing the possible increase in its strength after thermal and strain hardening. If you increase the content of interstitial atoms in the solid solution of Al alloy, i.e., increase the content of alloying elements, then the strength of the alloy will increase.

For structural materials, strength is evaluated as the resistance to plastic deformation under the condition of constant loads. In the process of volumetric or surface deformation, the metal is strengthened due to the distortion of the crystal structure of the grains, accompanied by an increase in the level of residual stresses. If we consider the dislocation nature of hardening, when dislocations interact with each other, as well as with other defects of the crystal lattice, the lattice distortion increases, and, consequently, the resistance to deformation increases. Excess phases, grain boundaries, dislocations, foreign atoms, and other lattice defects are obstacles to the movement of dislocations.

The main hardening mechanisms that increase the stresses of plastic flows are grouped in modern theories of dislocations as follows [27]: 1) hardening by dissolved interstitial or substitution atoms; 2) hardening by dislocations, hardening by grain and subgrain boundaries; 3) hardening by dispersed particles.

In [34], E. Orovan showed that for a hardened material, the yield strength can be represented by the sum:

$$\sigma_{0,2} = \sigma_0 + \Delta\sigma_{\text{тв.р.}} + \Delta\sigma_{\text{д.у.}} + \Delta\sigma_{\text{д}} + \Delta\sigma_{\text{з}}, \quad (1.2.1)$$

where σ_0 is the friction stress of the crystal lattice, $\Delta\sigma_{\text{тв.р.}}$ is the increase in yield strength due to solid-solution hardening, $\Delta\sigma_{\text{д}}$ is the increase in yield strength due to dislocation, or deformation, hardening, $\Delta\sigma_{\text{з}}$ is the increase in yield strength due to grain-boundary hardening, and $\Delta\sigma_{\text{д.у.}}$ is the increase in yield strength due to dispersion strengthening.

The Peierls-Nabarro stress, which is the frictional stress in the crystal lattice, calculated by the formula:

$$\sigma_0 = [2G/(1-\nu)]\exp[-2\pi/(1-\nu)], \quad (1.2.2)$$

where ν is the Poisson's ratio and G is the matrix shift modulus [43].

The qualitative dependence of the plastic flow stress on the dislocation density is described by the following formula:

$$\Delta\sigma_{\text{д}} = \alpha m G b\sqrt{\rho_{\text{д}}}, \quad (1.2.3)$$

where α is the inter dislocation interaction parameter, m is the orientation coefficient, is G the shear modulus of the matrix, and $\rho_{\text{д}}$ is the dislocation density [34].

As mentioned above, grain boundaries are barriers to the movement of dislocations, which is why, with a decrease in grain size, the density of grain boundaries in a polycrystalline material increases, which prevents the development of plastic deformations. Grain boundary hardening is described by the Hall-Petch law:

$$\Delta\sigma_{\text{з}} = k_{\text{з}} d^{-m}, \quad (1.2.4)$$

where $k_{\text{з}}$ is the coefficient of grain boundary strengthening, d- average grain size and m- misorientation angle coefficient.

To increase the strength properties of the material, the distortions of the solid solution lattice are increased by doping the material, heterogenizing the structure, as well as

grinding the grain and excess phases. Therefore, alloys can be strengthened in various ways.

Alloying elements and various impurities that are part of the solid solution have atomic sizes that differ from the atomic size of aluminum, and it is they that can change the forces of interatomic interaction, as well as create regions of elastically deformed states at their locations, which will be an obstacle to dislocation movements. The nature and quantity of these obstacles influence their inhibition. If we consider the nature of alloying elements from the side of their influence on the hardening of alloys, then the main criterion will be the size of the atom itself (the so-called size factor). The higher the difference between the sizes of an aluminum atom and the atoms of other elements, the more perturbations there will be in the crystal lattice, and, naturally, the higher the hardening will be. The greater the amount of solute, the greater will be the amount of distortion of the lattice itself - this is the concentration factor. Qualitatively, the contribution of the size and concentration factors to the strengthening of the alloy solid solution is described by the Mota and Nabarro equation:

$$\sigma_m = \sigma_0 + G_0 \frac{|r_1 - r_i|}{r_0} C_i, \qquad (1.2.5)$$

where σ_0 is the yield strength of the alloy substrate, G_0 is the shear modulus of the alloy substrate, r_0 and r_i are the atomic radii of the substrate and the alloying element, and C_i is the atomic fraction of the alloying element.

By alloying with a solid solution, relatively small distortions of the crystal lattice can be achieved, therefore, the values of the increase in strength are small and equal to 10-30% of the total strength of the base, and the ductility values remain high. That is why, when creating alloys that are easily subjected to plastic deformation, it is advantageous to use solid solutions as the basis of structural materials. The state of the solid solution, as well as the amount of distortion in it, as a result of which the hardening itself can be changed by heat treatment, i.e. solubility of elements in aluminum with temperature change.

If the content of the alloying element is increased and the solubility limit of this element in the volume of the alloy is exceeded, separate inclusions will appear, and their number of inclusions will increase proportionally to the number of alloying elements.

The strength characteristics of the material can increase additively, but they can also decrease, depending on the properties of the inclusions. If the strength of the inclusions is greater than the strength of the solid solution, then the strength of the alloy increases; if the particles are less strong, then the strength of the alloy decreases [34]. In this case, hardening during alloying is of a mechanical nature and cannot be explained by additional changes in the structure of the lattice. The strength is greatly affected by the size of the inclusion - with a large size and a small number of inclusions, large distances between these inclusions are observed. Then each element of the structure is deformed under the action of an external load, and does so independently of each other. Solid inclusions can cause the opposite effect and reduce strength - in this case, these inclusions will be stress concentrators and will initiate the initiation of cracks [20, 29]. At small, nanometer sizes of inclusions, the interaction of these inclusions with the main crystal lattice affects, which increases the distortion of the structure and causes an increase in strength [32].

The increase in yield strength due to precipitation hardening is calculated as follows:

$$\Delta\sigma_{\text{д.у.}} = 0{,}85\frac{\mathrm{Gb}}{\mathrm{l-D}}, \qquad (1.2.7)$$

where b is the Burgers vector,l is the average distance between particle centers and D is the average particle size [34].

1.2.1. Effect of heat treatment on alloys Al-Mg-Si systems

The discovery of the effect of thermal hardening due to the precipitation of Mg2Si particles [1] gave impetus to the development of alloys of this system. Heat treatment, artificial and natural aging give a serious increase in the mechanical characteristics of aluminum alloys of the Al-Mg-Si system [2].

The heat treatment of alloys changes the solubility of various intermediate compounds in the main Al solution [19]. If the temperature is lowered, then the solution will become a supersaturated intermediate compound, separating out as a separate phase. With the help of rapid cooling, it is possible to slow down the procedure for separating the excess phase and, thus, to obtain at ordinary temperature the state of the alloy in which it was previously at high temperatures as if to freeze the process. The

resulting supersaturated solution will have an unstable state in which internal processes will begin to occur over time, as a result of which the mechanical properties of the alloy will change. This process is called aging. [22,23].

Aging is called natural if it takes place at room temperature, artificial - at elevated. The tensile strength of the alloy after aging greatly increases relative to its tensile strength in the freshly quenched and annealed state [35]. The tensile strength of alloys does not noticeably increase in the initial, or incubation, period of aging. In order to give the alloy high ductility, it must again be returned to the freshly quenched state.

Magnesium and silicon form compounds that are soluble in aluminum - for example, Mg2Si, therefore, thanks to them, the alloy is strengthened during heat treatment. If you increase the amount of magnesium in the alloy, then this will lead to a decrease in the ductility of the alloy in the hot state, and also complicate its processing by pressure. Therefore, usually its alloys contain no more than 0.8%. In some alloys, the proportion of magnesium reaches 1.8%, while the technological properties of the alloy deteriorate, but this deterioration is accompanied by an increase in mechanical properties.

If an aluminum alloy contains copper in an amount of 4.5–5.0%, then this leads to an increase in the strength of the alloy. With an increase in its content of more than 5%, a noticeable increase in strength is no longer observed, but plasticity sharply decreases [21,24-26,31].

Hardening and subsequent natural or artificial aging is the most well-known type of heat treatment used in industry. Hardening is carried out at a temperature of 520-530°C. Natural aging occurs at room temperature. This entails an increase in tensile strength and yield strength, as well as an increase in hardness [19]. Natural aging usually proceeds within 5-7 days. Thus, natural aging, compared to the freshly quenched state, gives an increase in tensile strength by 30-40% and an increase in yield strength by about 50%.

To obtain maximum σw and $\sigma_{0.2}$, the alloys are subjected to quenching and subsequent artificial aging. Artificial aging is carried out at a temperature of 160-170°C for 10-12 hours - this gives an additional increase in strength by 30-50%, relative to natural aging.

Heat treatment is based on the effect of increasing the solubility of the Mg_2Si compound in Al with increasing temperature [35]. If the alloy contains up to 1.85% Mg_2Si, it can be brought into a single-phase state by raising its temperature, and this state can be fixed at room temperature by high-speed quenching.

Structural transformations during aging

During aging, aluminum alloys undergo the formation of metastable and then stable phase precipitates, complex processes of rearrangement of atoms in a solid solution, as well as growth, or coagulation, of precipitated phases [35]. The first stage of aging is a rearrangement within a supersaturated solid solution of atoms, which leads to the formation of submicroscopic regions with an increased concentration of magnesium and silicon (Guinier–Preston (GP) zones), which are also called clusters. These zones appear in the form of needles up to 100 A long and 10-20 A in diameter, their density in the matrix is $(2\text{-}5)\cdot10^{15}$ cm $^{-3}$. HP zones are not phase separations. They have a matrix crystal lattice, which is slightly distorted due to the increased concentration of atoms with a radius that differs in size from that of aluminum atoms. There is a coherent relationship between the matrix and band lattices [34]. Solution zones near HP zones are depleted in silicon and magnesium due to diffusion of alloying elements into HP zones. Slow ordering of the HP structure in the form of needles proceeds during natural and artificial aging at low temperatures [34–].

Metastable β'-phases that retain a coherent bond with the matrix lattice are formed only during artificial aging at temperatures above 200ºC. The mechanism of formation of this phase is not yet clear; it is possible that some of the HP zones are rearranged into metastable phases [34].

The HP and β'-phase zones observe a coherent bond with the matrix lattice, their stability is determined by the degree of correspondence between their crystal lattices, and the greater this correspondence, the more stable are the HP and β'-phase zones. Alloying elements affect the aging of the alloy in a similar way: the stability of the HP and β'-phase zones increases and the aging rate decreases if alloying reduces the indicated lattice mismatch [36].

The last stage of solid solution decomposition is the formation of precipitates of the stable Mg2Si phase, which does not have a coherent bond with the matrix lattice. Plates,

not needles, are the equilibrium form of the stable phase. A further increase in temperature or holding time leads to particle growth or coagulation. The particles become larger, which means that their density in the matrix will decrease, therefore, their contribution to hardening will decrease, and the alloy begins to pass into an equilibrium state [18, 36]. If we consider the form of decomposition of a solid solution, then the initial acicular zones become rods, and then precipitates form in the form of plates [35, 36].

Changes in mechanical and physicochemical properties are due to changes occurring in the structure of alloys during aging [49, 50]. Aging is done to a greater extent to increase the strength of the alloy [36,37].

A constant increase in σv and σ0.2, as well as a slight decrease in δ occurs during natural (zonal) aging over time. If the aging temperature increases, then the diffusion mobility of atoms also increases, therefore, the stages of decomposition of a supersaturated solid solution are accelerated and hardening occurs faster.

Hardening appears at the stage of formation of HP zones and metastable β`-phase, while the crystal lattice is distorted, and the alloy is strengthened due to the presence and coherence of HP zones and β`-phases. For hardening, lattice deformation does not play a special role, but the interaction with magnesium and silicon atoms in the β'-phases of dislocations is probably important.

At temperatures above 250ºC, the increase in strength obtained as a result of strain hardening as a consequence of recrystallization disappears, and the strength of this alloy goes into the values of the initial state. The recrystallization temperature depends on the chemical composition of the alloy and the degree of cold plastic deformation, and, upon annealing to its values, the loss of strength is not so significant [36, 37].

Until the end of the 20th century, the selection of aging modes was carried out experimentally, which required large material costs, therefore single-stage aging modes are more common. Multistage regimes increase the strength properties, but require serious experimental efforts, which prevents the introduction of such regimes into production [36, 37]. Thanks to computer simulation, it was possible to significantly reduce the empirical labor intensity. In recent years, the number of works on modeling aging processes has noticeably increased, and not only for the Al-Mg-Si system, but

also for the Al-Li, Fe-C, Ti-Ni, Al-Ni, Cu-Co, Al- Cu, Al-Zn-Mg, Al-Sc, Al-MgGe, Al-Mn-Mg. All these models have limitations: they consider only one hardening phase and use isothermal aging regimes, and this does not take into account the multi-stage process of separation and it is impossible to describe the hardening. Too rough approximations between structural changes and mechanical properties are also used, and this causes a large discrepancy with the experimental results, therefore it is impossible to choose a mode with maximum strength properties.

1.2.2. Effect of Severe Plastic Deformation on Alloys Al-Mg-Si systems

In the last few decades, much attention has been paid to the creation and study of new materials - nanomaterials [4, 38, 39]. Such materials are characterized by unique properties and crystal structure and average grain size up to 100 nm. Methods of severe plastic deformation (SPD) [5, 6] form nanostructures in bulk metal samples by grinding their structure to nanosize due to large deformations occurring at relatively low temperatures under high pressure conditions. The principle of SPD methods is based on the formation of a highly fragmented and misoriented structure with grain sizes up to 100 nm due to large plastic deformations ($\varepsilon \geq 4$-6) [7, 17, 40].

In order to obtain the greatest changes in the microstructure and the maximum increase in strength, the alloys under study must be subjected to preliminary heat treatment before SPD. In addition, this preliminary heat treatment of heat-strengthened alloys after SPD provides additional hardening during subsequent aging due to the precipitation of strengthening nanoscale phases [16, 41].

The SPD method, the initial microstructure of the material, processing modes, chemical and phase composition determine the grain size and the nature of the emerging structure. In order to obtain a nanostructure in bulk blanks, when using SPD methods, a number of requirements must be observed. The main requirement is the ability to form a nanostructure based on high-angle boundaries - HABs, because the change in the properties of metallic materials occurs due to HABs. [5,17,54,56]. It is also necessary that the resulting structure be homogeneous throughout the entire volume of the workpiece - this is a condition for the stability of properties. It is also required that the

original workpiece does not have mechanical damage or destruction. For conventional metal forming techniques, these requirements are not met. To obtain bulk materials with a nanostructure, it is required to use special deformation schemes that make it possible to achieve large plastic deformations for relatively low temperatures [39, 41].

Severe plastic deformationtorsion (SPD) gives the highest structure refinement (grain/subgrain size is approximately equal to 80 nm) among the applied SPD methods[39,41]. The disadvantage of this method is the possibility of obtaining samples of only small geometric dimensions. All-round forging forms a homogeneous structure with equiaxed grains/subgrains, and their size is up to 300–400 nm [19], while the method equal channel angular pressing(ECAP) gives a reduction in grain size to 200 nm, subject to different processing modes [8,16,39,41,42-45].

The ECAP method is one of the promising SPD methods used to obtain a bulk UFG structure of a material [8, 42–46]. The ECAP method was developed by V.M. Segal et al. [5] more than 50 years ago. This method is based on the deformation of massive workpieces by a simple shear. R.Z. Valiev et al. used the method developed by Segal to experimentally obtain UFG structures in the early 1990s [6]. His research became the basis for creating bulk nanostructured materials with improved mechanical and functional properties [6,46.]. The ECAP method is the most common SPD method, which can be used to obtain an UFG structure in a bulk metal billet. The ECAP method is provided by multi-cycle processing by pressing the same workpiece in a tooling with channels intersecting at an angle Φ (Figure 1.2.2.1).

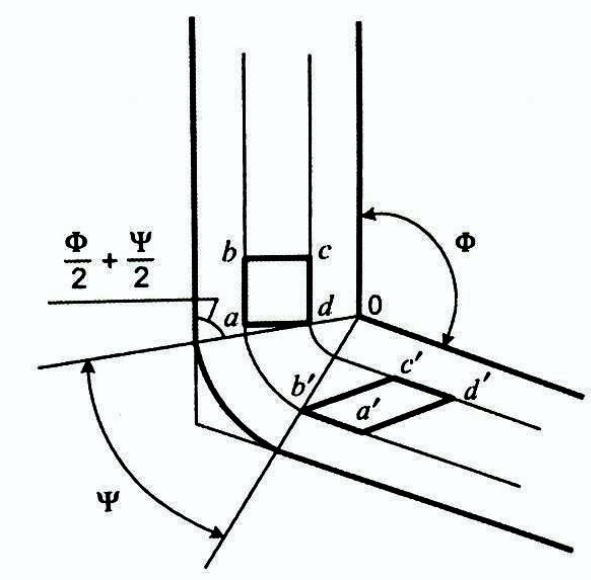

Figure 1.2.2.1 – General scheme of deformation by the ECAP method [46].

When applying the ECAP method, the initial workpiece is deformed according to the simple shear scheme, and deformation occurs under the conditions of a rotational flow of the material, and with a system of acting active and reactive forces (Figure 1.2.2.2). The mechanics of the ECAP process was analyzed and developed by V. M. Segal [8, 44, 45, 47] and also by G. I. Raab and colleagues [18, 38].

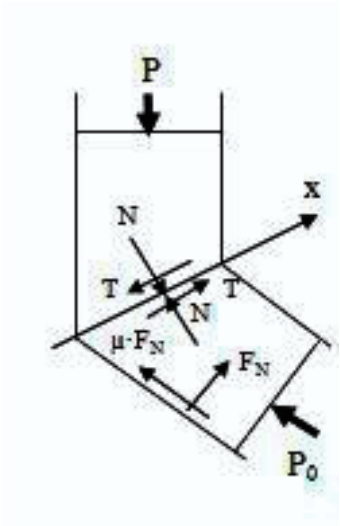

Figure 1.2.2.2. Scheme of acting forces for the ECAP method [46].

The deformation path plays one of the main roles in the formation of an UFG structure in bulk metals when using the ECAP method [18, 43]. The deformation route is a sequence of certain angles of rotation of the workpiece relative to the longitudinal axis between passes through the pressing tooling. Route "A" is determined by turning the workpiece before each subsequent cycle of deformation by an angle equal to 0°, route "B" - by the angle of rotation of the workpiece by 90 °, and route "C" - by 180 ° [8,42-46]. The most efficient route for the formation of an ultrafine-grained structure in the ECAP method is route B[18,43]. Later route B was divided into two varieties: 1) “Ba” is a route with alternate 90 ° turns between cycles to the left (i.e. counterclockwise movement), looking in the direction of movement of the workpiece, and to the right (clockwise movement); 2) "Sun - is determined by turning the workpiece each time only in one direction. The best change in shear planes for non-monotonic deformation in the workpiece is achieved by turning 90º before each subsequent pass. The return effects in this case, for example, Bauschinger, are not strong, and the increase in the dislocation density of the structure at such parameters occurs more actively. If the ECAP method is

nonmonotonic, then there is an increase in the frequency of interfragment shears, and this gives an increase in the contribution of linear and rotational modes to the deformation, and the process of formation of the UFG structure and high-angle boundaries is also enhanced [44]. To ensure uniform and efficient formation of UFG structures in bulk workpieces using the ECAP method, it is necessary to determine a combination of several factors: pressing route, speed and degree of deformation (number of cycles n), processing temperature, geometry and tribological parameters of tooling, where the ECAP process takes place. The traditional ECAP method has been actively developed in recent years. The main directions of this development are an increase in the intensity and efficiency of structure grinding, as well as the application of SPD methods to hard-to-deform materials, the creation of defect-free blanks, an increase in the size of the resulting bulk blanks, the creation of long rods, as well as sheet blanks, the development of the process of obtaining UFG blanks to industrial production [43,46].

Thanks to the ECAP method, it is possible to obtain nanostructured materials with high morphological grain uniformity from massive plastically deformable workpieces. Figure 1.2.2.1 shows how the shear deformation of the sample occurs when it crosses the contact between the channels. During the ECAP cycle (repeating the procedure n times), there will be a systematic increase in deformation, which will lead to a gradual decrease in the grain size - this is due to the formation of a grid, first of low-angle, and then of high-angle boundaries. The ECAP method is also applicable in controlling the crystallographic textures of bulk structural materials.

ECAP-conform method (ECAP-C)

This method has a very significant innovative potential [18]. The ECAP-C method, which also produces blanks in the form of bars and wires with an UFG structure, has some advantages, for example, the ability to make the processing process continuous and use the active friction forces involved in the engraving of the rotor. The scheme is shown in Figure 1.2.2.3 below:

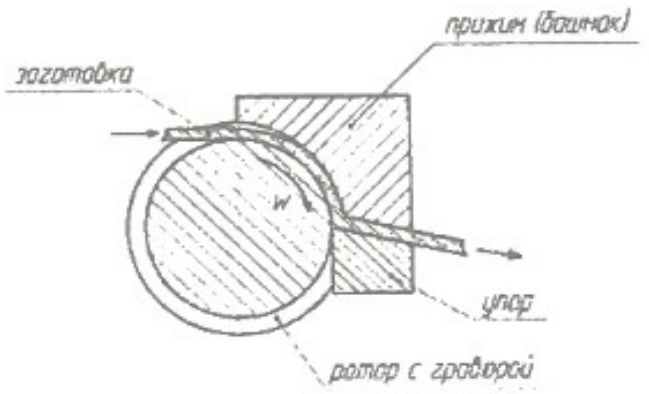

Figure 1.2.2.3. Scheme of ECAP-C [48].

As shown in Figure 1.2.2.3, the original billet in the form of a bar is sent to a part of the plant, where it is processed according to the ECAP scheme. The inlet and outlet channels can be changed according to the required criteria, and this makes it possible to obtain bars of different profiles, it is also possible to change the section according to supplemented requests, and this can be even more harden the material. After one pass in ECAP-Conform [48], the average grain size in commercially pure Al is 0.6–1.1 μm, i.e. Indeed, the method is suitable for obtaining an UFG structure; moreover, the material will be suitable for further deformation processing, for example, by drawing. After studying a large number of aluminum alloys subjected to ECAP-Conform, it was concluded that heat-hardenable alloys have a higher innovation potential, for example, alloys of the Al-Mg-Si system, (6101, 6201, AA6101 ...) [9-12].

There are a number of works devoted to the effect of the ECAP-C method on the 6101 alloy. It was shown in [10] that the formation of an UFG structure in an alloy of the Al-Mg-Si system occurs during continuous processing by the ECAP-Conform method. ECAP-Conform was applied to alloy 6101 on an installation with a channel intersection angle of 130 °C, with the number of cycles n = 6, and this led to a homogeneous UFG structure with a grain size of 400 to 600 nm. Grain refinement during ECAP-Conform is accompanied by dynamic aging, which leads to the formation of metastable spherical particles ranging in size from 3 to 20 nm [10].

In [49], the analysis of electron backscattering diffraction (EBS) was used to study the evolution of the grain structure during ECAP-C of an Al-Mg-Si alloy similar in

chemical composition to alloy 6101. It was shown that an ultrafine substructure is formed after 1–2 passes of ECAP -C, and after four passes, ECAP-C transforms into a UFG microstructure with a predominance of high-angle grain boundaries and saturates during further processing (Figure 1.2.2.4).

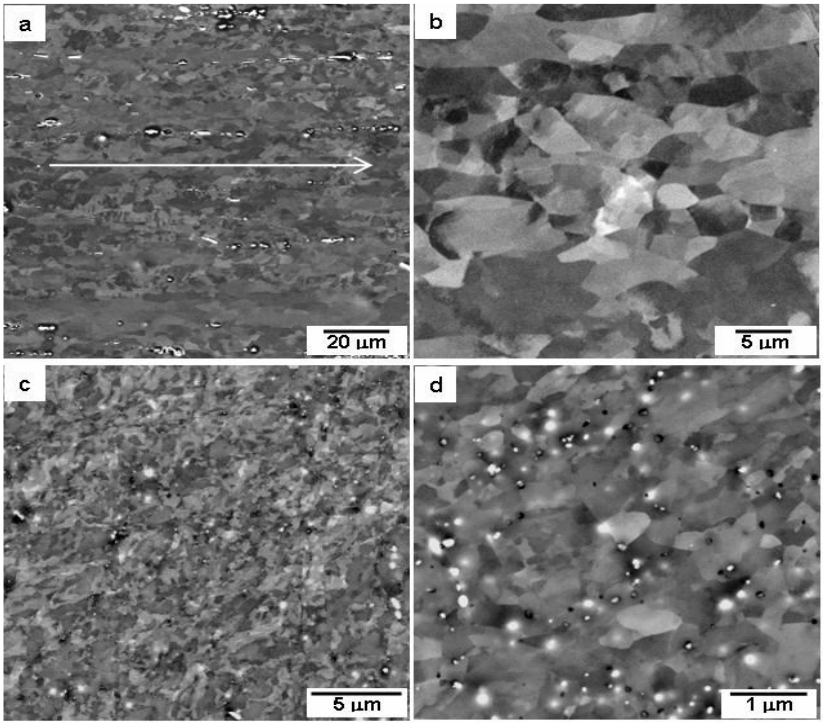

Figure 1.2.2.4. Backscattering electron micrographs of the microstructure of the Al 6101 alloy wire rod: a, b – initial state (T1); and (c, d) after ECAP-C (the arrow indicates the direction of deformation) [10].

There is also a multi-ECAP-C method [46]. the main feature is the joint application of two types of ECAP method: 1) ECAP method in parallel channels (ECAP-PC); 2) ECAP-C. During the passage of one cycle of processing the workpiece by the Multi-ECAP-Conform method, the true deformation e>2.5 is achieved, and a mixed structure is formed, which is elongated subgrains in the direction of shear deformation. Separate sections containing equiaxed grains with a grain size of about 460 nm are also formed in the structure. It was presented that the aluminum matrix is crushed, and nanosized particles of the secondary strengthening phase Mg_2Si are formed.

1.3. Destruction of metal samples under static tension

Destruction is a rather complex, multi-stage process, which is influenced by a large number of factors. The destruction process begins with the formation of submicroscopic pores and ends with the division of the sample or the overall structure into separate parts. Very many mechanical properties of metals and their alloys determine their fracture resistance, as well as the amount (work) of deformation before fracture [16].

Professor Starkey proposed a classification system [50] for various types of destruction based on three determining factors: 1) the nature of the destruction; 2) places of destruction; 3) causes of destruction. The nature of deformation and destruction is divided into main groups: elastic deformation; plastic deformation; gap, i.e. division into parts; material change (metallurgical, chemical and nuclear). The causes of destruction are also divided into classes: process time; load type; temperature; environmental impact. Destruction can be volumetric and surface, and it determines the type of destruction site [51,52].

Viscous, i.e. plastic, destruction is the destruction that occurs as a result of the process of nucleation, merging and propagation of internal pores. Plastic flow is carried out at an angle of 45 ° towards the main normal stresses under the action of the main shear stresses. Therefore, a fracture position at 45° to the direction of force corresponds to static failure in ductile materials [51,52]. If the considered fracture is perpendicular to the action of the force, then the fracture is considered brittle. And it will occur under the action of normal stresses (Figure 1.3.1.b). Sometimes both components are present in a fracture.

Ductile fracture in metals is characterized by slow crack propagation, as well as high energy consumption, starting from the stage of crack initiation, because a significant work of plastic deformation is required. Ductile fracture corresponds to a fibrous structure and high roughness. There is no metallic sheen. The fracture is a relatively flat central part. Outside the central part, cut lips are formed. Near the fracture surface, a tightening is formed, which reflects the macroplastic deformation of the sample during ductile fracture. The occurrence of ductile fracture in industrial metallic materials is

explained by the porosity of the material in the region of localized plastic deformation, or shrinkage [5, 52].

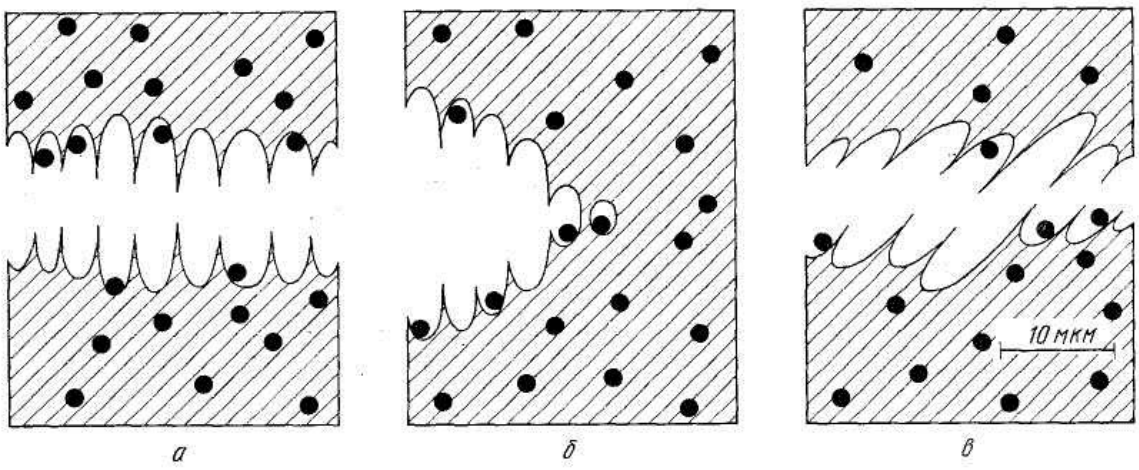

Figure 1.3.1.Scheme of ductile fracture with the formation of a pitted fracture surface at: a) uniaxial tension, b) eccentric tension, c) -pits[53].

During plastic flow, micropores most often begin to nucleate on inclusions, grain boundaries, undissolved particles of second phases, in deformation bands, or other places where there are defects leading to a concentration of plastic flow. Through a particle of the second phase or along the “particle-matrix” interface, detachment of the material can occur at the sites of micropore nucleation. With an increase in plastic deformation, micropores also grow, and new ones are formed, the distance between large micropores decreases and narrow ridges, which are the boundaries of micropores, break, and then destruction occurs (Figure 1.3.1).

a) 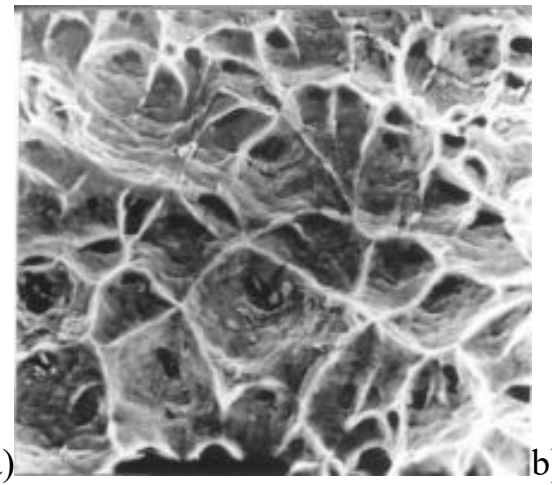 b) 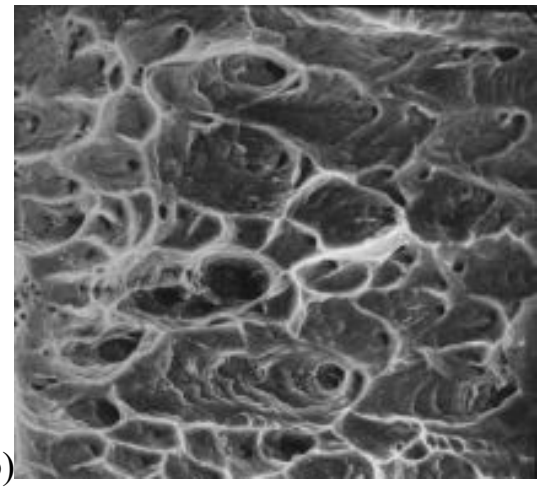

c) 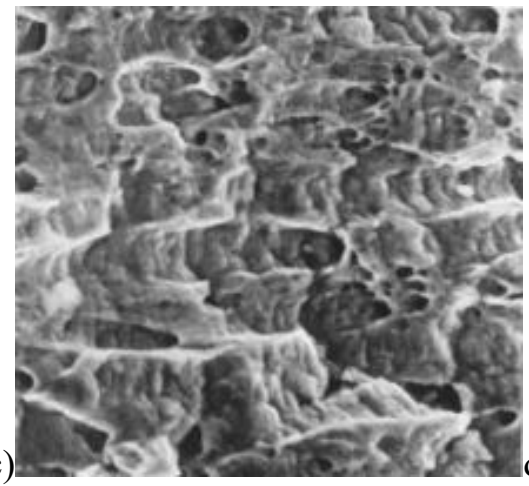 d) 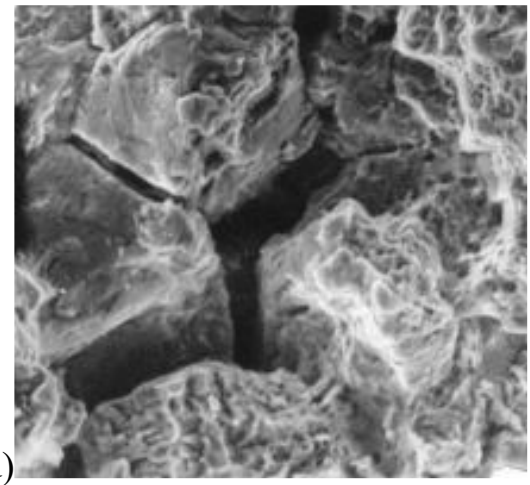

e) 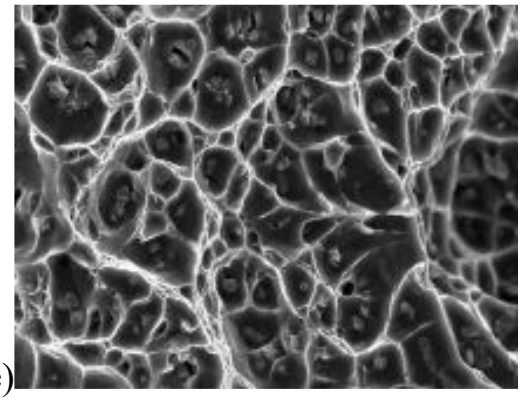

Figure 1.3.2.Microrelief of fracture pits for the surface of a material with UFG structure: a) equiaxed pits(under consideration steel H26T3), b)shear pits(For steel H32T3), c)separation pits(Forbecome40X4G18N8F), d)intergranular ductile fracture(Forbecome40G18F), e)holes with inclusions(at AK alloy4-1): ×1000 [54-56].

The fracture surface consists of a large number of cup-like depressions - these are pits. If the fracture is ductile, then the sizes and shapes of the pits are usually non-uniform. The shape of the pits is determined by the relative direction of the maximum stress, which causes destruction [1, 2]. Neither Figure 1.3.2 shows the types of fracture pits for UFG material [2]. For example, Figure 1.3.2.a shows equiaxed pits, which are formed, for example, in the center of a fracture during uniaxial tension. Figure 1.3.2.b match ishear marks - they are extended in one direction on the fracture surface (and in the opposite direction on the mating surface) and are located on the surface of the cut lips.

Figure 1.3.2.c shows the tear pits that form as a result of an eccentric stress state, which corresponds, for example, to notched specimens that are commonly tested for fracture toughness as well as toughness. Separation pits are formed from stretched

micropores, and then they form the initial region of crack growth in the fracture site. The number of micropore nucleation sites and the relative plasticity of the matrix determine the size of the pits. The surface of the pits indicates slip, waviness, or stretch zone, which indicate signs of deformation. Ductile fracture is mostly intragranular, but can also be intergranular (Figure 1.3.2,*d*). You can see the inclusions inside the pits themselves (Figure 1.3.2,*e*. A ductile fracture always indicates a high energy consumption of destruction and a high resistance to the development of a crack in the material.

It is possible to draw a conclusion about the mechanism of destruction due to fractographic analysis, which has been actively used in recent years. Figure 1.3.3 shows a typical structure of aluminum ductile fractures. It is characterized by a certain relief from a set of individual pits. Their diameter corresponds to the size of 0.5 - 20 microns. The size of the depth of the pits reaches several micrometers and characterizes the size of the region of severe plastic deformation. The result of the formation, growth and coalescence of a large number of micropores/pores are pits on the fracture surface. In the depths of the pits, there are particles of excess phases, which proves the appearance or nucleation of most micropores in these inclusions. Severely deformed pits and areas without characteristic structural features are located on the “walls” of the cup fracture (Figure 1.3.3).

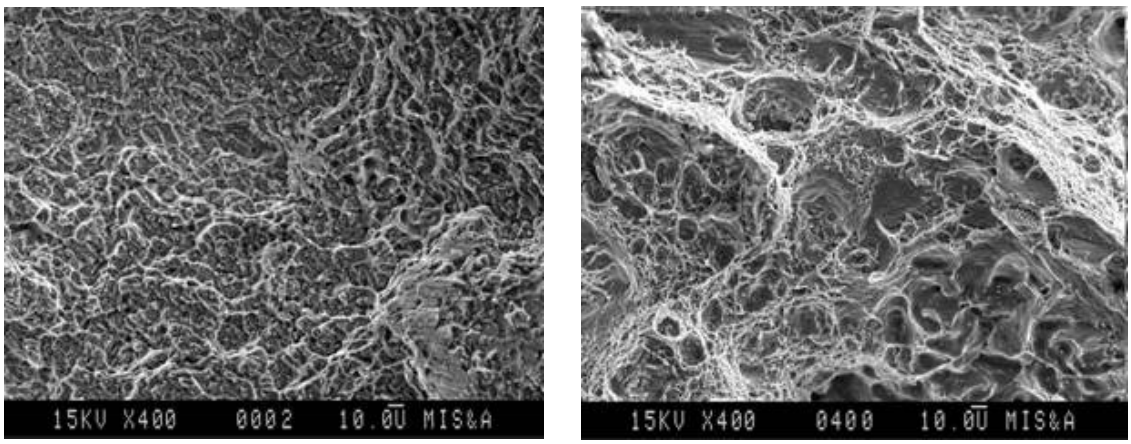

a) b)

Figure 1.3.3. Typical microstructure of ductile fractures of aluminum alloys [51].

In static tension, specimens are tested both with round and rectangular sections. There are certain requirements for creating samples: specific geometry and method of cutting the material. Good diameter uniformity, low roughness, absence of surface defects, as well as coaxiality along the length of the entire sample are needed. It is also impossible to overheat the material and change its microstructure.

With a round section of the sample, its working length is usually considered to be four or five diameters (short samples), or ten diameters (normal samples). Before stretching, the diameter of the sample is measured to calculate the stress σ and the relative residual contraction after failure. If an extensometer is used, then the length of the working part is measured, and such quantities as the deformation ε, as well as the elongation at failure will be automatically calculated using a computer or independently from the diagram σ - ε [51,52].

In the case of polycrystalline metals, the formation of a cellular structure is strongly influenced by the grain size. This is explained by the fact that at one degree of deformation, a decrease in the grain size leads to an increase in the dislocation density and a reduction in the dislocation path length. Both of these factors facilitate the formation of a cellular structure, however, in grains smaller than 10–3 mm, a cellular structure is not formed [60].

An analysis of the data obtained by various authors shows that the change in cell sizes for single- and polycrystalline iron, depending on temperature, strain rate, orientation, grain size, and type of loading, is within 0.6–3 μm. Upon deformation in the neck, according to [47, 60], for Armco iron, the cell size decreases from 1.5 at $\psi = 0{,}21$to 0.8–0.6 μm at $\Psi = 0{,}50$. Under conditions of limiting localization of plastic deformation and exhaustion of plasticity, crack initiation occurs when the limiting distortion of the crystal lattice is reached due to the formation of unfavorable, stressed bulk dislocation clusters.

Ductile fracture kinetics

All types of fracture controlled by plastic deformation are characterized by the presence of certain stages of damage and threshold stresses separating one stage of damage from another. These stages include [53]:

1) incubation period during which a cellular dislocation structure is formed;

2) the period of accumulation of reversible damage, during which discontinuities arise that can exist in the metal under load, do not disappear when the stress is removed and do not affect the specific energy of deformation () of the material (damages can be healed by heat treatment);A_p

3) the period of accumulation of irreversible damage, corresponding to the occurrence of defects affecting;A_p

4) macro-destruction that occurs when the viscosity of the material in the dangerous section is exhausted.

Each stage is characterized by a specific evolution of the dislocation structure and certain features of the change in structure-sensitive properties with increasing strain [62]. For a long time, the accumulation of damage under conditions of ductile fracture was associated with the formation of pores, while attaching importance to the damage mechanism. The data obtained using more accurate methods allow us to conclude that nucleation cracks appear already during the incubation period and become critical when their size reaches the cell size [5].

The first stage of damage is associated with the accumulation of crystallographic cracks mainly in the surface layer of the deformable material, i.e., damage is determined by the dislocation mechanism. This stage is limited by two threshold stresses $\sigma_к^c \ and \ \sigma_к^m$, which characterize the formation of crystallographic cracks of a critical size equal to the cell size of the dislocation structure at $\sigma_к = \sigma_к^c$. Then, a crack of a critical value forms in the damaged surface layer, which determines the transition from the dislocation damage mechanism (crystallographic dislocation cracks) to the vacancy damage mechanism (pore formation) at $\sigma = \sigma_к^m$.

In the second stage of damage, the formation of pores and the evolution of the dislocation structure are strongly influenced by inclusions and the presence of second phases. This stage actually refers to the period of neck formation; there is a deformation hardening of the material, which is not associated with a change in the stress state in the neck.

In [63], the features of fracture and the appearance of cracks in pure aluminum and aluminum alloys under tensile stresses on flat samples with a working part of 37x3x2 mm with a polished surface after some plastic deformations were studied: at the initial

stages of deformation, straight-line slip marks appear, oriented at 45^0 to stresses, and indicating shifts of individual parts of the crystal from each other; with further stretching, slip bands appear in crystallographic planes of a different orientation; with a further increase in deformation, a second system of slip bands arises, crossing the previously formed ones - the deformation proceeds sequentially or simultaneously in several directions of easy slip.

The destruction of most pure metals under the action of tensile stresses is preceded by plastic deformation with the formation of a neck. Pores appear in the neck, which merge, form cracks, leading to the destruction of the sample. In high-purity (impurities 0.01%) coarse-grained Al, the formation of a neck is not accompanied by the appearance of pores, and destruction occurs when pores appear, which originate in intense deformation bands [18]. At high degrees of deformation, a reorientation (rotation) of grains of an unfavorable orientation occurs. The number of slip bands at room temperature increases with the degree of deformation. At the grain boundary, the bands slow down or continue in the case of small angular misorientations. Fracture has a transcrystalline character [64]. Plastic deformation in polycrystalline Al proceeds extremely inhomogeneously. Localization of deformation in microblasts is observed. Deformation in pure polycrystalline Al is prone to localization. Fracture is associated with these areas of deformation localization, and future areas of destruction are predetermined already at the initial stages of deformation. The formation of optically visible cracks in Al was not observed until deformations close to sample failure. In the SEM at a deformation of 25%, microcracks are already observed inside the grains at the intersections of the slip bands. According to [63], microcracks are viscous retarded in undeformed regions in pure Al. The formation of optically visible cracks in Al was not observed until deformations close to sample failure. In the SEM at a deformation of 25%, microcracks are already observed inside the grains at the intersections of the slip bands. According to [63], microcracks are viscous retarded in undeformed regions in pure Al. The formation of optically visible cracks in Al was not observed until deformations close to sample failure. In the SEM at a deformation of 25%, microcracks are already observed inside the grains at the intersections of the slip bands. According to [63], microcracks are viscous retarded in undeformed regions in pure Al.

In low-alloyed solid solutions of Al, the deformation stages are similar to pure Al: rectilinear slip marks appear [63]. With further stretching, slip bands appear in crystallographic planes of a different orientation, then a second system of slip bands arises, crossing the previously formed ones. At high degrees of deformation, grains of an unfavorable orientation are reoriented.

In low-alloyed solid solutions up to 3% Mg, there is no clear dependence of the strain distribution over the grain volume and over the boundary regions. In supersaturated solid solutions (9.5% Mg), the strain distribution over the grain volume is characterized by a smaller spread than along the grain boundary (at the grain boundary, the strain distribution is more inhomogeneous). This applies to coarse-grained Al-alloys based on high-purity Al. In deformed alloys, the strain distribution is more uniform than in cast alloys. In deformed Al-Mg alloys, in contrast to cast alloys, crack initiation is more likely in terms of grain volume, and in Al-Cu-Mg alloys after heat treatment, crack initiation is equally probable in terms of volume and grain boundaries. In high-alloy cast alloys, the grain boundaries are embrittled due to the decomposition of the solid solution, and brittle cracks appear in the boundaries before destruction.

In homogeneous solid solutions, there are no structural components on which cracks can nucleate in the early stages of deformation. And cracks do not appear until deformations close to destruction. In homogeneous solid solutions, as in pure Al, areas of increased deformation appear already at the early stages of deformation and are not further redistributed, and in the course of further deformation, nucleation cracks appear in these areas [90]. In saturated solid solutions, areas of increased deformation are redistributed at different stages of deformation (deformation is more uniform). However, from the moment cracks appear, elongation occurs due to crack opening.

With an increase in alloying, the inhomogeneity of the course of deformation along the boundaries increases in comparison with the grain volume for cast alloys. For deformed alloys, the picture is reversed: slip bands are more evenly distributed over the volume of grains than in cast alloys. Deformation proceeds predominantly over the volume of grains. This increases the probability of intercrystalline fracture for cast alloys (alloyed with >1.5% Mg) and transcrystalline fracture for deformed ones.

In binary cast alloys Al-Fe (0.5-1.8% Fe), crystals of intermetallic compounds (Al3Fe) are located in the form of eutectic along the grain boundaries. Plates of eutectic particles have a thickness of up to 30 microns. In Al-Fe alloys with a composition close to eutectic (1.8% Fe), individual rhomboid particles up to 100 μm in size can be observed. The structure of Al-0.3 and 0.5% Fe alloys is Al with separate precipitates. The deformation is localized in coarse slip bands in Al grains [95]. With an increase in the Fe content, the strength increases, and the ductility decreases. Local deformation in microvolumes in Al-0.3 and 0.5% Fe alloys proceeds very unevenly (as in pure Al and in low-alloy alloys). The destruction is preceded by the formation of several foci of increased local deformation (29-30%). One of these centers, developing, leads to the destruction of the sample at a local deformation of 60% and at an average deformation of 20%. Fracture is intercrystalline. Particles of precipitates slow down the course of deformation, increasing strength, but cannot prevent the localization of deformation in microregions. In Al-0.3 and 0.5% Fe alloys, the deformation microrelief is characterized by the presence of deep folds along the load direction [63]. With an increase in the amount of Fe, the number of folds decreases.

Chapter 2. Material and research methods

Pure aluminum has a rather low strength and is not applicable as a structural material. If it is alloyed with other elements, thermal and mechanical treatments are applied, then its strength will increase. Various aluminum alloys have high mechanical strength under the condition of low density, therefore they are considered as structural materials.

2.1. Formulation of the problem

A review of the literature has shown that Al alloys 6101 in the obtained UFG state are of great interest. The process of fracture of UFG 6101 alloys, including the process of formation of pores in the material under critical deformations before fracture, remains little studied. The study of the features of destruction and the structure of the material at the stages of destruction is important for a more complete description of the properties of UFG materials. In this regard, the **purpose of the work** was to study the features of the mechanical behavior and fracture of Al-6101 alloy samples., relating to the lines of alloys of the Al-Mg-Si series depending on its structural state: in UFG state and after standard heat treatment.

To achieve the goal of the study, the following **tasks** were set:

1. Study of the mechanical behavior of alloy samplesAl6101 with different structure: after artificial aging and in UMP condition.
2. Numerical simulation of the stress-strain state in static tension of Al 6101 samples.
3. Investigation of the features of destruction of samples in CG and UFG statesalloy Al-6101.
4. The study of the structure along the length of the samples after stretching to various degrees of deformation to identify the moment of nucleation of pores / cracks in the material, as the first stage of the destruction process.

2.2. Research material

Technical heat-strengthened aluminum alloy 6101, which belongs to the systemAl-Mg-Si, its chemical composition is given in Table 2.1.1.

Table 2.1.1. The chemical composition of Al 6101 (wt.%)

Brand	Limit	Si	Fe	Cu	Mg	Zn	B	Al	Ti+V+Cr+Mn
6101	Max	0.60	0.30	0.01	0.60	0.02	0.01	the basis	0.015

The state diagram of the Al-Si-Mg system was developed by Hansen and Heiler [65]. The quasi-binary section Al - Mg_2Si divides the aluminum angle of this diagram into two secondary systems (Al-Si-Mg_2Si and Al - Mg_2Si - Al_3Mg_2) of the eutectic type with limited and varying solubility of the components in the solid solution.

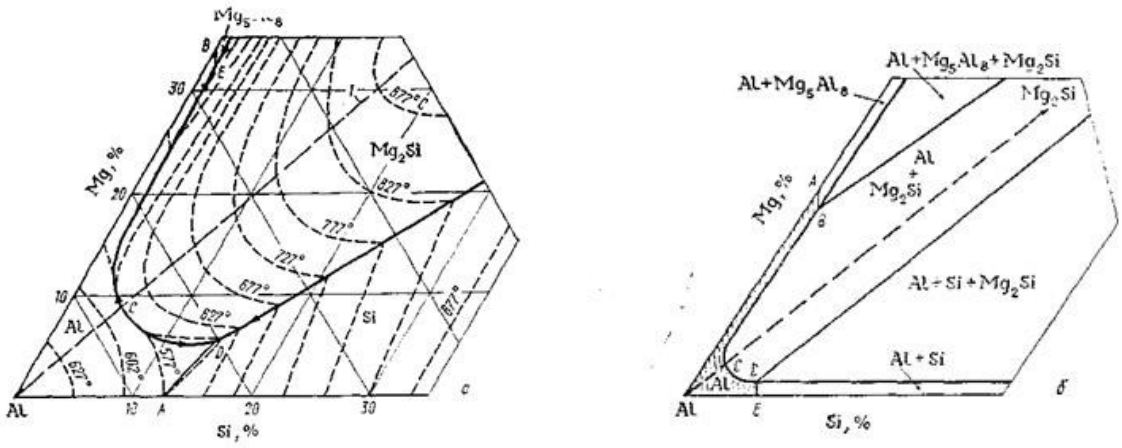

a b

Figure 2.1.1.Aluminum angle of the Al-Mg-Si diagram: a - projection of the liquid us surface; b - distribution of phase regions in the solid state.

In the Al-Si-Mg_2Si system [21], in which the AL9, AL34 (VAL5), AL4 alloys [1] are located, a ternary eutectic α+Mg_2Si+Si with a melting point of 550°C is formed, which limits the heating temperature for quenching [19] . These alloys are significantly strengthened during heat treatment due to the formation of supersaturated solid solutions of magnesium and silicon in aluminum during heating for quenching and

subsequent decomposition during cooling and aging with the release of fine particles of the Mg_2Si phase.

The solubility of Mg2Si and Si in a solid solution of aluminum is practically the same, but the formation and isolation of ultradispersed particles of the Mg2Si phase occurs quite slowly, in several stages.As the temperature decreases, the solubility of magnesium and silicon decreases, this is the basis of thermal hardening.The content of Mg2Si largely determines the value of mechanical properties, but the presence of magnesium and iron provides additional strengthening [24, 30].

Due to the low solubility of Si in Al at low temperatures (200 °C), the alloy has a heterogeneous structure under equilibrium conditions. Thus, the phase composition consists of two phases (a + Mg2Si). At a temperature of 550°C, the alloy is homogeneous, which makes it possible to harden it by aging [64].

Heat treatment

The alloys of the system under study are thermally hardened using the following modes:

- hardening (heating up to 510–550°C with subsequent cooling in water) + natural aging (NA) (time 10–15 days);
- quenching (heating to 510–550°C followed by cooling in water) + artificial aging (AA) (heating to 160–170°C for 10–12 hours).

2.3. Material processing techniques

The studied material belongs to heat-strengthened, and in the initial modification (without heat treatment) is not used in production, therefore, two methods of its processing were considered, which increase the strength properties of this alloy: in water at room temperature, then for 12 hours the material was aged by annealing at a temperature of 170ºC [35,37]; 2) processing by the ECAP method of conformals to obtain the UFG state [10, 46].

Experimental samples were made from wire rod obtained by hot rolling, manufactured by RUSAL, in the form of rods with a diameter of 10 mm. The initial rods were subjected to conformal ECAP processing according to the following modes -

annealing at 550º C for 2 hours, quenching in water at room temperature, and 4 cycles of conformal ECAP were immediately carried out at room temperature along the route Bc (turning the workpiece only in one direction each time), channel conjugation angle 130º[18.43]. The alloy was subjected to ECAP-C in the freshly quenched state of the solid solution and then underwent natural aging.

Figure 2.2.1. General view of blanks after processing of the 4th cycle by the ECAP-C method at 130°C along the route Bc.

Thus, part of the original wire rods was subjected to processing to obtain experimental samples in the coarse-grained state, the second part was subjected to processing to obtain an UFG structure. The obtained samples were used to study the influence of the type of structure on the mechanical properties, as well as to study the influence of the structure on the characteristics of the destruction of the material.

Structure research technique

In this paper, the study is devoted to the influence of the microstructure on the properties of the material; therefore, scanning electron microscopy (SEM) was used to study it, and a Zeiss Supra 40VP electron microscope was used.

The study of the surface of the cylindrical samples destroyed by mechanical static tension was carried out in order to obtain images of the surface with high spatial resolution and identification of the chemical composition of particles. Used: secondary electrons (SEI) and backscattered electrons (BSE) mode. secondary electrons (SEI)

mode sensitive to the relief of the sample surface; therefore, it was used to study the surface morphology of the samples. Back Scattered Electron (BSE) mode sensitive to compositional contrast, i.e. sample components having different compositions will have different grayscale tints in BSE images. This allows you to visualize the difference in composition between the constituents of the sample.

The surfaces of the axial cuts were preliminarily ground and polished, because after the cuts were made on an electro-erosion machine, their surface was unsuitable for SEM studies, due to the high surface roughness, which would not allow us to see the very structure of the material. Using SEM methods, we studied the surface of fractures and the content of numerous cup-like depressions (pits), which made it possible not only to observe the inclusions, but also to identify their composition.

The TEM method makes it possible to characterize the structure of the sample in the volume and on the surface, it also makes it possible to determine the qualitative phase composition of the sample and to determine the orientation relationships between the elements of the sample structure. A JEOL JEM2100 TEM (Transmission Electron Microscope) was used to study the fine microstructure at high magnification. Foils transparent to the electron beam were prepared for TEM. For this, plates were cut with a size of 5 by 3 by 0.6 mm. Next, the plates were mechanically thinned with abrasive paper to reach a thickness of 0.10-0.15 mm. To study the fine structure, the resulting plates were subjected to the jet polishing technique on a special Tenupol-5 installation, placed in a solution of 20% HNO3 and 80% methanol, the temperature was -25°C and the voltage corresponded to 15-20 V.

Mechanical test method

Mechanical tensile tests were carried out for determination of the qualitative and operational characteristics of the material, including strength and ductility. The properties determined by these tests are given in numerous material specification standards [51,52].

Samples were taken for the study, the general view of which is shown in Figure 2.2.2. with a circular section with a working base L 5 mm D mm. This base differs significantly from the base of samples according to GOST (GOST 1497-84, ISO 6892-84, ST SEV 471-88). This geometry of the samples was chosen because its use made it

easier to fix the stage of pore formation during tension by the SEM method (after slitting the sample after stretching to a certainε*). The samples were mounted in a Shimadzu AG-50kNX laboratory machine and stretched at a constant rate of 1.4 x 10-4 s-1 at room temperature. In the process of testing the material, the change in deformation was recorded using a video extensometer, which is equipped with a testing machine.

Cylindrical samples were made on CNC machines from the obtained rolled wires (bars with a cross-sectional diameter of 10 mm), a general view of which is shown in the Figure below:

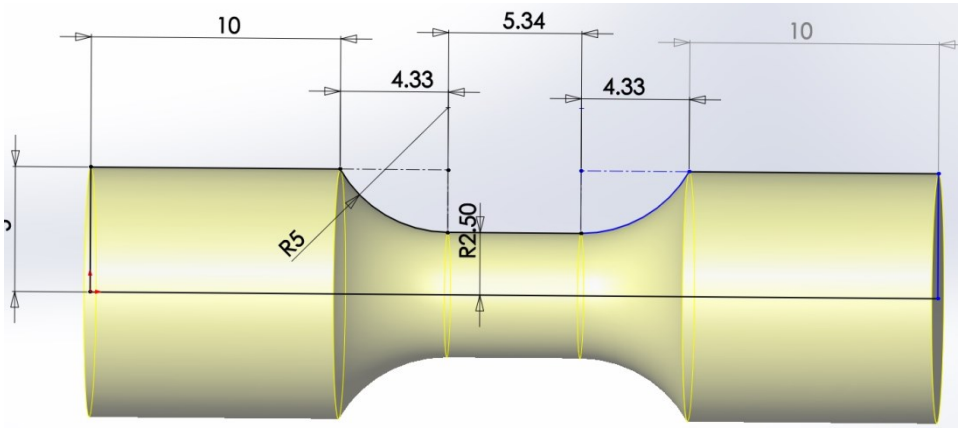

Figure 2.2.2. Engineering image of the type of samples under study.

After fabrication, the samples were subjected to heat treatment and then static mechanical tensile tests were carried out. A homogeneous stress state is created over the sample cross section, the material is under the action of normal and shear stresses. The tensile force creates stress in the test specimen and causes it to elongate. After mechanical testing, the samples were examined by SEM methods.

Publications on the research topic:

[66] Magomedova, DK Influence of grain size and second phase particles on the process of void initiation / Magomedova DK, Murashkin, MY// Journal of Physics: Conference Series. 2018. 991. 1. 012055.

[67] Magomedova, DK Technique development for conducting mechanical tests to study the pore formation process in case of material fracture / Magomedova DK, Efimov MA, Murashkin, MY //AIP Conference Proceedings. 2018. 1959. 070021.

Chapter 3. The structure and mechanical properties of the alloy in various states

The mechanical properties and behavior of the material under load are determined by the structure of the material under study. That is why, before mechanical testing, the structure of the studied aluminum alloy was studied.

3.1. Structure of Al-6101 alloy in coarse and ultrafine grains

The microstructure of the alloy in the initial CG state was studied using SEM and TEM. The original alloy processed by the traditional technology of hardening and aging, according to SEM, had a microstructure with an average grain size of 100 μm, light dots are intermetallic particles of the primary Al-Fe phase based on impurity Fe of crystallization origin, size≈5 μm.(Figure 3.1.1.a).

Also, in the structure of the investigated alloy, intermetallic crystalline inclusions (light particles) with a size of 0.5 to 7 μm were found (Figure 3.1.1.b) - these are distributed intermetallic particles based on Al-Fe, characteristic of these aluminum alloys [64]. These particles are just intermetallic particles of crystallization origin based on Al-Fe, on which, as will be shown below, pore formation and destruction occur under loading. These particles do not dissolve and do not transform when heated for quenching, i.e. the heat treatment performed in the used temperature range has practically no effect on them (particles will be discussed in more detail below).

a)

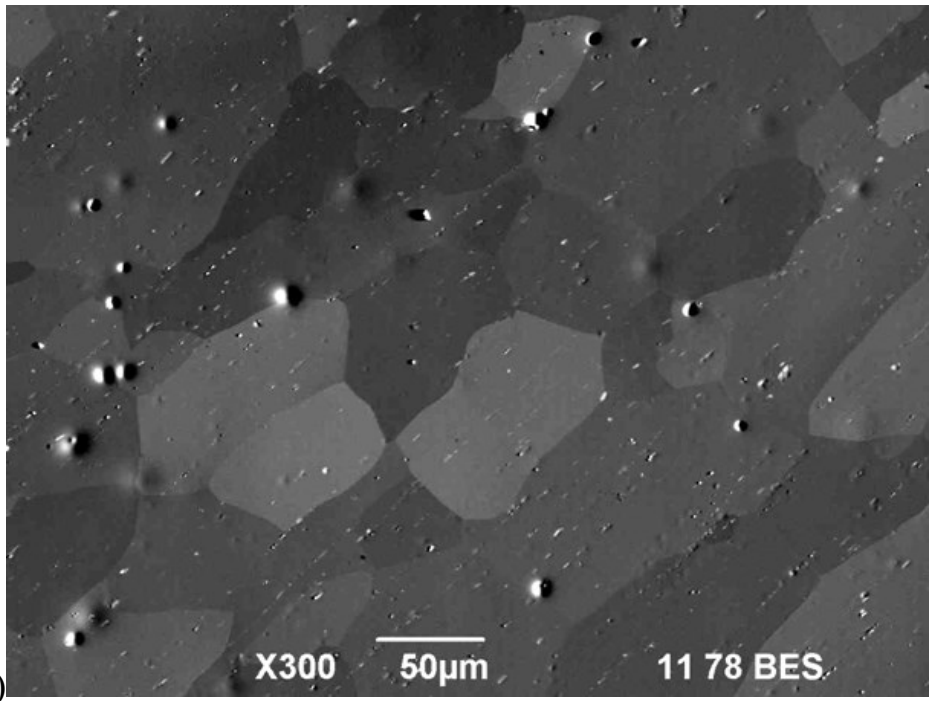

b)

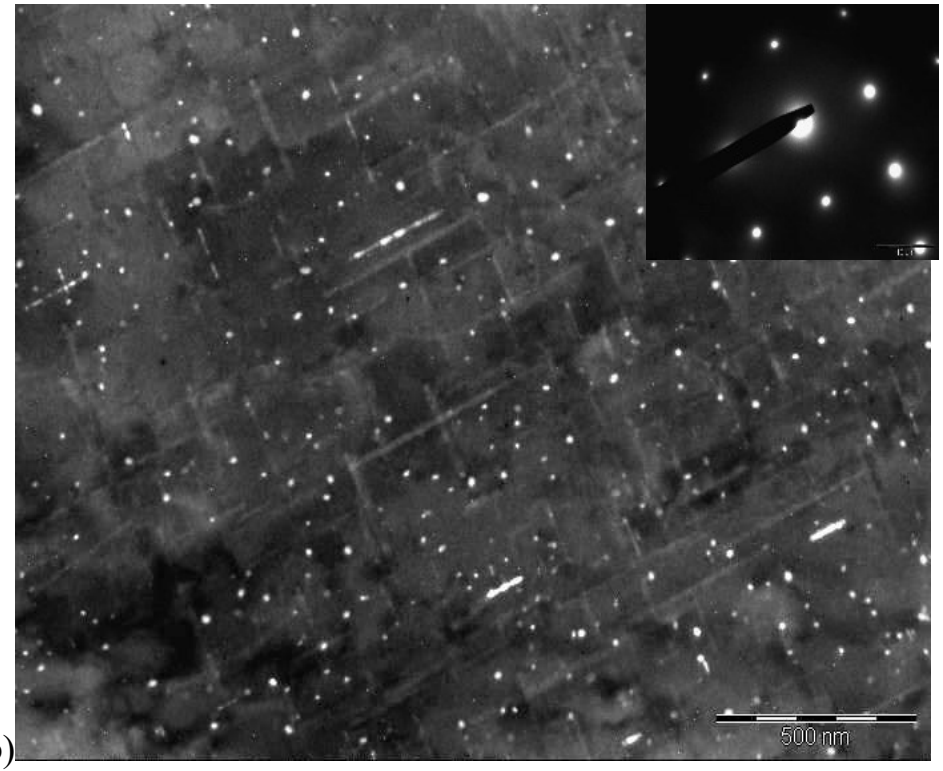

Figure 3.1.1. a) SEM and b) TEM images of the microstructure of the alloy after quenching and subsequent artificial aging at 170°C.

TEM studies of the alloy in the CG state also revealed very fine dispersed particles ranging in size from 3 to20 nm (Figure 3.1.2). These particles are dispersed particles of the secondary hardening β'-phase Mg_2Si formed as a result of quenching with aging. Analysis electron diffraction pattern confirms that the observed particles are particles of

the secondary phase of the Mg_2Si β'-phase (Figure 3.1.2.), known for the alloys of this system [68].

Precipitation of the strengthening Mg2Si phase in the (001) direction in the coarse-grained 6101 alloy after standard T6 treatment (TEM) is marked by the precipitation of an acicular metastable β"-phase.

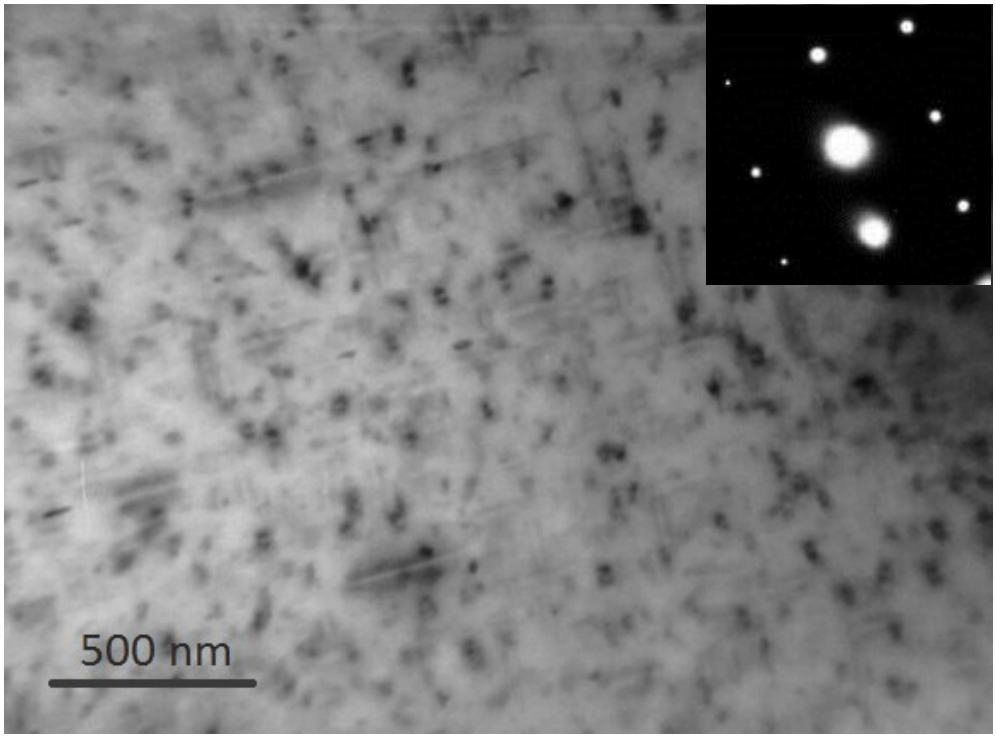

Figure 3.1.2. Alloy microstructure (TEM) after hardening and subsequent artificial aging at 170°C (SST+170°C) with particles of acicular metastable hardening phase β"Mg_2Si.

According to TEM data (Figure 3.1.3) as a result of ECAP-C, an UFG structure with Al-matrix grain size from 400 to 600 nm was formed in the alloy. The formation of the UFG structure during ECAP-C was accompanied by the decomposition of the solid solution and the formation of dispersed particles of the second phase, also 3 to 20 nm in size, due to dynamic aging (DA). Dynamic aging was observed earlier in various Al-Mg-Si alloys during SPD as at increased [10, 12, 15, 41,69-74], and at room temperature [62, 68, 71].According to research[10,12,15,41,69-74]in the process of ECAP-C, the formation of an ultrafine-grained structure in the alloy was accompanied by the process of decomposition of the solid solution - dynamic strain aging (DSA). The

manifestation of this process is typical for hardened aluminum alloys subjected to deformation processing and SPD [68–70].

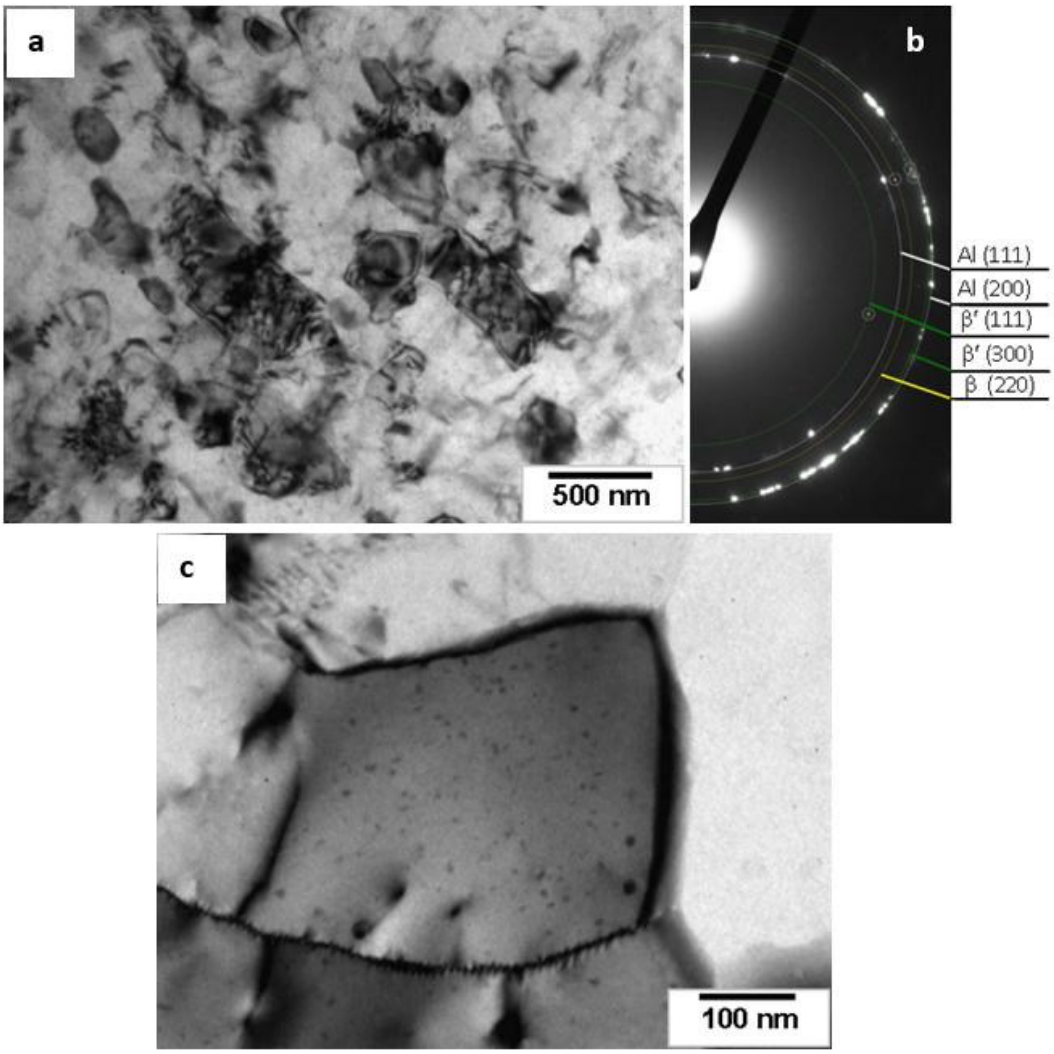

Figure 3.1.3. (a) Microstructure (TEM) and (b) patterns of the Al 6101 alloy after ECAP-C; and (c) view of the hardening precipitates of the second phase formed in the aluminum alloy matrix after treatment with ECAP-C [10].

SEM studies of Al-Fe particles

The structure of the surface of the axial section of the samples was studied using electron microscopy by SEM methods. Samples cut along the axis on an electro-erosion machine ARTA 123-PRO with precision 1-2 μm. Next, the cut surface was ground and polished to a surface roughness of 50 nm.

SEM study of particles of Al-Fe samples with a CG structure

In Figure 3.1.4. shows the area of the sample with white particles, which are particles based on iron. This statement is made on the basis of X-ray energy dispersive spectroscopy, the results of which are presented in Table 3.1.1, which indicate an increased content of iron particles in the bright areas indicated in Figure 3.1.4.

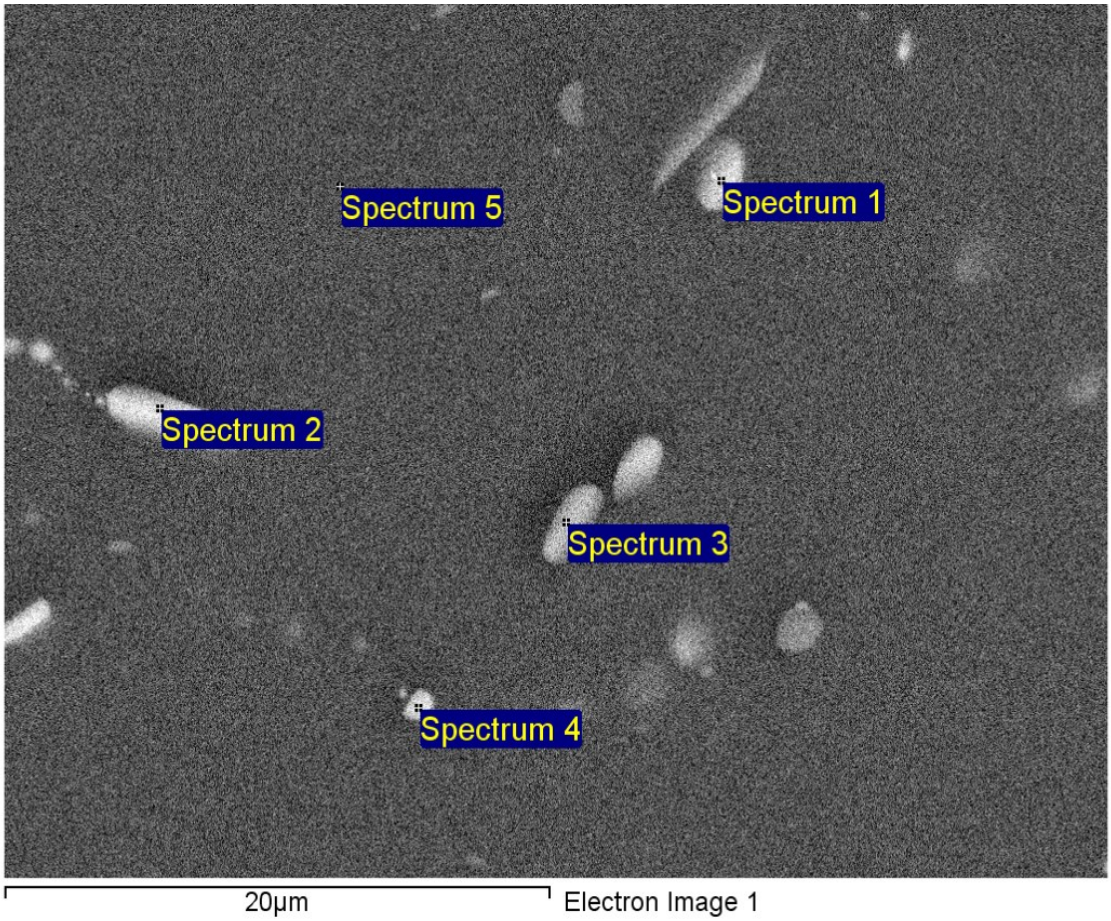

Figure 3.1.4.The surface of the axial cut of the sample with a short-circuit structure.

EDX-analysis (analytical method for elemental analysis of solids) of particles showed the presence in the particles of an increased content of Fe, Si relative to the matrix (Table 3.4.1). This composition is typical for intermetallic particles based on Al-Fein aluminum alloys of the Al-Mg-Si system, not containing Mn and/or Cr [75]

Table 3.1.1.The content of elements by sample areas presented in Figure 3.1.4.

Spectrum	Mg (wt.%)	Al (wt.%)	Si(wt.%)	Fe (wt.%)
Spectrum 1	0.57	85.92	7.67	5.83
Spectrum 2	0.75	86.57	7.62	5.07
Spectrum 3	0.68	88.54	6.93	3.85
Spectrum 4	0.69	91.92	3.20	4.19
Spectrum 5	0.81	98.51	0.69	0.00
mean	0.70	90.29	5.22	3.79

Most likely, the intermetallic compound is formed as a ternary AlFeSi compound, taking into account that the silicon content in the particles (in the scanned areas) is also noticeably increased relative to the average for the alloy (0.60%). These particles do not dissolve and do not change during quenching annealing and do not change during subsequent heat treatments (aging annealing) [29]. Further, for short, we will call these particles intermetallic compounds based on iron or Al-Fe. This confirms that the observed particles are particles of intermetallic compounds based on Al-Fe. Spectrum No. 5 does not correspond to the region with white particles, and, as analysis shows, this spectrum also does not contain Fe. The sizes of Al-Fe particles in CG are up to 7 μm.

SEM study of particles of Al-Fe samples with UFG structure

An analysis of the axial cut surface similar to that described above was prepared for UFG samples obtained by the ECAP-K method. Al-Fe particles stand out on the surface and their location and size can also be estimated. The previous analysis showed that the light particles on the axial sections are iron intermetallics, therefore, for UFG samples, it is sufficient to estimate the size of these particles (Figure 3.1.6).

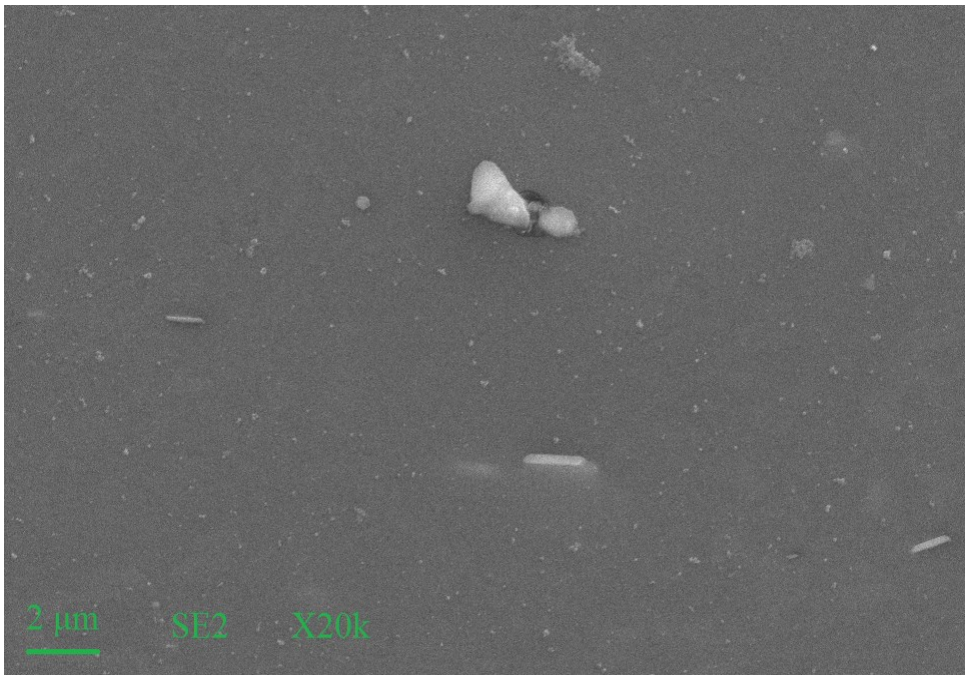

Figure 3.1.5.The surface of the axial cut of the sample with UFG structure and geometric marks for Al-Fe particles.

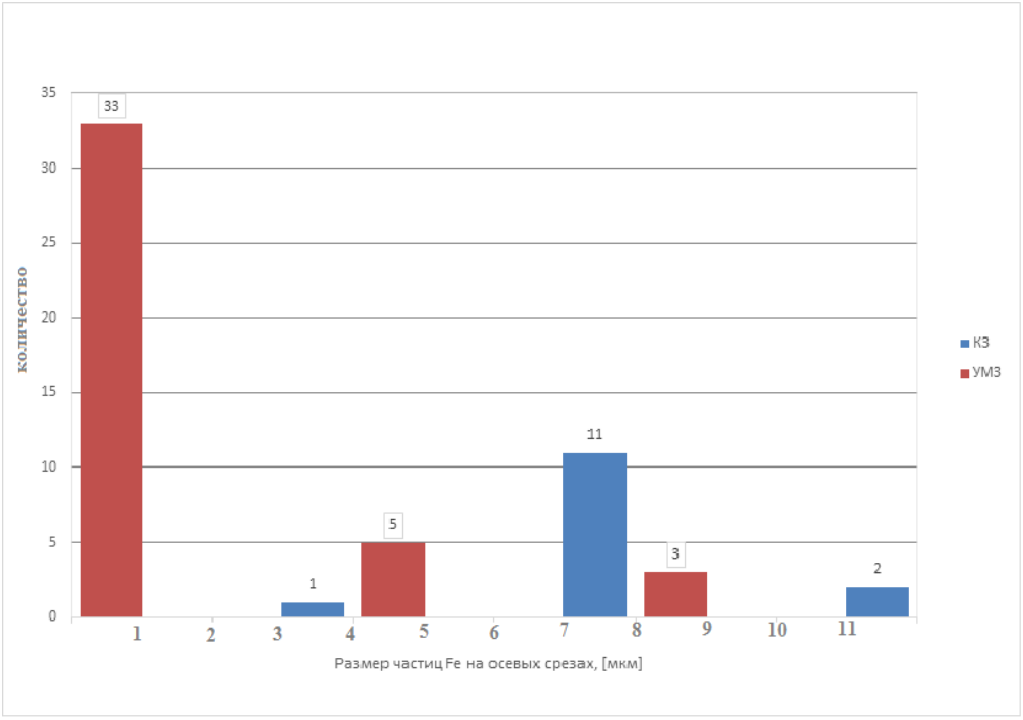

Figure 3.1.6. Al-Fe particle size distribution histogram in CG and UFG samples.

Based on the data obtained for the UFG structure, it can be concluded that the sizes of Al-Fe particles in the UFG material are up to 2 µm. Combining with the data for the CG material, it can be argued that the ECAP-C treatment results in fineness of the Al-Fe particles from 7 to 2 µm in the 6101 alloy.

3.2. Mechanical behavior of Al-6101 alloy in coarse and ultrafine grain conditions

Figure 3.2.1.a-c shows σ (ε) diagrams for samples of different structural states. According to the fracture diagrams, the main strength characteristics of the material are calculated, which are presented in Table 3.2.1

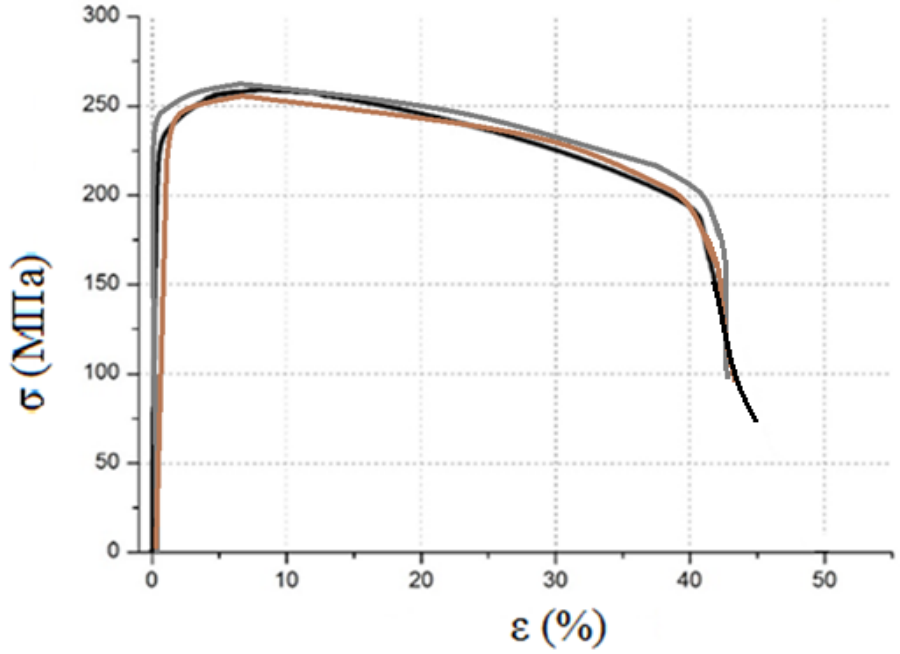

a)

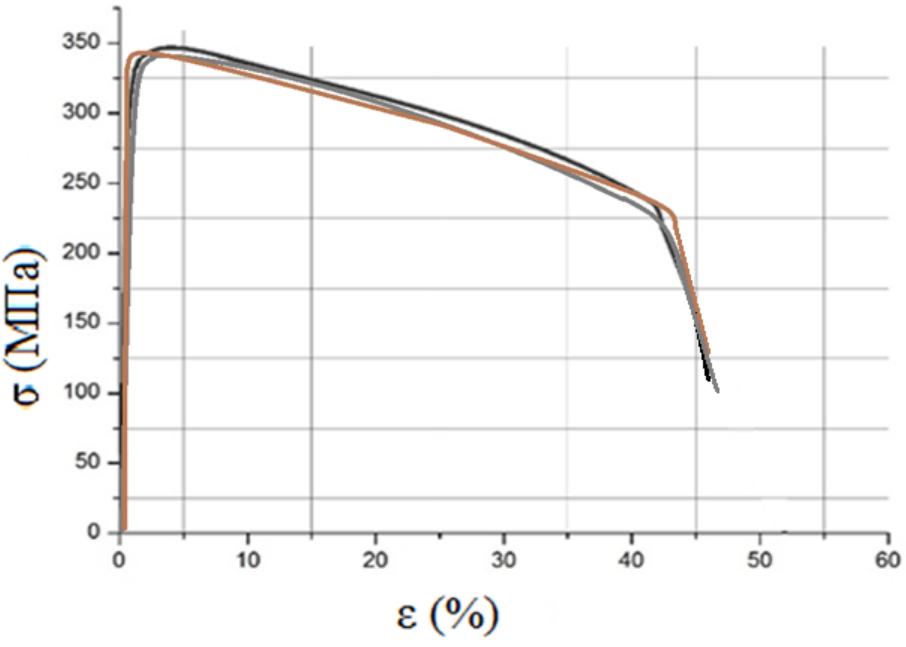

b)

Figure 3.2.1.Diagrams of deformation obtained during tension of specimens with a) CG, b) UFG structure.

Table 3.2.1. Average values of yield strength and strength for: a) CG and b) UFG samples.

Structure type	Yield strength, MPa		Tensile strength, MPa		Relative deformation, %	
		av. value		av. value		av. value
CG	220	230±10	255	265±10	46	45±5
	230		266		43	
	240		274		44	
UMP	315	304±10	341	351±10	46	44±5
	303		150		47	
	294		362		48	

It can be concluded that the CG and UFG specimens of the 6101 alloy structure have approximately the same relative elongation strain to failure of ~50%.

For comparison, the international standard [23] describes the mechanical properties of the 6101 alloy in the following terms:

- 6101-O (annealed, heated at 415°C for 2-3 hours): maximum tensile strength not more than 150 MPa and maximum yield strength not more than 83 MPa, elongation (stretch to failure) 10-18%;
- 6101-T4 (dissolved and artificially aged): tensile strength not less than 180 MPa and yield strength not less than 110 MPa, elongation 10-16%;
- 6101-T6 (dissolved, stress-free stretched and artificially aged): tensile strength of at least 290 MPa and yield strength of at least 240 MPa, elongation of 8% or more.

It can be noted that the obtained plasticity values (about 50%) are noticeably higher than the GOST data for the short-circuit state and data [55.68] for UMP state. This is due to the fact that in our experiment, For the study, samples with a “short” working base L 5 mm D 10 mm were selected in comparison with the GOST samples.

Samples with UFG structure showed strength 25% higher than samples in the CG state. Previously in [29.30.68] approximately the same strength values were indicated

for the 6101 alloy processed by the ECAP-Comform method for tests carried out on cylindrical specimens according to GOST. The increase in strength and yield strength as a result of ECAP-C is explained by a decrease in the grain size of the alloy. Grain boundary strengthening - the result of grain refinement during ECAP-conforms is added to dispersion strengthening (which is the result of natural aging after ECAP-conforms).

Construction of diagrams true strain - true stress [106]

During tensile tests of specimens on a universal testing facility, the so-called machine (or conditional) deformation diagram “force P - movement of the gripper” is recorded«Δl_{Σ}» (Figure 3.2.2). As a result, the following characteristics were determined:

- σ_V– ultimate strength, N/mm2;
- $\sigma_{0.2}$– conditional yield strength, N/mm2;
- δ_5– relative elongation after rupture, %.

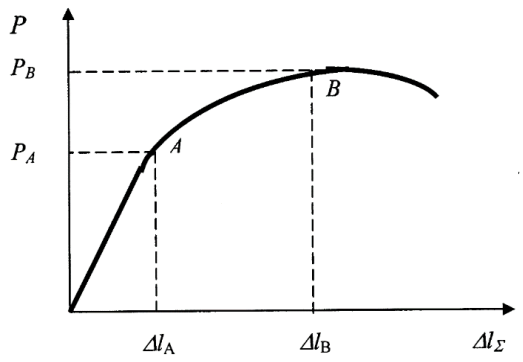

Figure 3.2.2. Scheme of the machine deformation diagram.

Conditional diagrams of deformation of materials in the coordinates "stressσ-deformationε» was obtained by recalculating the machine diagrams of deformation «force P - displacement of the gripperΔl_{Σ}". However, the conditional tension diagrams, as well as the parameters determined from them, do not quite correctly show the behavior of the material, since in the conditional diagram: 1) there is also a contribution made by the deformation of the testing machine; 2) in conditional diagrams during tension, stresses are calculated from the ratio:

$$\sigma = P/S_0, \qquad (3.2.1)$$

where S_0 is the initial cross-sectional area of the sample; however, when stretched, the cross-sectional area of the sample changes. To correctly record the description of the mechanical behavior of the material, the true strain - true stress diagram is considered, and the method for constructing them is described below.

The deformation of the machine consists of two parts: elastic $\Delta l_{\text{м}}^{\text{у}}$and plastic $\Delta l_{\text{м}}^{\text{п}}$, while the elastic deformation depends linearly on the applied load, and the plastic deformation is due only to the plastic deformation of the sample.

The first step to recalculate the curve is to determineΔl_{gaps}. After defining Δl_{gaps} from valueΔl_{Σ}(moving grip) of each point of the curve is subtracted Δl_{gaps}

$$\Delta l_{\Sigma} - \Delta lgaps = \Delta l'_{\Sigma} \qquad (3.2.2)$$

Relative deformation:

$$\varepsilon = \Delta l / l, \qquad (3.2.3)$$

True deformations:

$$e = \ln(S_0/S_t) = \ln(l+\Delta l)/l0\ , \qquad (3.2.4)$$

where S_t is the current section of the sample.

To construct true material deformation diagrams, the coordinates “true stresses σi – true strains e” were used. The values of σi and e were calculated using formulas 3.2.5 and 3.2.6:

Until the moment of strain localization (because the volume is constant), the stress was calculated by the formula:

$$\sigma_i = \sigma\ S/S_0 = \sigma\ d^2/d^2_0 = \sigma\ l_0/l \text{ or },\sigma_i = \sigma(1 - \varepsilon_1) \qquad (3.2.5)$$

where σ is the conditional stress,

$$e_i = e_1 = ln(1 + \varepsilon_1) \qquad (3.2.6)$$

Formulas (3.2.5) and (3.2.6) are applicable only up to the moment of strain localization. After the formation of the neck, the deformation is determined taking into account the change in the cross-sectional area:

$$e = \ln(S_0/S_t) \qquad (3.2.7)$$

where S_0 is the initial area of the sample, S_t is the current area of the sample in the neck.

The true fracture stress is found by the formula:

$$\sigma_{idestr} = \sigma_{destr.}\ S_0/S_p \qquad (3.2.8)$$

To solve the problem of the dissertation, in the first approximation, we consider that the section from $\sigma_{iв}$, i.e. from the beginning of strain localization to failure, there corresponds a linear increase in true stress with an increase in true strain.

On the curve, true deformation - true stress, indicate the point σ_{idestr}. Let's connect the points $\sigma_{iв}$ and σ_{idestr}. and obtain a curve in the region of strain localization for the first approximation.

As a result, we obtain the desired diagram: true strain - true stress. At that moment, when the stress exceeds the strength of the sample, it will break.

To study the patterns of destruction of Al 6101 alloys, it is important to construct true strain-stress curves under static tension, as well as their analysis to identify the causes of increased true fracture stress.

After destruction, 2 symmetrical parts of the original samples were obtained, which were further used for microstructural analysis of the destruction surface of our material in all structural states.

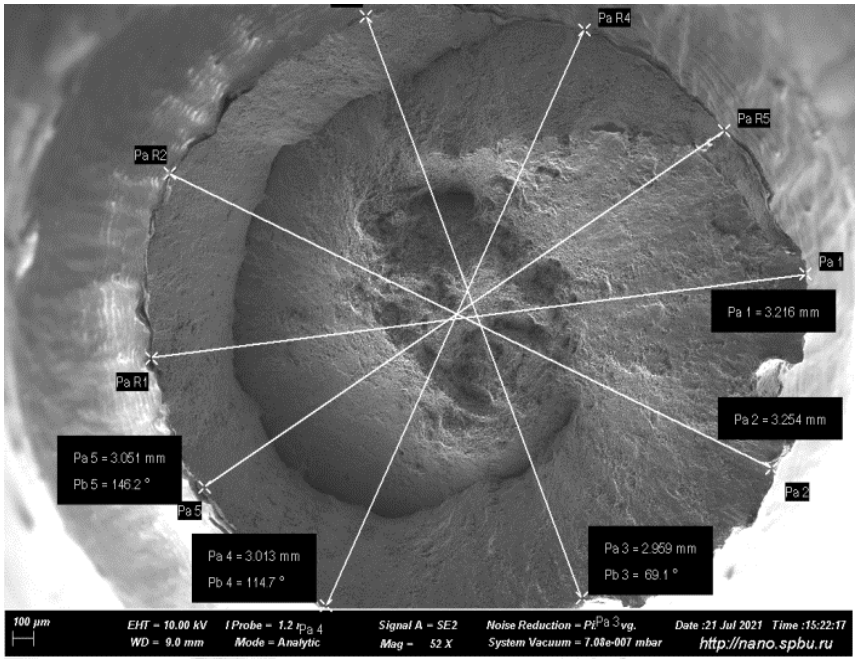

Figure 3.2.3. General view of the detachment surface of a specimen with a UFG structure to determine the cross-sectional area of the specimen during fracture.

To calculate the true deformations before failure of samples in various states, the diameter in the neck section was measured (Figure 3.2.3, 3.2.4) on the SEM in secondary electrons (SEI) mode.

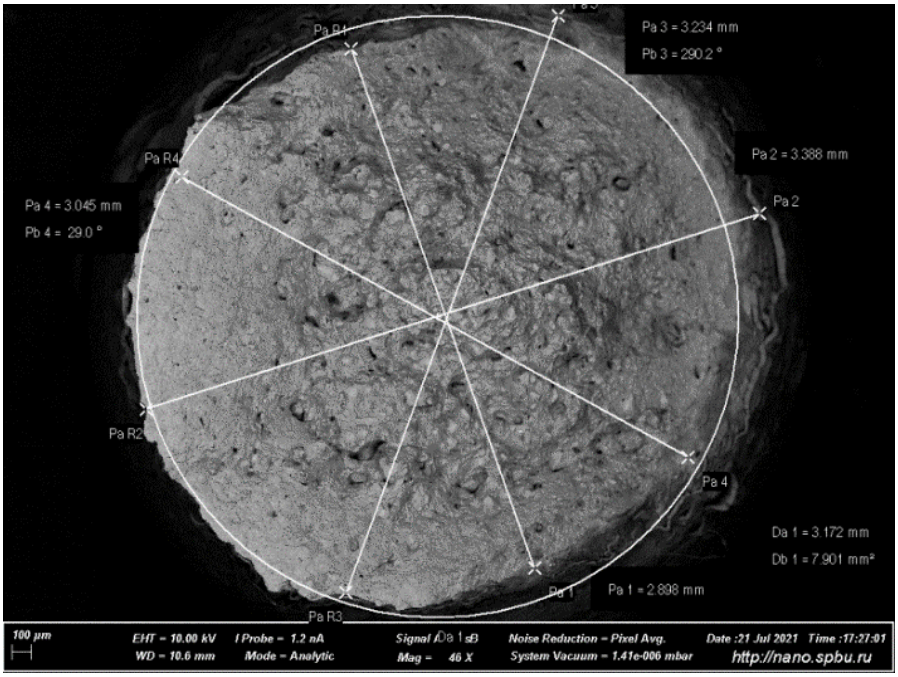

Figure 3.2.4. General view of the detachment surface of a sample with a CG structure to determine the cross-sectional area of the sample during destruction.

Based on the conditional tension diagrams presented above (one typical test curve for each state was selected) and taking into account the destruction area determined from the images above, diagrams of true stress from true strains for each state were constructed, which are shown in Figure 3.2.5.

Conditional tension diagrams for UFG and CG states are shown in Figure 3.2.1. Based on the obtained conditional tension diagrams, taking into account the area of the samples after fracture (determined from SEM images), true tension diagrams of CG and UFG states were constructed using the method described above.

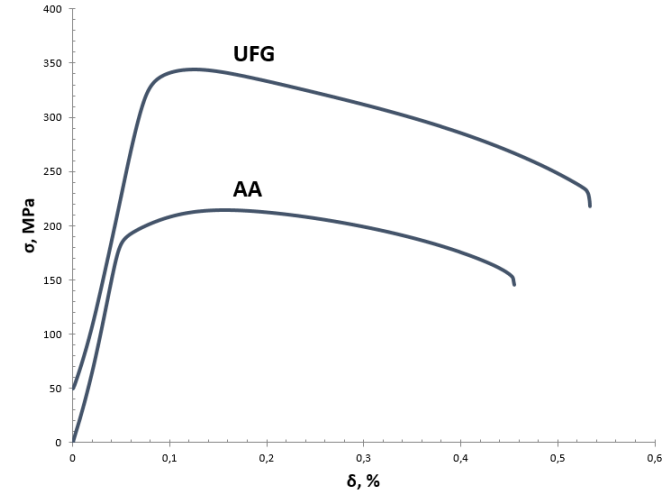

a)

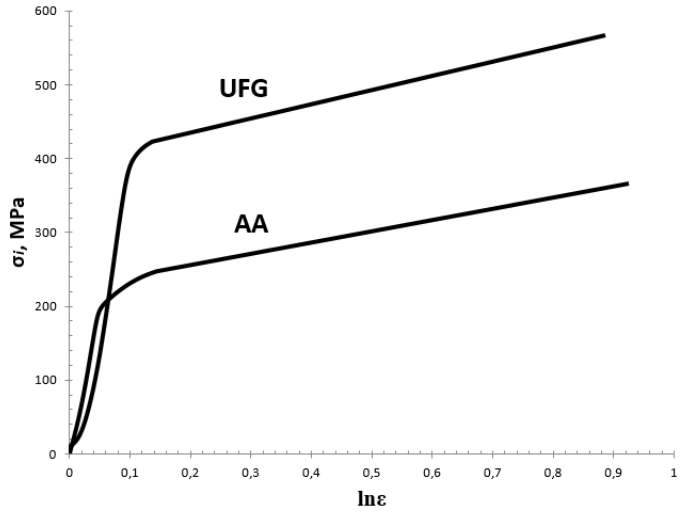

b)

Figure 3.2.5. True diagrams corresponding to the states of the samples without taking into account the change in the section.

Table 3.2.2. Mechanical characteristics of the alloy.

Structure state/	$\sigma_{0.2}$, MPa	σ_V,MPa	ε_{unif}, %	ε, %	σ_{idestr}, *MPa*	e_{destr}
CG	230	265	2	45	365	0.92
UMP	304	351	5	46	565	0.95

where δunif(%) - uniform deformation.

Table 3.2.2 presents the values of mechanical characteristics determined from the curves for CG and UFG structures. Experimental data showed an increase in strength and yield strength by 25% for a material with an UFG structure relative to a coarse-grained material. Similar results of experimental studies for the 6101 alloy after applying the ECAP-C method were presented in [18, 19]. It can also be concluded that the true strains before fracture of the 6101 alloy in the ultrafine-grained and coarse-grained states are equal, provided that the measurement error is taken into account, as well as the increased value of the true fracture stress of the UFG samples relative to the samples in the CG state.

3.3. Determination of the initial stage of destruction - the beginning of the formation of pores

At the initial stage, an experiment was carried out to establish the first stage of destruction, at which pores appear inside the material. To do this, samples in different states were stretched to different stress values, i.e. experimentally determined the stresses/strains at which the samples began to break down by forming pores inside them, without cracking.

Initially, the presence of pores was assessed by optical microscopy and, if the cut surface was free of defects, therefore, pores had not yet formed, and the selected mechanical test stop mode was not suitable for the task. Next, the stress was increased by 50 MPa with each step until defects in the form of pores were found when examining axial sections on a microscope. After that, the axial slices were examined in detail by SEM methods.

If the stretching was carried out to σmax and the experiment was stopped, and no pores were found inside, then the samples had not yet reached the first stage of the destruction process. If stretching was carried out up to ε*≈40% which in terms of true deformation is e*≈0.7, then the samples have not yet been destroyed, but cracks have already formed inside the samples, which symbolizes the second stage of destruction - when the pores have already united / merged into cracks. As a result, a stretching mode was established, in which the appearance of pores inside the material was recorded:

Figure 3.3.1 and Figure 3.3.2 show diagrams corresponding to tests with tensile stop at ε* (e*).

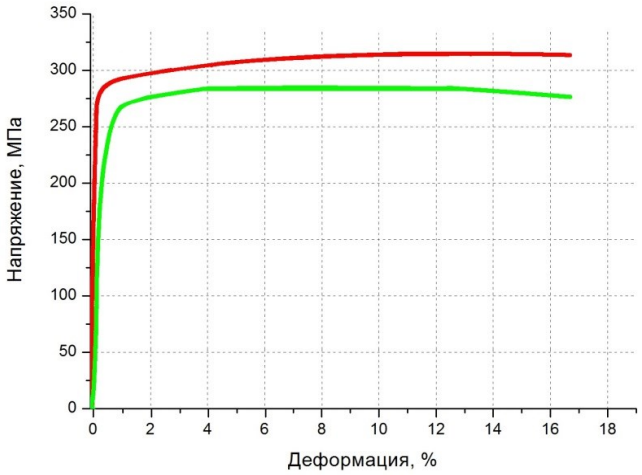

Figure 3.3.1. Stress-strain diagram for samples of CG structures under loading not to failure.

To detect the presence and evaluate the size and position of pores in the material structure, after mechanical tests, the deformed samples were cut along the axis on an ARTA 123-PRO EDM machine with a precision of 1–2 μm. The surface of the axial cut was ground and polished to a surface roughness of 50 nm. The surface structure of the axial section of the samples was studied by SEM.

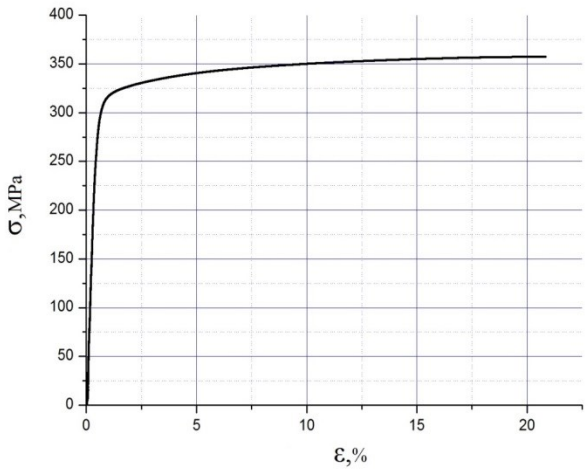

Figure 3.3.2. Stress-strain diagram for samples of the UFG structure under loading not to failure.

As a result, the experiment was carried out as follows: first, tension was carried out to failure, ε* was experimentally determined on the basis of the data obtained: in the control mode for achieving this deformation, the tensile experiment was stopped for each type of sample. If destruction occurred at ε≈45%, then ε*<45% was considered, i.e. to start ε*≈44%, but either cracks were recorded inside the material, or the sample was destroyed when removed from the installation fixtures. For ε*≈40% managed not only to stop the experiment before the destruction of the samples and remove them from the grips of the machine, but also to fix the formed pores that have not yet merged into cracks, which, in turn, symbolize the second stage of the destruction process.

3.4. Determination of microhardness change of Al-6101 alloy in coarse-grained and ultrafine-grained state

The microhardness of alloy samples in various states after stretching to failure was studied. The microhardness was measured directly next to the fracture region (where the deformation reached its maximum ε=0.5), in the region of 1.5 mm from the fracture, and on undeformed specimen grips. Studies have shown that the value of microhardness in the grip area of the samples is the highest in the UFG state, and in CG the values are slightly lower (about 100 units) and are approximately equal within the measurement error. In the area of the middle of the working base, the microhardness of all samples increases, since there is some work hardening in the materials due to deformation. The maximum increase in microhardness for all states is observed in the region close to the fracture, where, accordingly, the maximum narrowing deformation occurs. The microhardness in the fracture region increases for all states by approximately 10 units (about 10%) compared to the undeformed region. This reflects work hardening (strain hardening after exceeding the yield strength) and hardening of the material during deformation to tensile failure, and hard work and hardening of the CG and UFG material occurs approximately equally.

Table 3.4.1. Microhardness change data on samples in various states after stretching to failure

State	Base	1.5 mm from break	kink
CG	94.0	111	130
	94.8	99.4	116
	91.8	104	112
	90.9	102	111
	91.5	109	129
	92.4	98.1	112
	91.8	95.8	128
	93.6	98.9	115
Avg.	**93**	**102**	**119**
UMP	128	129	140
	129	129	134
	126	133	137
	128	134	132
	121	131	133
	126	131	141
	129	130	140
	126	129	113
Avg.	**127**	**130**	**134**

Chapter Conclusions:

- The relative strain before failure is~50% and does not depend on the type of alloy structure.
- Samples with an ultrafine-grained structure, obtained by the ECAP-C method, show strength by 25% higher than samples in a coarse-grained state after standard heat treatment.

- The increase in strength is associated with a change in strength due to grain refinement during ECAP-C, which is added to a change in strength due to dispersion strengthening (resulting from natural aging after ECAP-C).
- The increased true fracture stress of the UFG state determines its increased resistance to crack formation.
- The true deformation experienced by the material before the formation/opening of cracks and further destruction of samples of alloy 6101 both in the CG state and in the UFG state, taking into account the measurement error, is the same, and is equal toe*=0.7.

Publications on the research topic:

[76] Magomedova, D.K. Investigation of the mechanical properties of coarse and fine-grained Al-6101 UNDER STATIC tension / Magomedova, D.K., Efimov, M.A., Ryabokon, D.V. // Technical program and abstracts of the school young scientists "Structure and properties of high-entropy alloys and coatings". 2019 . C.43-44.

[77] Magomedova, DK Mechanical behavior of coarse- and fine-grained Al-6101 samples of different geometry under tension / Magomedova DK, Gunderov, DV, Efimov, MA // IOP Conference Series: Materials Science and Engineering. 2019. 672.

[78] Magomedova, D.K., Churakova, A.A., Stress distribution in static tension of cylindrical samples from fine- and coarse-grained aluminum alloy 6101, Nanoindustriya. 2021. Issue 1.

[79] Magomedova, D.K. Influence of geometry and grain size on the mechanical properties of Al 6101 under static tension of cylindrical samples / Magomedova D.K. // materials. technologies. Design, Bulletin of USATU, Ufa. Volume 3. No. 2(4). C.20-24.

[80] Magomedova, DK The dependence of mechanical properties of Al-6101 alloy on geometry of the samples with a groove during tensile tests / Magomedova DK, Gunderov DV , Mavlutov AM //Journal of Physics: Conference Series. - 2021.- 1967(1).- 012023.

Chapter 4. The results of the study of the surface of fractures and the axial section of the samples after stretching by SEM methods

4.1. Investigation of the surface of fractures of samples

a)

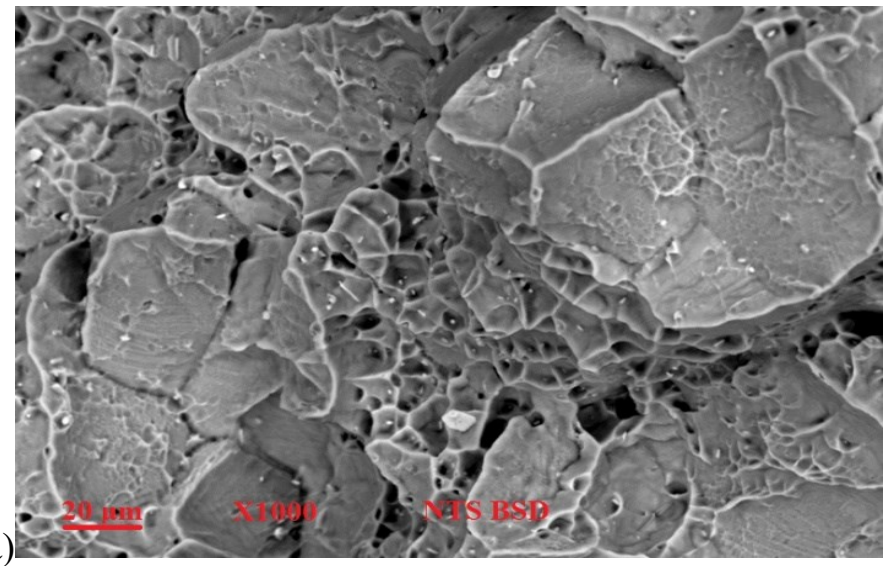

b)

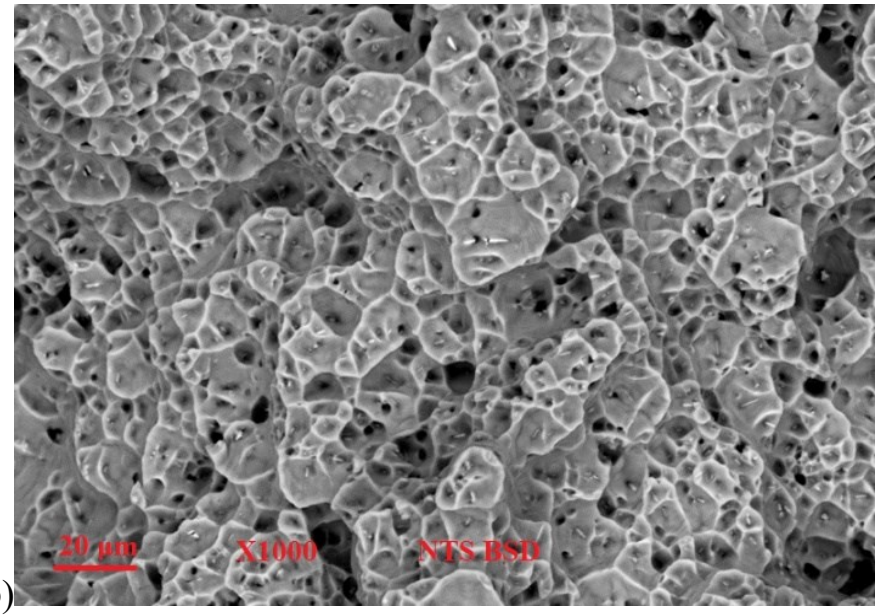

Figure 4.1.1. General view of the destruction area of samples with: a) CG; b) UFG structure.

As can be seen from the images shown in Figure 4.1.1, the fracture surface of the samples after static tension at room temperature is formed by pits and is predominantly ductile. Fractures have a generally homogeneous structure. On Figure 4.1.2.a histogram of the diameter of fracture pits in CG and UFG structures is presented.

The pits are the places of primary formation of pores during the stretching of the material, which later united and formed cracks, which merged into large cracks, along which the samples collapsed. Fracture pits are the centers of origin of "destruction" and their study is of particular interest.

To detect the content of particles of secondary phases and/or Al-Fe intermetallic particles in the pits of the fracture surface were chemically analyzed in the mode back scattered electrons (BSE).

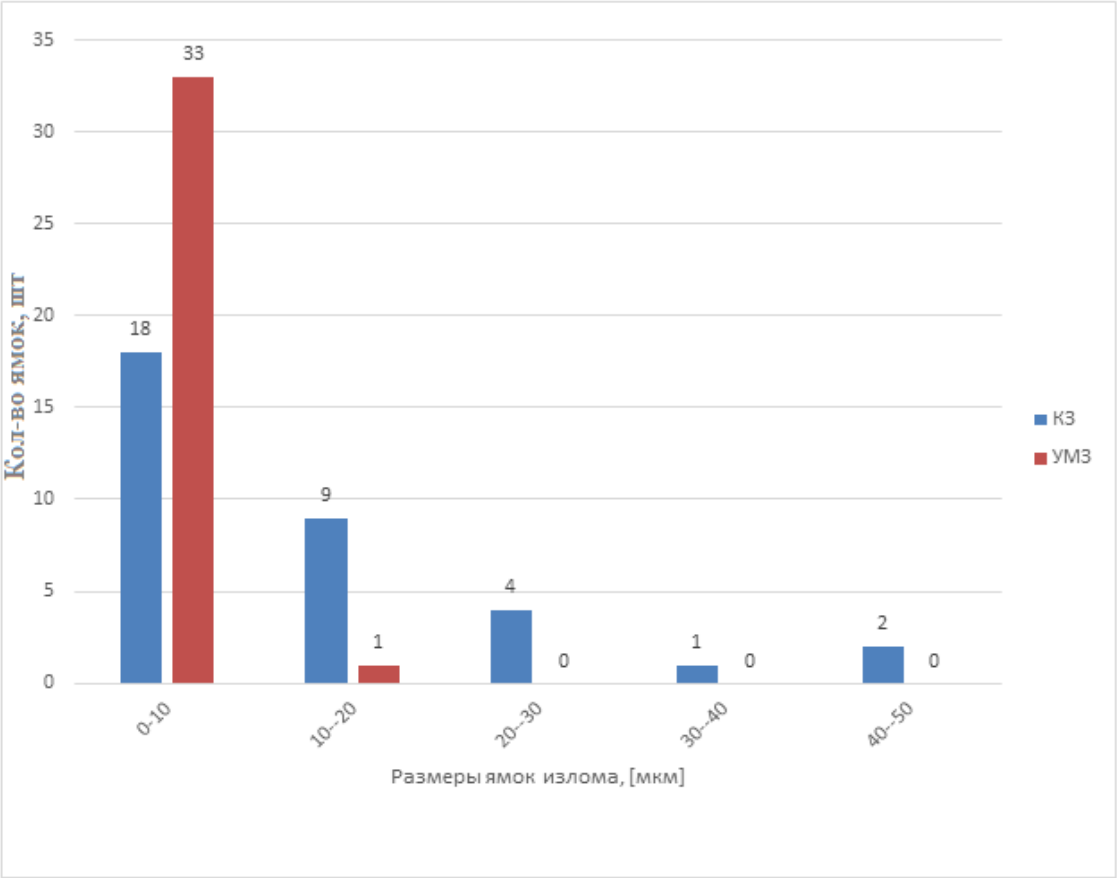

Figure 4.1.2.Histogram for the diameter of fracture pits in CG and UFG structures.

The figures below show examples of selected areas on fracture surfaces and tables with average abundances of the corresponding elements (backscattered electron (BSE) mode).

In Table 4.1.1. the average values of the elements are given, corresponding to the presented spectra in Figure 4.1.3. and Figure 4.1.4, respectively, according to their structural states.

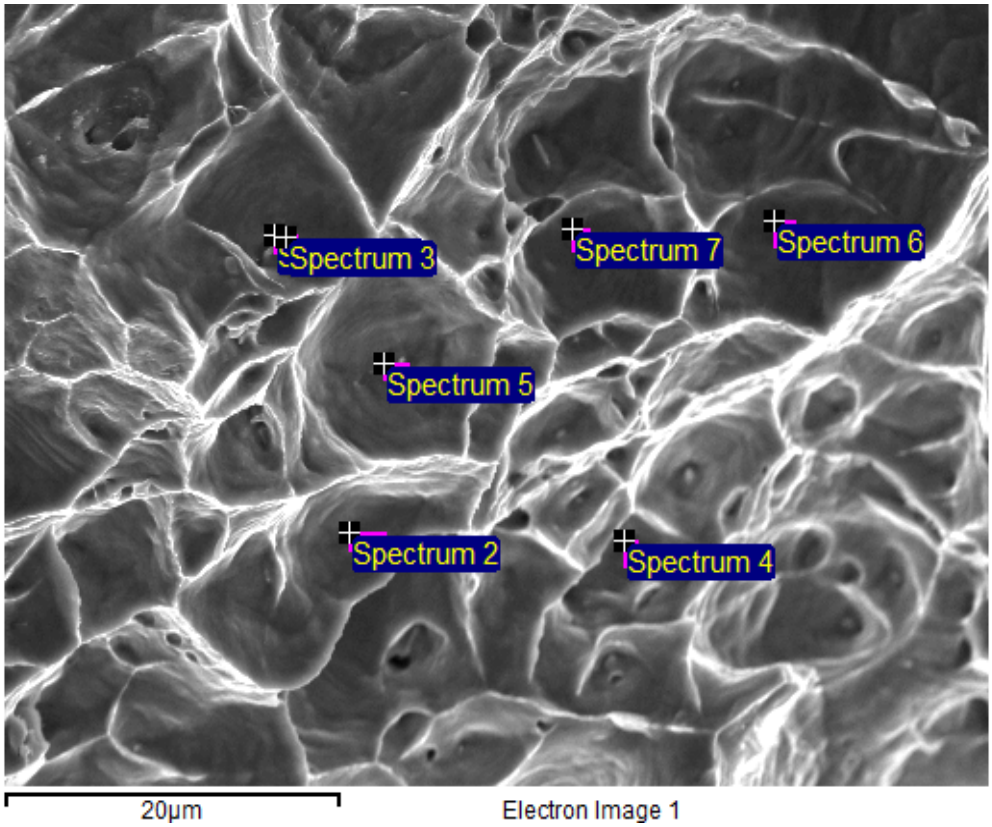

Figure 4.1.3. Fracture surface of a specimen with a CG structure.

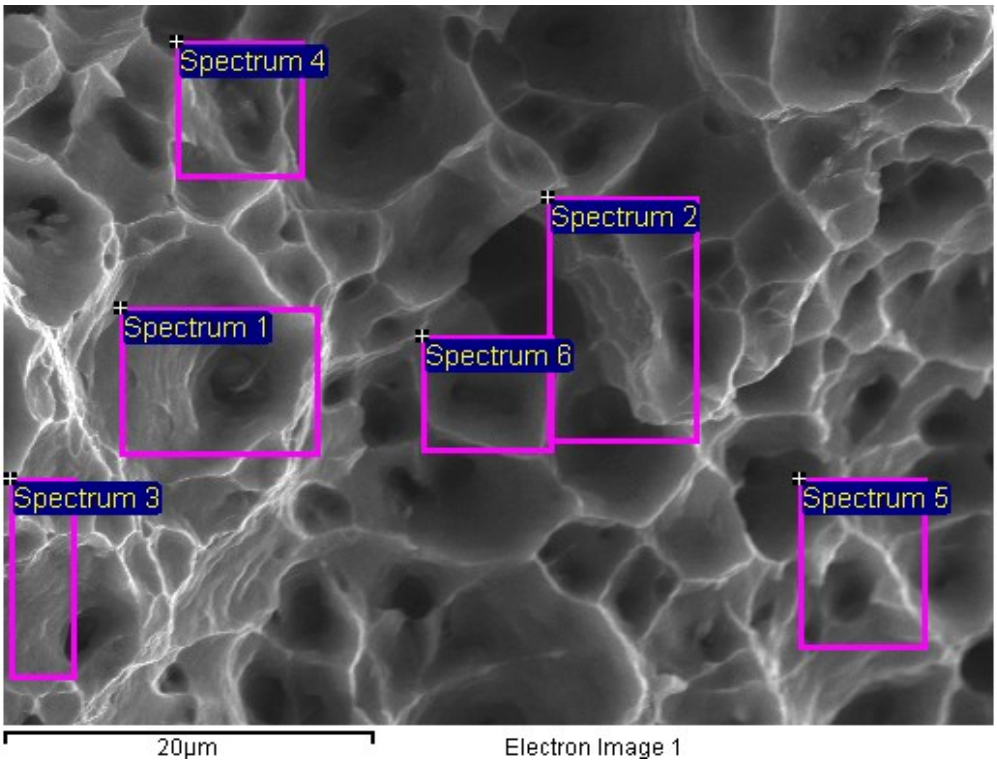

Figure 4.1.4. Fracture surface of the sample with UFG structure.

Table 4.1.1. The average content of elements in the fracture pits of CG and UFG samples according to spectral analysis data for the main elements in Figures 4.1.3 and 4.1.4. respectively.

	Mg(wt.%)	Si(wt.%)	Fe(wt.%)
Average content of elements in CG material	1.5	2.97	4.74
Average content of elements in UFG material	0.93	0.46	0.45

An analysis of the fracture surface spectrum shows (Table 4.1.1) that the fracture surface in the CG state contains a large percentage of Fe. At most points of measurement of the chemical composition of specimen fractures in the CG, the content of Fe is increased. Fe does not dissolve in the aluminum matrix, it is an impurity, its amount is small, but on the basis of Fe, large precipitates of micron size are formed. Large (several microns in size) particles of Al-Fe intermetallic compounds, formed at the stage of casting, are the areas of nucleation of pores and subsequent destruction of Al alloys after AA in tension. Accordingly, these intermetallic particles are in high content on the fracture surface in the depth of the pits, and the fracture spectrum shows an increased Fe content, which is many times higher than the average Fe content in the alloy. At the same time, when analyzing the chemical composition of the ECAP fracture surface, it can be seen that the state differs markedly from the chemical composition for NA: the Fe content on the ECAP fracture surface is noticeably lower. Presumably, this is due to the fact that after ECAP, the nature of destruction changes, since The regions of pore nucleation and subsequent destruction may be other structural elements, for example, regions of higher dislocation density, defects formed during ECAP, and iron intermetallic compounds no longer play a decisive role in the formation of the fracture surface, or they are also somewhat refined during ECAP, which leads to their smaller contribution to destruction.

The analysis of the images of the surface of the fractured samples presented in Figures 4.1.1, 4.1.3, 4.1.4 corresponds to the description of ductile fracture - the pits correspond to uniaxial tension with inclusions.

Conclusions for the section:

1) The surface of the fractures is pitted and has a homogeneous structure;

2) The size of the pits on the surface of fractures for samples with a CG structure can be estimated with a size of up to 10 μm, for samples with a UFG structure, up to 5 μm. This indicates that in the UFG state during destruction, a large number of microdefect nucleation centers were simultaneously involved, relative to the CG state.

3) The fracture surface of the CG state contains a large percentage of Fe, which exceeds the average Fe content in the alloy. Large particles of Fe-Al intermetallic compounds are the areas of nucleation of pores and subsequent destruction of CG states under tension, and intermetallic particles based on Fe in a large content are on the fracture surface.

4) The Fe content on the fracture surface of the UFG state is noticeably lower than in the CG state; therefore, the centers of nucleation of pores and the "source" of destruction will be to a greater extent other defects/elements of the structure.

4.2. Study of the axial section of Al 6101 specimens obtained under static tension up to deformation ε≈40%

In order to more fully assess the influence of the structure on the process of destruction, a study was made of the structure of the samples stretched to the values of true deformation (e*=0.7). Samples stretched to e*,cut along the axis on an electro-erosion machine ARTA 123-PRO with precision 1-2 μm. The cut surface was ground and polished to a surface roughness of 50 nm and then examined using electron microscopy. In this case, again, the structure of the material was of interest, but already inside the sample itself.

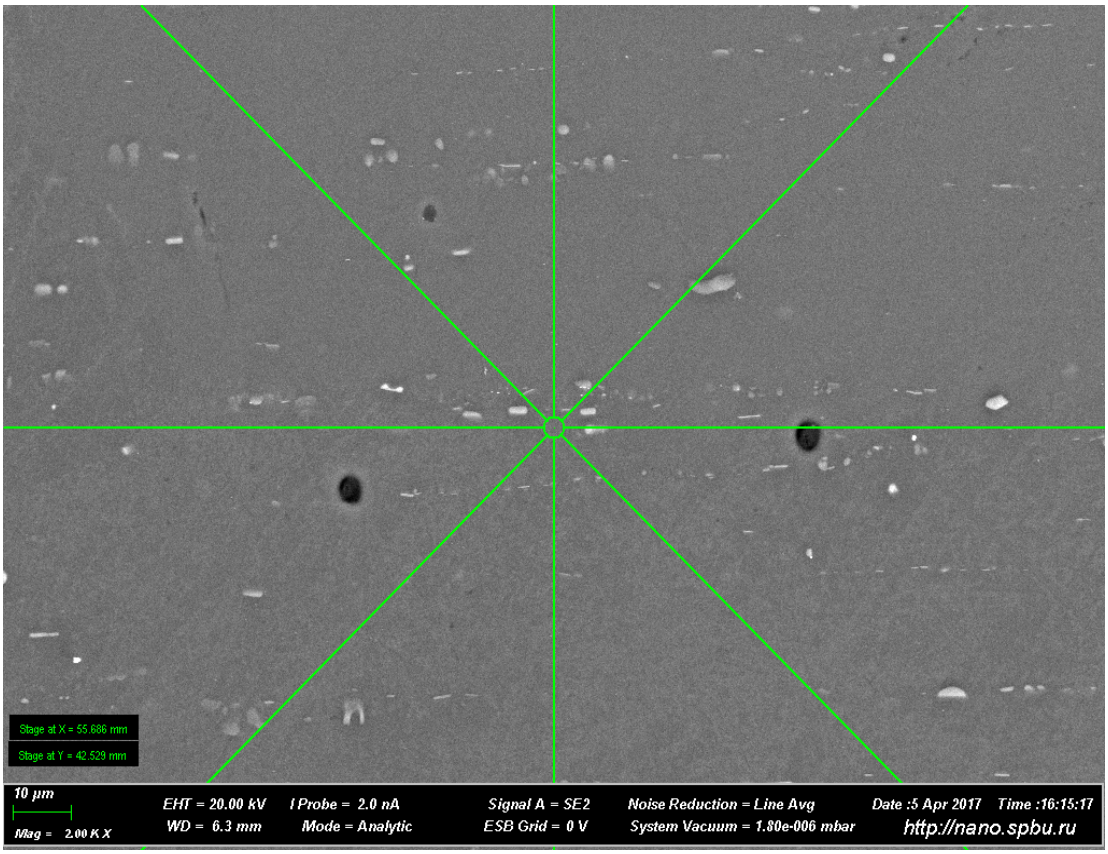

Figure 4.2.1. Photograph of the axial section of a sample with a CG structure after stretching to ε*.

Figure 4.2.1. is a SEM image of the axial section for a CG specimen. Below is a snapshot of the surface of the axial cut of the CG sample with the pore sizes applied to the corresponding places.

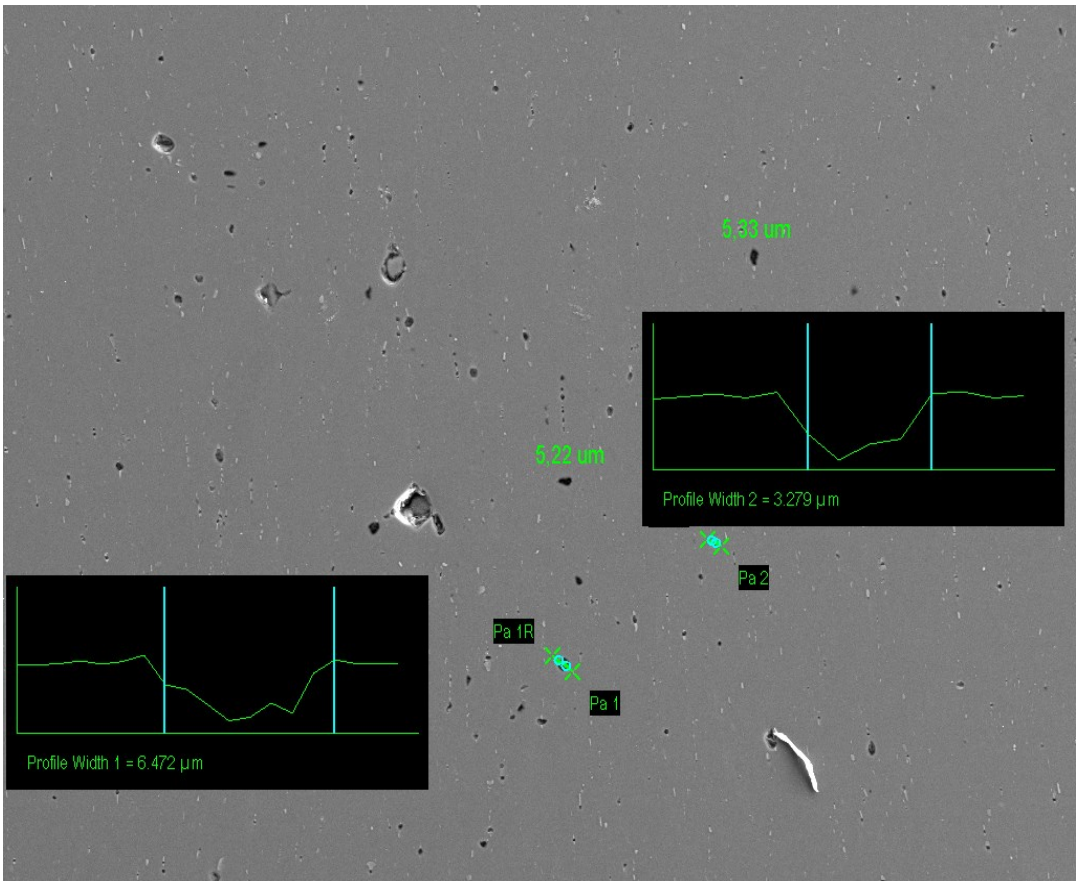

Figure 4.2.2. Photograph of the axial surface of a sample with a CG structure with pore sizes after stretching toε* (automatic markers are supplied to change the distance and depth of the measured defect).

Samples with a UFG structure were considered similarly. For comparison, Figure 4.2.3 shows two images: for a sample with a CG structure and a sample with a UFG structure. One can clearly see the presence and location of pores in both types of structures, as well as the difference in their sizes, according to the markers.

a)

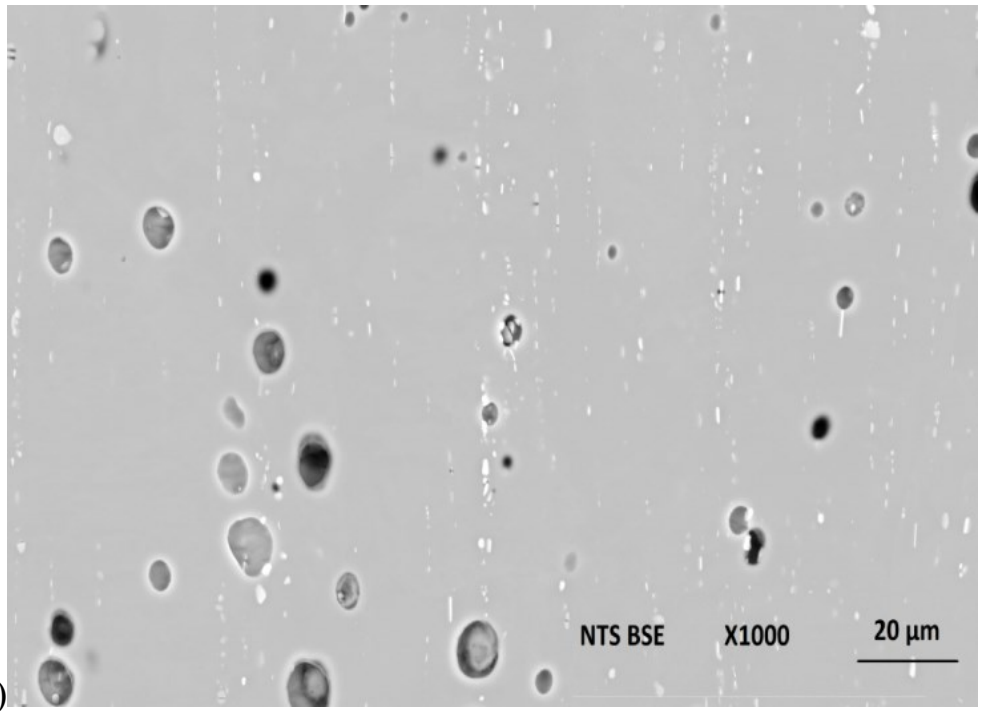

b)

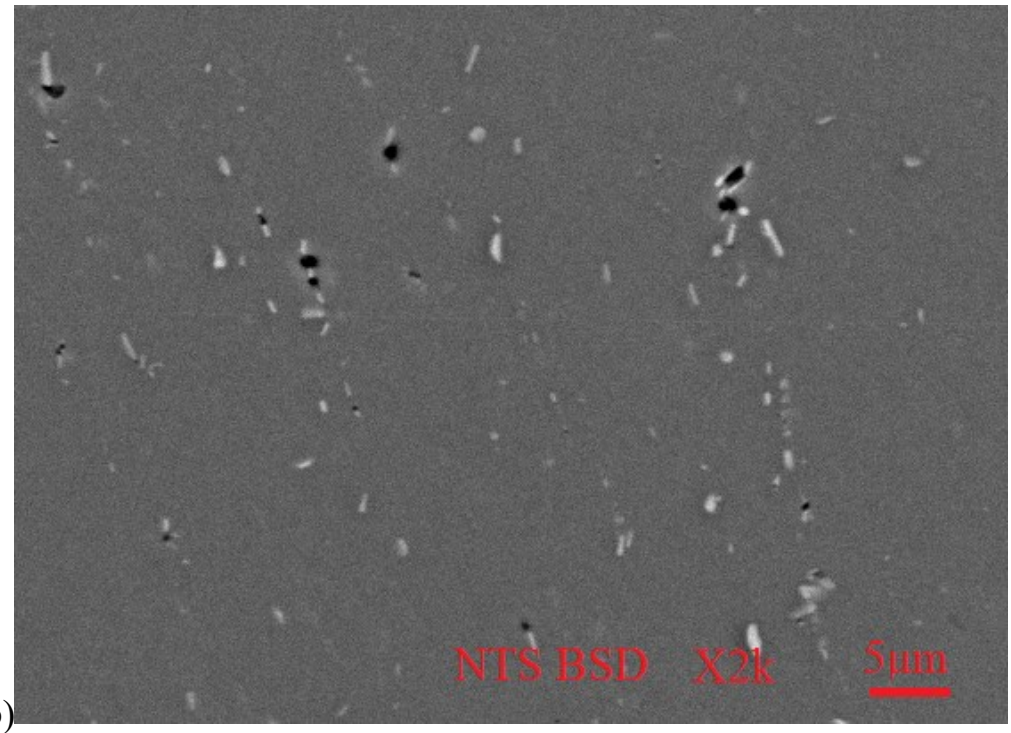

Figure 4.2.3. . Photograph of the axial surface of the sample with: a) CG, b) UFG structure with pores after stretching to ε*.

As a result, the average pore sizes were determined at the stage of deformation ε*, at which they were fixed. The data obtained were combined and presented in Table 4.2.1 and Figure 4.2.4.

Table 4.2.1. Average pore size for material with CG and UFG structure.

Structure type	Pore size in tension up to ε*, μm
CG	3-7
UMP	1-2

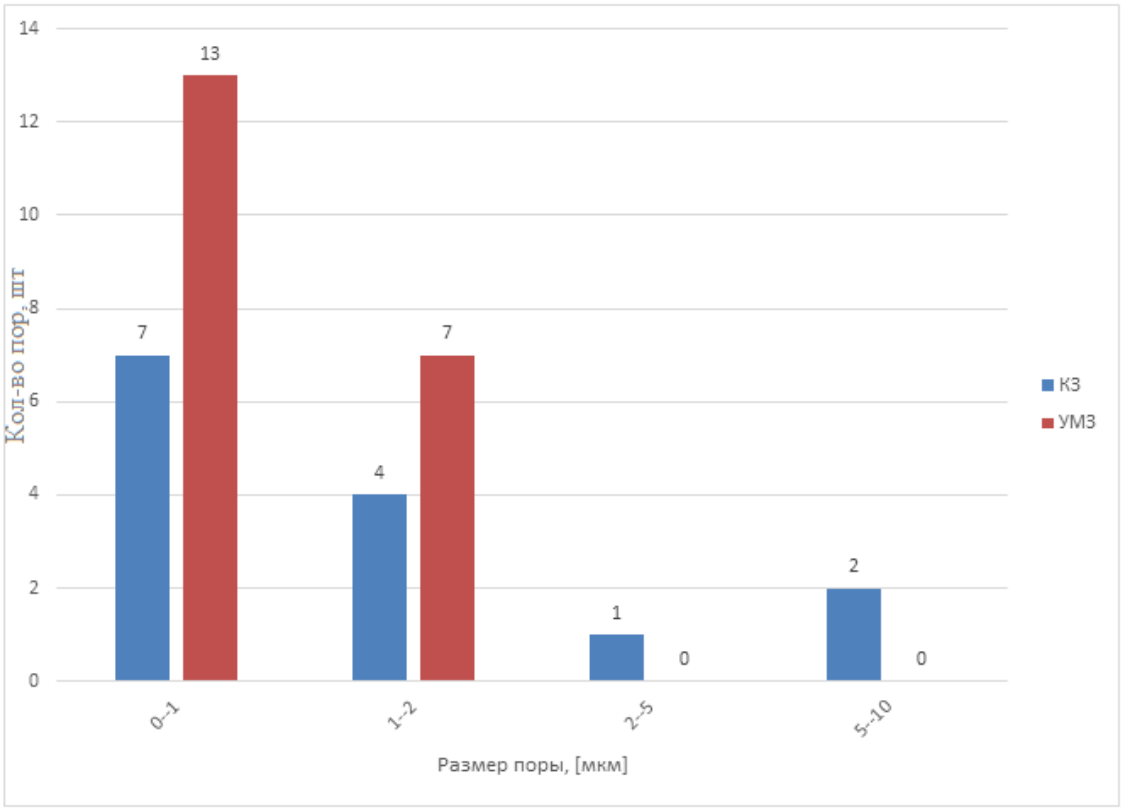

Figure 4.2.4. Histogram of pore distribution in CG and UFG samples after stretching to ε*.

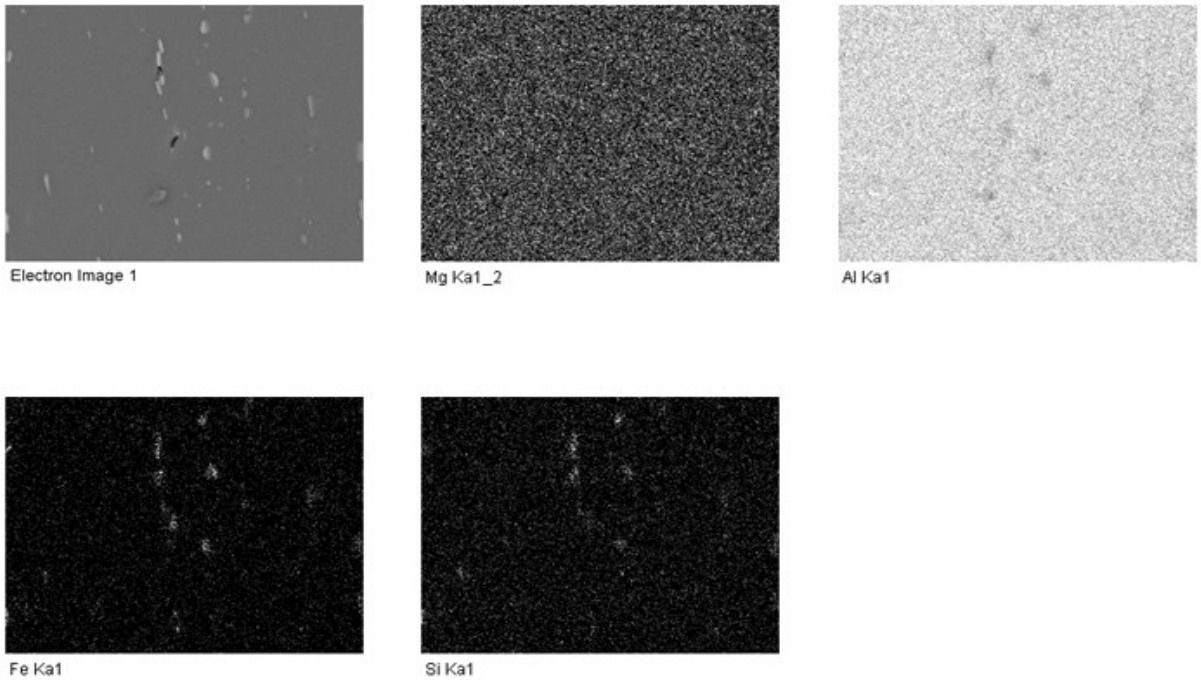

Figure 4.2.5. Electronic map of the distribution of elements over the surface of the axial cut of the sample with a CG structure.

To determine the centers of nucleation of pores, a chemical analysis of the surface of axial sections of samples of three types of structures was carried out (Figure 4.2.5 and Figure 4.2.6). Table 4.2.2 shows the values corresponding to the spectra presented in Figure 4.2.6:

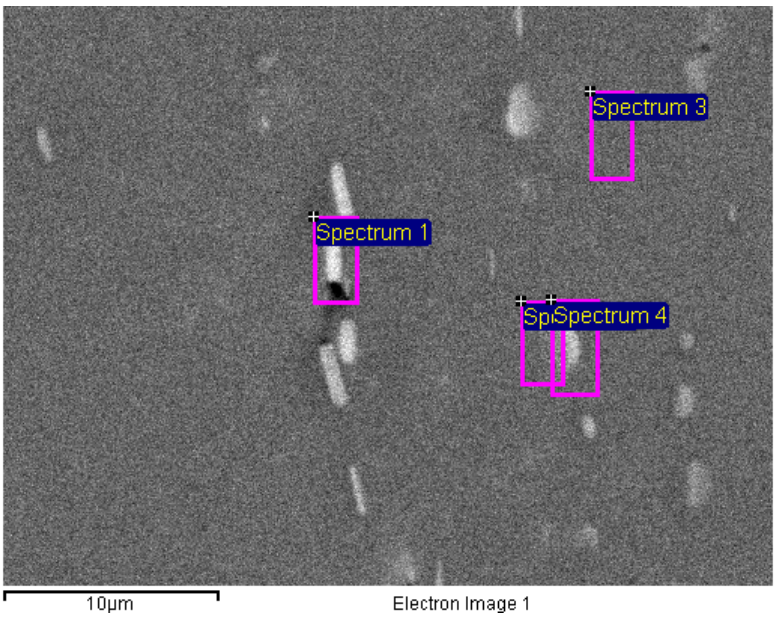

Figure 4.2.6. The surface of the axial cut of the sample with a CG structure and the corresponding spectra after stretching to ε*.

Table 4.2.2. The content of elements in the limited area of the sample, presented in Figure 4.2.6.

	Mg(wt.%)	Si(wt.%)	Fe(wt.%)
Spectrum 1	0.72	3.56	1.76
Spectrum 2	0.78	2.35	1.87
Spectrum 3	-	-	-
Spectrum 4	0.95	2.31	1.44

Spectra 1,2,4 correspond to the region of pores, and spectrum 3 is outside the pore, and the values of the measured characteristics were lower than the sensitivity of the instrument. As can be seen from the table, the presence of Al-Fe particles is indeed observed in the region of formed pores, which confirms the earlier conclusion.

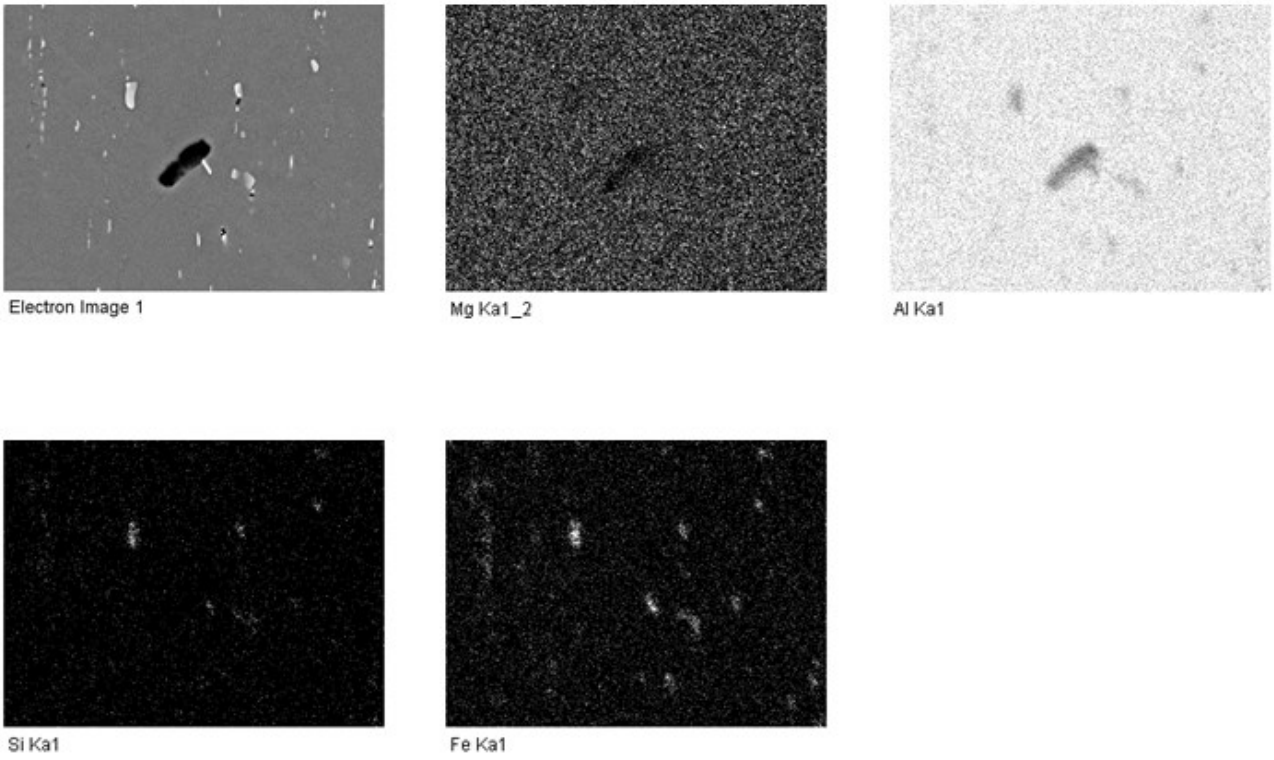

Figure 4.2.7. Electronic map of the distribution of elements over the surface of the axial cut of the sample with UFG structure after stretching to ε*.

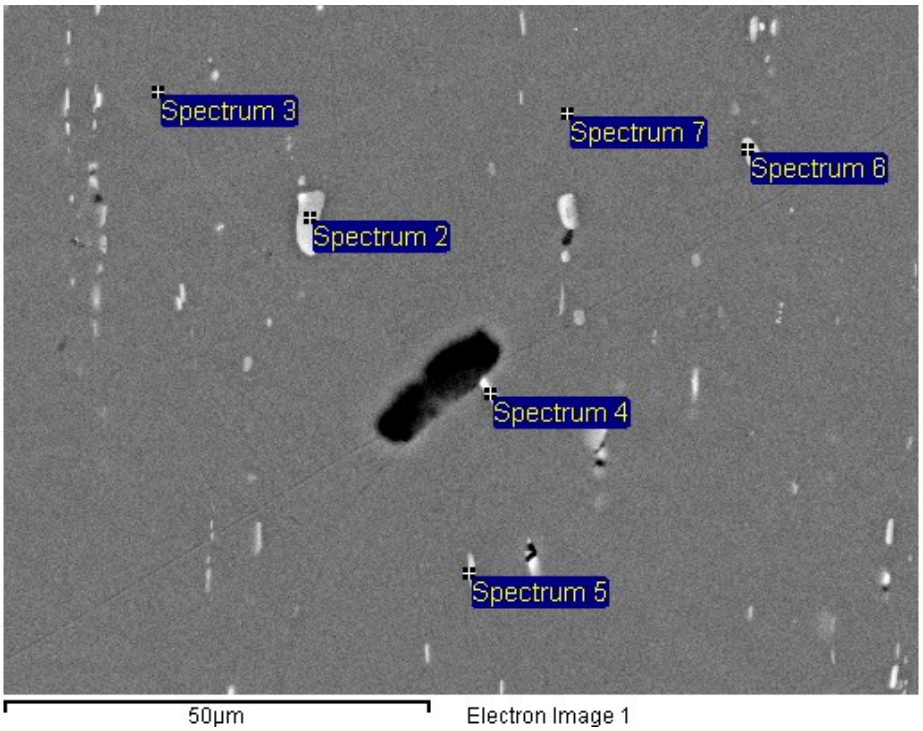

Figure 4.2.8. Axial cut surface of a sample with UFG structure and corresponding spectra after stretching to ε*.

Samples with UFG structure were studied similarly (Figure 4.2.7 and Figure 4.2.8). In Table 4.2.3. the values corresponding to the spectra presented in Figure 4.2.8 are given.

Table 4.2.3. The content of elements in the limited area of the sample, presented in Figure 4.2.8.

	Mg(wt.%)	Si(wt.%)	Fe(wt.%)
Spectrum 1	0.66	0.40	0.09
Spectrum 2	0.62	6.97	4.61
Spectrum 3	0.76	-	-
Spectrum 4	0.71	1.06	1.74
Spectrum 5	0.83	0.64	-
Spectrum 6	0.83	0.63	-
Spectrum 7	0.81	-	-

Spectra 2 and 4 correspond to particles that lie outside clearly visible pores. Also, Figure 4.2.8 shows that the Fe particles are not located in the pores. This also confirms the earlier assumption that Fe-Al particles are less likely to be areas of pore formation during fracture and, accordingly, are less likely to lie in the pits of the fracture surface.

Conclusions for the section:

1. The highest concentration of pores is located in the center of the sample, which corresponds to the region of maximum stress concentration.
2. The coarse-grained state corresponds to pores 3-7 μm in size, for the ultrafine-grained state - 1-2 μm.
3. As can be seen from the analysis of the chemical composition of the surface of the deformed samples, Fe particles are observed in the alloy in the pores of the alloy with a CG state.
4. Al-Fe particles in the pores of the alloy with the UFG state are fixed less frequently than in the CG state. Therefore, the reason for the established difference in the content of Fe may be the following: during the processing of the ECAP alloy, the Fe-Al intermetallic particles in aluminum are redistributed and refined, and the Fe-Al particles are less likely to be areas of pore formation during destruction and, accordingly, less likely to lie in the pits of the fracture surface.

4.3. Study of the axial section of Al 6101 specimens after destruction

In order to more fully evaluate the effect of the structure on the fracture process, we also studied the structure of the studied samples after tension immediately before fracture.

Broken specimens, cut along the axis on an electroerosive machine ARTA 123-PRO with precision 1-2 μm. The area corresponding to the capture area was also removed - the working part of the sample (5-7 mm long) was considered. The cut surface was further ground and polished to a surface roughness of 50 nm. In this case, again, the structure of the material was of interest, but already inside the fracture itself. The structure of the surface of the axial section of the samples was studied using electron microscopy by SEM methods.

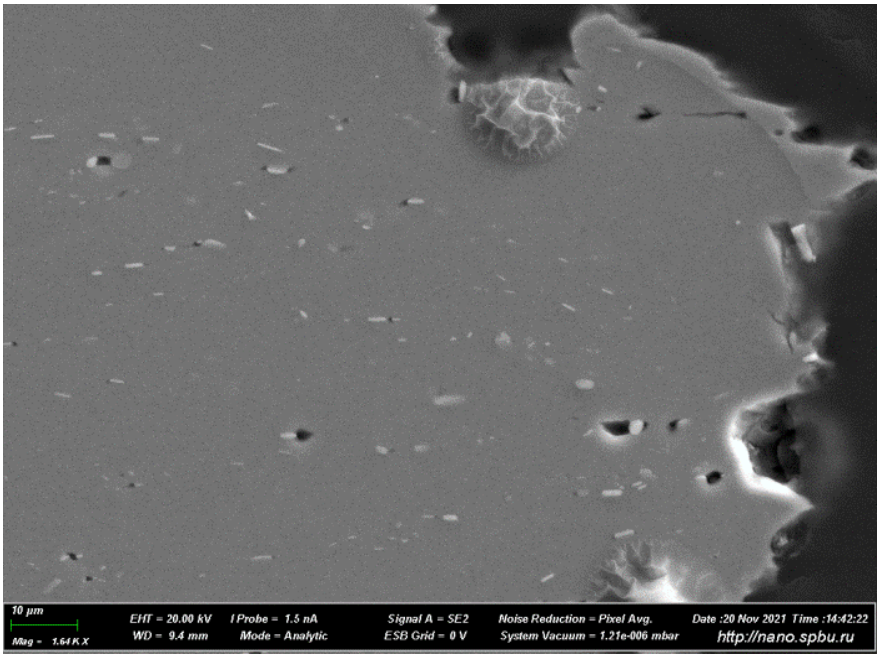

Figure 4.3.1. Axial slice image of a fracture sample with a CG structure with a fracture boundary, after deformation to failure.

In Figure 4.3.1. presented by SEM-snapshot of an axial section of a fracture sample with a CG structure with a fracture boundary, after deformation to fracture: the presence of pores and light particles is visible, as in the case of studying axial sections of specimens deformed not to fracture. Figure 4.3.2. presents the same image with filters for the elements Mg, Si and Fe. Due to the possibility of element-by-element analysis of the surface of the presented axial cut, it is possible to determine the location of the main elements, the points of their accumulation or absence - this allows us to draw a conclusion about the elements on which destruction will occur.

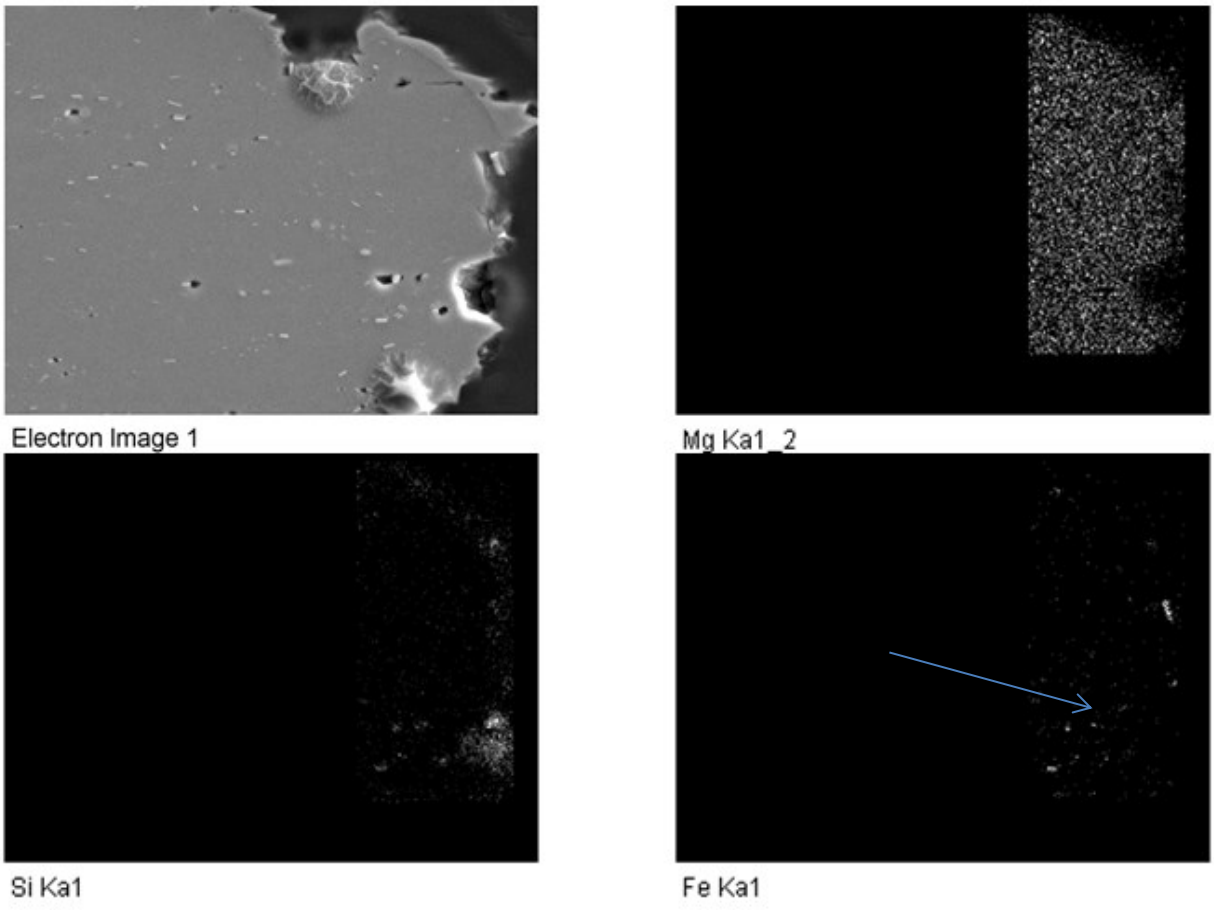

Figure 4.3.2. Axial slice image of a fracture sample with a CG structure and an electronic map of the distribution of elements over the fracture surface after deformation to failure.

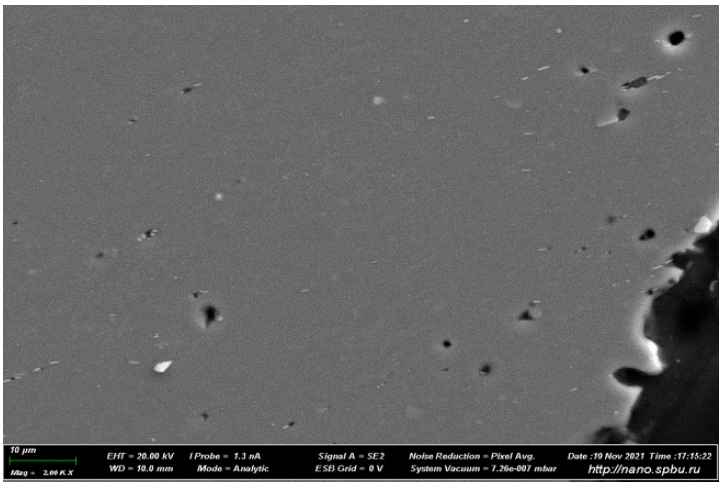

Figure 4.3.3. Axial slice image of a fracture sample with UFG structure with a fracture boundary.

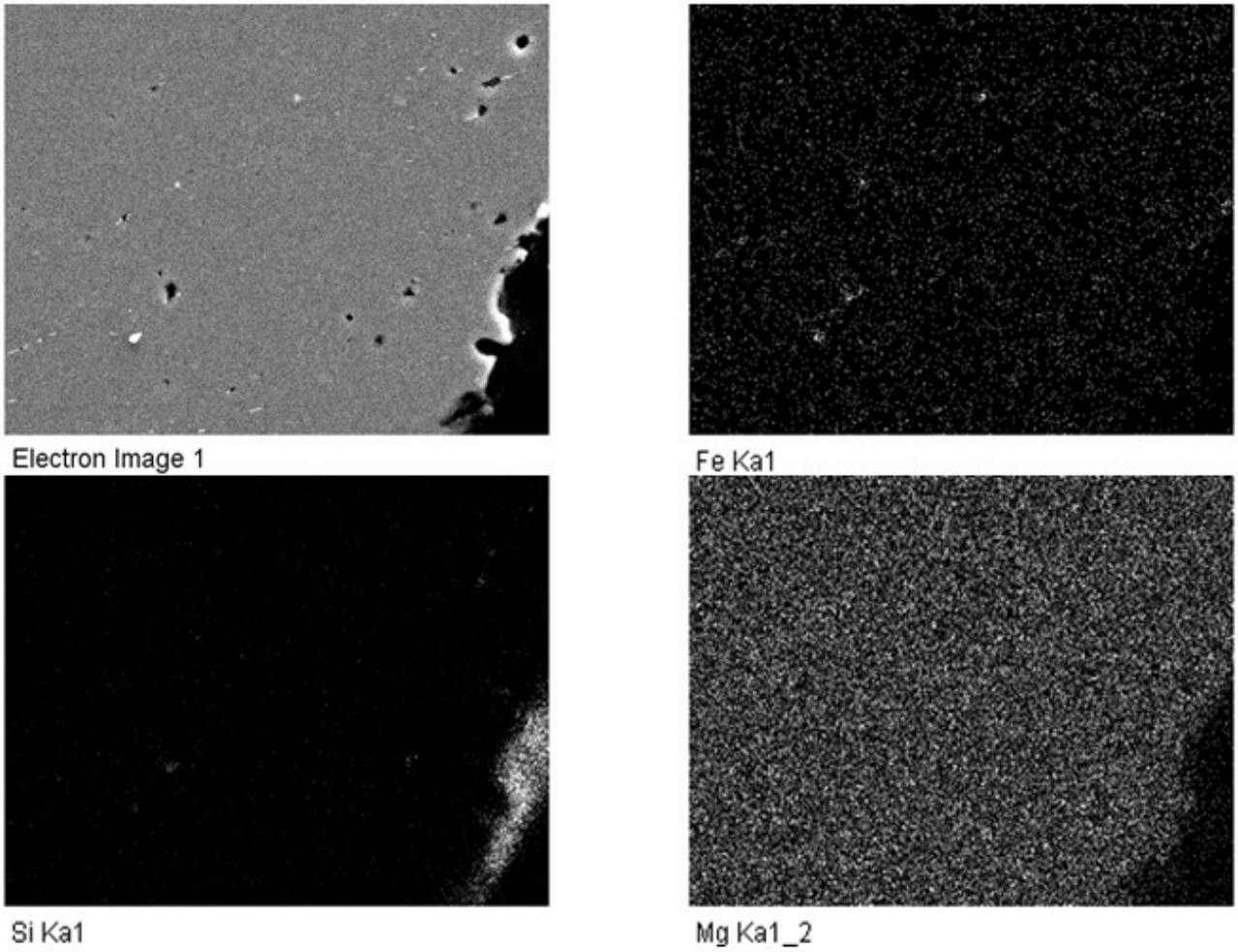

Figure 4.3.4. Axial slice image of a fracture sample with UFG structure and an electronic map of the distribution of elements over the fracture surface

In Figure 4.3.3. presented by SEM-snapshot of an axial section of a fracture specimen with a UFG structure with a fracture boundary, after deformation to failure: we also observe the presence of formed pores and light particles, as in the case of a similar specimen of the CG structure (Figure 4.3.1). Figure 4.3.4. presents the same image with filters for the elements Mg, Si and Fe: you can determine the location of the main elements, points of accumulation or absence.

Analyzing Figure 4.3.2. and Figure 4.3.4. it can be concluded that in the CG state at the fracture boundary there is an increased content of iron particles relative to the UFG state, since the Fe filter in Figure 4.3.2, which corresponds to the CG state, shows the accumulation of iron elements exactly along the edge of the fracture.

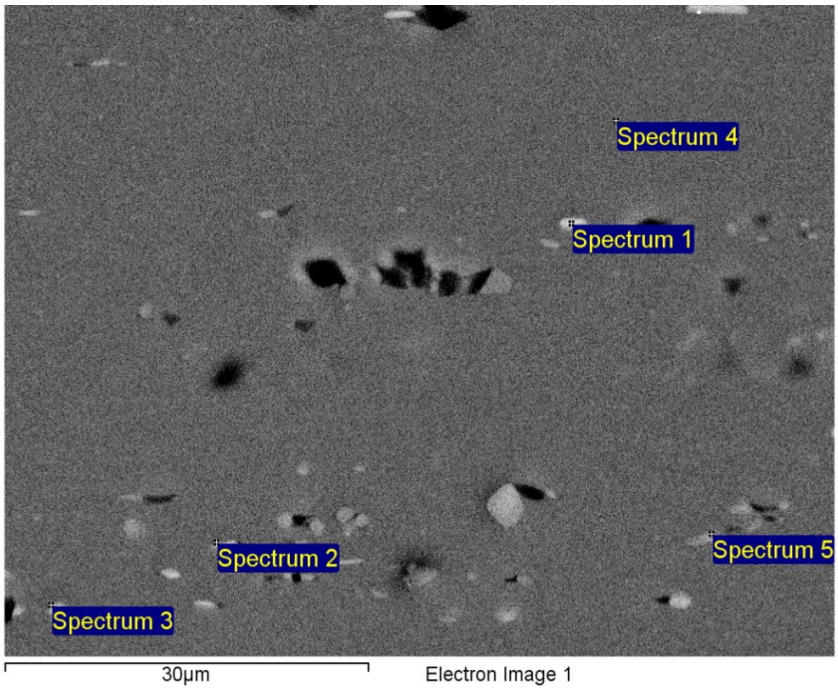

Figure 4.3.5.Axial cut surface of a sample with UFG structure and corresponding spectra.

Figure 4.3.5 shows the surface of the axial cut of the destroyed UFG sample. The white particles are iron intermetallics according to Table 4.3.1, and their location corresponds to areas outside the pores, which is confirmed by Figure 4.3.6 with filters of the main elements.

Table 4.3.1.The content of elements in the limited area of the sample, presented in Figure 4.3.5.

Spectrum	Mg(wt.%)	Al(wt.%)	Si(wt.%)	Fe(wt.%)
Spectrum 1	0.95	87.27	6.96	4.82
Spectrum 2	1.10	95.12	2.46	1.33
Spectrum 3	0.98	90.10	5.59	3.33
Spectrum 4	1.23	97.87	0.89	0.00
Spectrum 5	1.11	93.10	4.02	1.77
mean	1.10	93.45	3.55	1.90

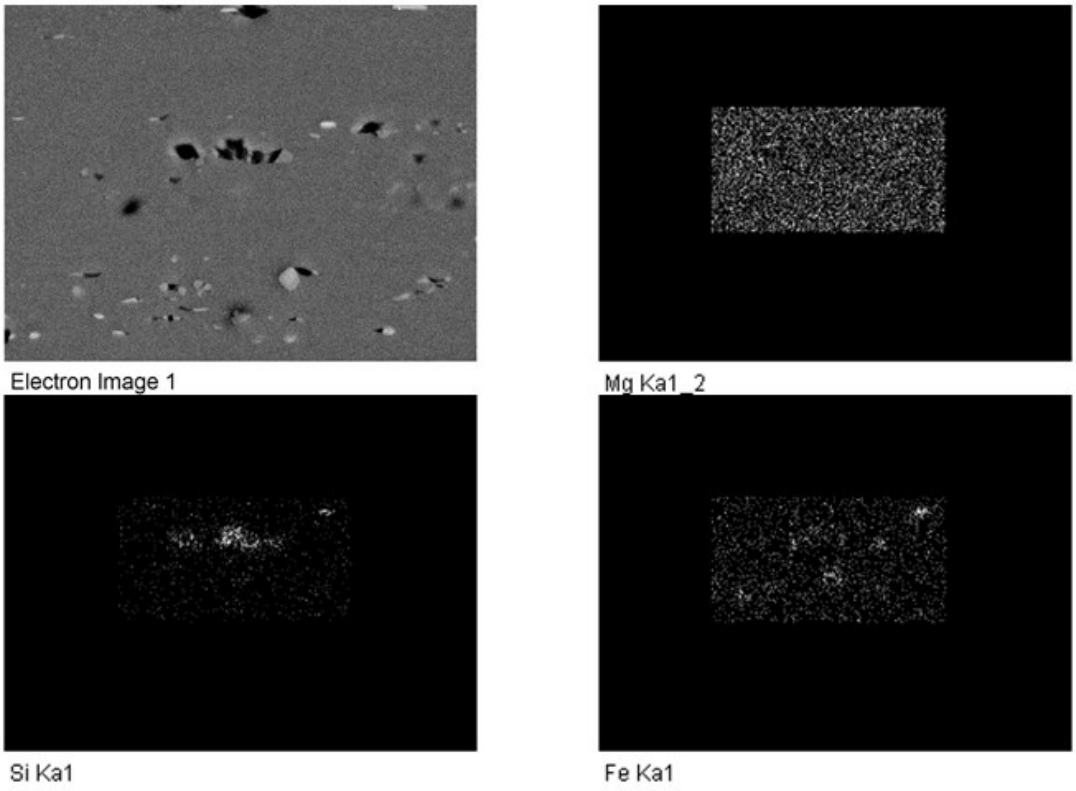

Figure 4.3.6. Axial slice image of a fracture sample with UFG structure and an electronic map of the distribution of elements over the fracture surface, corresponding to Figure 4.3.5

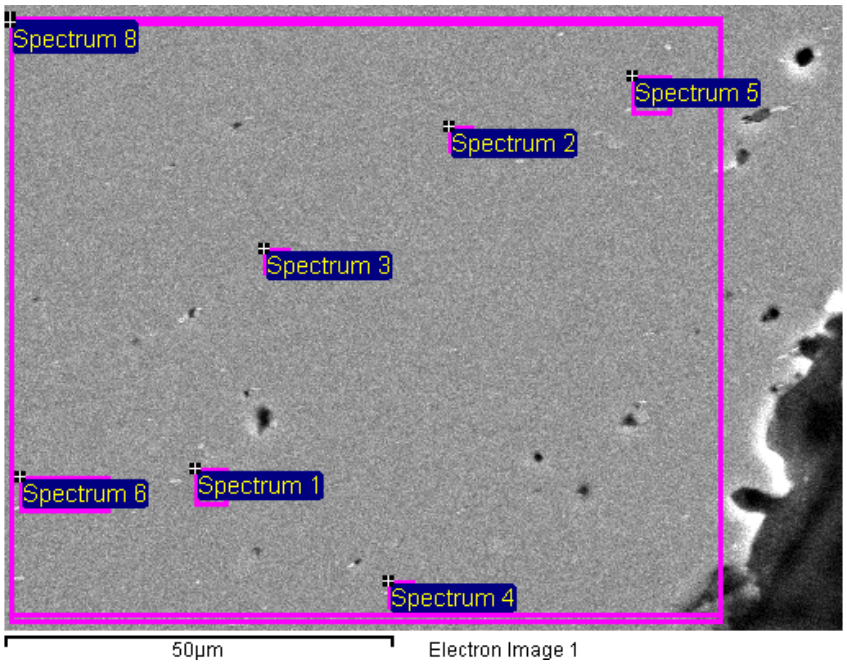

Figure 4.3.7.Axial cut surface of a sample with UFG structure and corresponding spectra at the fracture boundary after deformation before fracture.

Table 4.3.2.The content of elements in the limited area of the sample, presented in Figure 4.3.7.

Spectrum	Mg (wt.%)	Al (wt.%)	Si(wt.%)	Fe (wt.%)
Spectrum 1	0.93	96.45	1.49	1.14
Spectrum 2	0.85	95.94	1.73	1.48
Spectrum 3	0.89	97.18	0.92	1.01
Spectrum 4	1.01	97.57	1.00	0.42
Spectrum 5	0.95	98.08	0.70	0.26
Spectrum 6	0.93	97.83	0.90	0.34
Spectrum 7	0.89	98.55	0.56	0.00
Spectrum 8	0.89	98.67	0.44	0.00
mean	0.92	97.53	0.97	0.58

Figure 4.3.7 and Table 4.3.2 present data that confirm that the light particles in the images are Fe-based particles. The Fe content on the fracture surface of samples with UFG structure is noticeably lower than with CG structure. It was assumed that after ECAP-C, the nature of destruction changes, because The areas of pore nucleation and subsequent destruction may be other elements of the structure, and iron intermetallic compounds no longer play a decisive role in the formation of the fracture surface, or they are also somewhat crushed during ECAP-C, which leads to their smaller contribution to fracture." As the analysis of this chapter shows, indeed, ECAP treatment leads to a refinement of Al-Fe particles from 7 to 2 μm in alloy 6101, relative to its coarse-grained state.

Conclusions for the section:

- Al-Fe intermetallic particles in high content are on the fracture surface in the depth of Al pits of CG alloys under tension, and the fracture spectrum shows an increased Fe content, which is many times higher than the average Fe content in the alloy.
- The previously recorded increased content of Fe in the pits in the area of destruction is not due to the SEM measurement error, but rather the increased content of

Al-Fe particles at the bottom of the pits - since pores are more likely to form on Al-Fe particles at the initial stage of destruction, and, accordingly, after destruction.

Publications on the research topic:

[81] Magomedova, D.K. Influence of grain size on the process of pore formation in Al-6101 / Magomedova D.K. // Collection of materials "The Fourth Interdisciplinary Scientific Forum with International Participation "New Materials and Advanced Technologies"". 2018. Volume 1. P. 319-321.

[82] Magomedova, D.K. Study of the mechanical properties and fracture surface of Al-6101 cylindrical specimens under static tension / Magomedova, D.K., Churakova, A.A., Gunderov, D.V. // Proceedings of the VII International Conference "Actual problems of continuum mechanics". 2021. pp.167-171.

[83] Magomedova, DK Investigation of mechanical properties and fracture surface of cylindrical samples Al-6101 under static tension / Magomedova DK, Churakova AA, Gunderov DV // Journal of Physics: Conference Series. 2022. 012023.

[84] Magomedova, D.K. Influence of Al 6101 alloy structure on the formation of pores during static tension as a structural change during deformation / Magomedova D.K. // materials. technologies. Design, Bulletin of USATU, Ufa. 2022. Volume 4. No. 1(7). C. 24-29.

Chapter 5. Numerical simulation of the stress-deformation state under static extension of specimens Al 6101

For a better understanding of the features of deformation of CG and UFG samples, the simulation of the tensile process was also carried out to determine the stresses and strains at various points of the working base of the sample.

Scheme of the experiment. For finite element modeling of the stretching process, the Deform 3D software package was used. Figure 5 shows a schematic representation of the tooling and sample assembly. Tension was simulated on a tensile testing machine. To do this, workpiece 1 was fixed in holders 2 and 3. Holder 2 performs translational upward movement (the direction is indicated by an arrow), holder 3 is fixed.

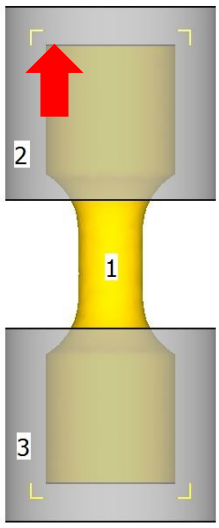

Figure 5. Assembly of 3D models of tooling and workpiece for modeling the stretching process: 1 – workpiece; 2 - upper holder; 3 - lower holder.

5.1. Boundary conditions and assumptions made

As the material of the initial workpiece, aluminum alloy Al 6101 in an artificially aged state was chosen according to the regime: annealing at a temperature of 550ºC for 2 hours, followed by quenching in water at room temperature, then for 12 hours the material was aged by annealing at a temperature of 170ºC [35,37]. Hardening curves and elastic properties are set on the basis of the tensile experiments. The workpiece material in the initial state is assumed to be plastic, isotropic, and there are no initial

stresses and deformations in it. A sketch of the workpiece with dimensions is shown in Figure 3.1.1.

Three-dimensional solid Models of the workpiece and tool were created in the CAD system - KOMPAS-3D, were solid and three-dimensional objects, and were saved in the "stl" format. A mesh of finite elements was formed in the form of tetrahedra, the number of which was 32,000 and was determined by preliminary calculations. The option to compensate for the volume of the workpiece model was activated. The stamping tool was an absolutely rigid solid body. The finite element mesh did not include tool models.

The speed of movement of the upper holder is chosen to be 1.4 x 10-4 s^{-1}.

A three-dimensional deformation scheme with high contact stresses was modeled; therefore, the Siebel friction factor was used. According to [47, 52], the friction factor f was taken equal to 0.4. The contact surfaces of the tooling were specified by the impermeability condition.

The simulation was carried out without taking into account the increase in metal temperature from the thermal effect caused by plastic deformation, and with a constant time step equal to 0.05 s. The solver of sparse matrices with iterations according to the Newton-Raphson method was used. The finite element model described the motion of a continuous medium based on the Lagrange approach.

Below are maps of the distribution of strains and stresses for CG and UFG cylindrical samples, the geometry of which, when constructed, coincides with the geometry of experimentally deformed samples.

Figure 5.2. shows that the distribution of strains in a cylindrical sample with a coarse-grained structure is non-uniform. According to the distribution map, the greatest deformation is achieved in the central part of the sample, which corresponds to theoretical and experimental data. According to this simulation, it can be concluded that the deformation does not occur in the surface zone, but proceeds from the central part along the volume.

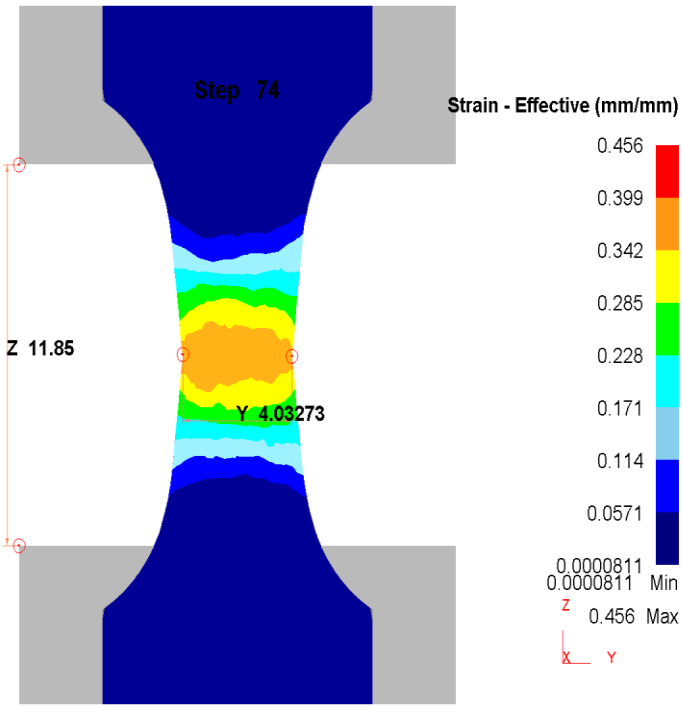

Figure 5.2. Strain distribution map of a cylindrical short-circuit specimen under tension up to deformations e=0.7.

Figure 5.3. a stress distribution map for a cylindrical image of a coarse-grained structure is presented and, according to the presented modeling, this distribution is uniform. The maximum stress values start from 202 MPa over the entire cross section, which is not very much higher than the experimental values. This difference is acceptable in terms of error.

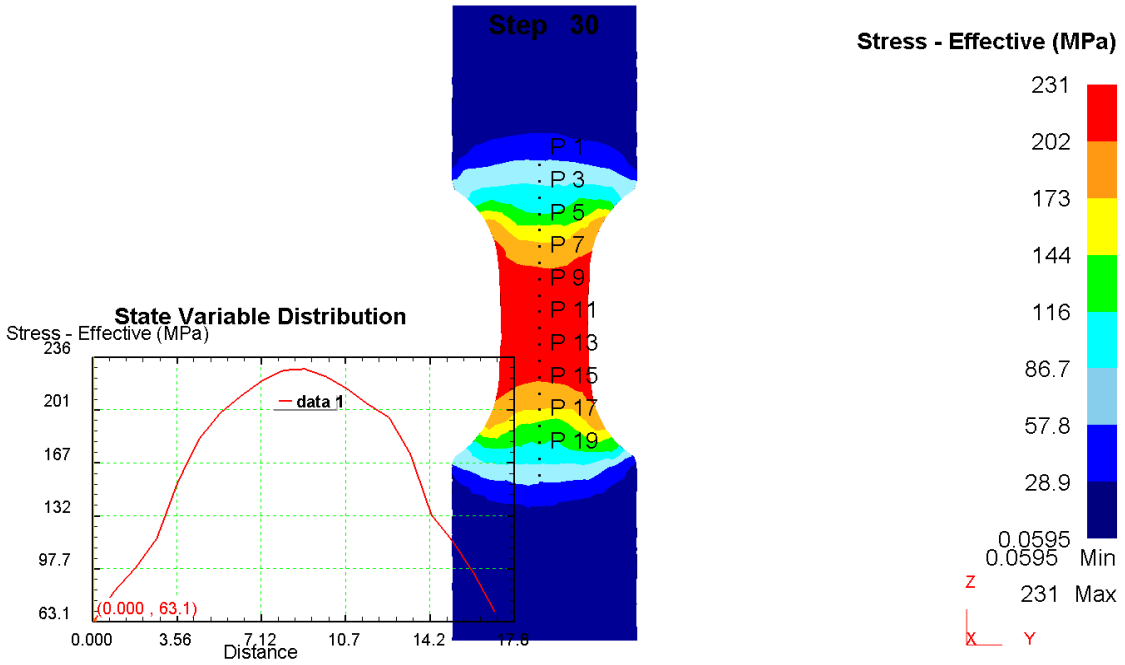

Figure 5.3. Stress distribution map for a cylindrical CG specimen under tension up to deformations e=0.7.

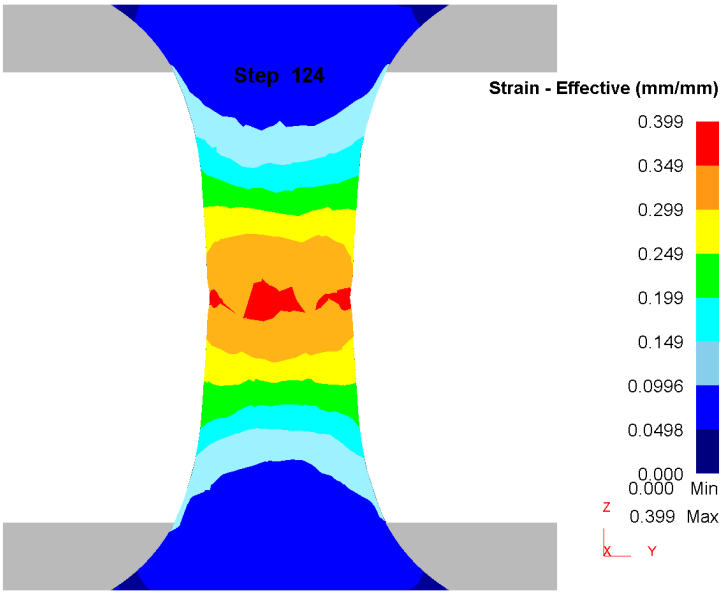

Figure 5.4. Strain distribution map of a cylindrical UFG specimen under tension up to deformations e=0.7.

In Figures 5.4. and 5.5 present similar maps of strain and stress distributions, respectively, for a cylindrical specimen of the UFG structure. Because the grain size and

other structural differences of our samples were not taken into account in the simulation, similar results were obtained: the deformation is distributed in homogeneously, and the stresses are uniform.

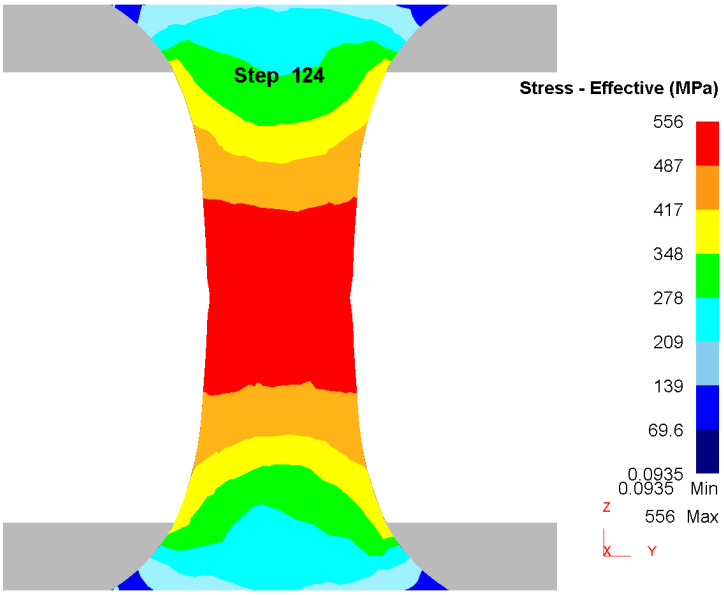

Figure 5.5. Stress distribution map for a cylindrical UFG specimen under tension up to deformations e=0.7.

The zone of pore formation in the UFG and CG states is approximately the same and corresponds to the deformation e = 0.39. It was in these zones that the formed pores in the material were revealed after deformation to e = 4; in the zones more distant from the center of the sample, no pores were observed. Therefore, this simulation is acceptable under the conditions of this problem, despite the lack of consideration of the size of the structural elements of the material.

5.2. Analysis of the growth of the true fracture stress of samples for the UFG state relative to its short-circuit state

In order to assess the influence of the structure on the fracture process and to establish the “sources of origin” of the destruction of samples, it is necessary to analyze the nucleation of pores, which symbolizes the first stage of the destruction of the material. Thus, if we have data on the calculation of critical stresses, which determine

the initiation of pores inside the material, in this case in Al-6101, under static loading, then its destruction can be predicted.

In [85], the issue of calculating critical stresses for similar copper samples under similar loading conditions was previously considered. In this case, we consider Al 6101 in the structural states: CG AA, UFG-ECAP.

A numerical calculation of the stress-strain state in tension was carried out. The methodology is based on the article [85]. We consider static loading at room temperature and a constant tensile rate. Samples are presented in three geometries and three structural states: from coarse-grained material during natural and artificial aging, and from fine-grained material obtained by the ECAP-C method [18].

Previously, a number of studies have been carried out [85.86] in order to determine the criteria for pore formation in metallic materials with particles of secondary phases. At present, the most widely used criterion is the critical stress value at the metal matrix/particle interface (Figure 5.2.1).

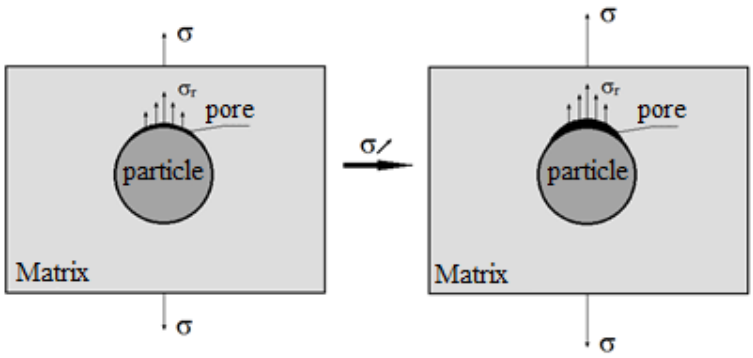

Figure 5.2.1. Matrix/particle interface. Schematic pore growth with increasing external tensile stress.

The calculation of the critical value $\sigma_r$of the stress at the metal matrix/particle interface was first carried out in [86]. The authors succeeded in deriving the pore formation criterion for rods made of coarse-grained steel and copper with a recess:

$$\sigma_m + \sigma_{eq} \geq \sigma_r, \qquad (5.2.1)$$

where $\sigma_m = \frac{1}{3}(\sigma_1 + \sigma_2 + \sigma_3)$– hydrostatic stress;

$\sigma_{eq} = \frac{1}{\sqrt{2}}\sqrt{(\sigma_1 - \sigma_2)^2 + (\sigma_2 - \sigma_3)^2 + (\sigma_3 - \sigma_1)^2}$ - equivalent stress,

$\sigma_1, \sigma_2, \sigma_3$ are the principal stress values.

To explain the growth of the true fracture stress of samples during the formation of the UFG state, taking into account previously known approaches we can offer the following model. As mentioned earlier, according to the Hall-Petch law, a decrease in grain size entails an increase in strength and yield strength as a result of ECAP-C, since As the grain size decreases, more stress is needed for the flow of dislocations. Why does the true fracture stress of the samples increase during the formation of the UFG structure? This question requires additional discussion.

The formation of pores and subsequent fracture during deformation in the 6101 alloy is formed on inclusions Al-Fe[17.46]. In matters of porosity, it is common Zener-Strote model, which is a criterion for pore formation, according to which a pore on a particle is formed under the condition that the stress reachesσsome critical valueσ_r:

$$\sigma > \sigma_r \qquad (5.2.2.)$$

However, the Hall-Petch law gives a different explanation (Figure 5.2.2): the dislocation cluster model shows that slip in a polycrystal passes from one grain to the next through its boundary, while the stress concentration near the head of the dislocation clusters that were formed at the boundary , exceeds some critical valueτ_{With}. The number of dislocations in a pile of length L under a uniform shear stressτdetermined by the value $n=\alpha_1\pi L\tau/GbL$, where$\alpha_1$is a coefficient close to unity, which depends on the nature of the dislocations, and G is the shear modulus and bL is the Burgers vector of the dislocation. [27]. The stress that acts on the head dislocation is defined as$\tau_l=n\tau$, hence$\tau_l=\alpha_1\pi L\tau^2/GBL$. We assume that the friction force acts on the dislocations in the slip plane$\tau_0$and the dislocation pileup length L is defined as half the grain size d; as a result, an equation is obtained for determining the shear stress, which gives the flow of dislocations through the grain boundary:

$$\tau = \tau_0 + \left(\frac{2Gb_L\tau_c}{\alpha_1\pi}\right)^{1/2} d^{-1/2}, \qquad (5.2.3)$$

where τ_c- critical valueτ_1, at which the head dislocation crosses the boundary. The flow of dislocations through the grain boundary just determines the yield strength of macroplastic deformation of a polycrystalline material.

The number of dislocations n accumulating at the grain boundary during microdeformation increases with increasing grain size d, therefore, the stress increasesτon the border. Then the movement of dislocations into a neighboring grain occurs at a certain critical stress$\tau_{With}=\tau_1+\tau$, Whereτis defined as the external stress on the sample.

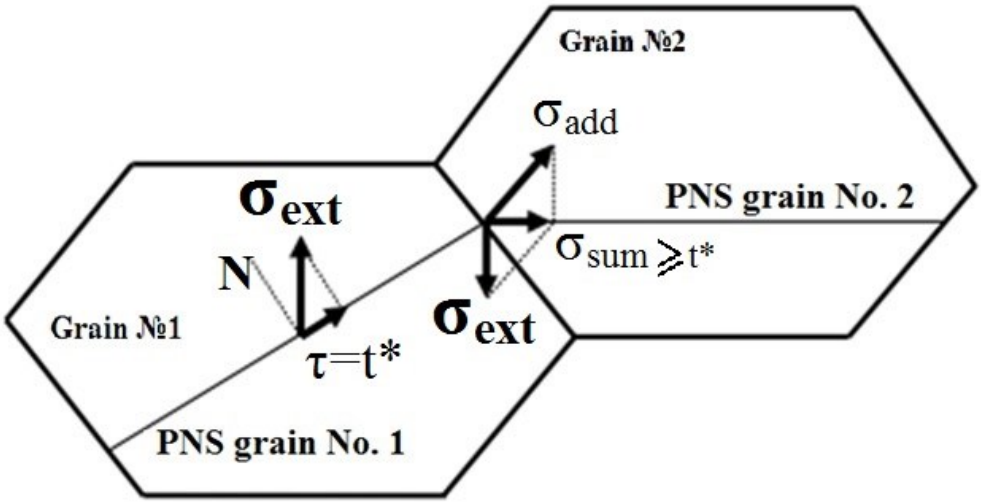

Figure 5.2.2. Scheme illustrating relay-race transmission of plastic strain in a polycrystal, which determines the Hall-Petch law.

A similar model can be made for the fracture stress (Figure 5.2.2). A certain number of dislocations np, which accumulate at the grain/particle interface, increases with the length of the dislocation path, i.e. with increasing grain size. And already at the grain/particle boundary, clusters of dislocations np give stresses$\sigma_{\rho p}$,. To reach some critical voltageσ_r, which causes a break at the material/particle interface, and form pores, it is quite applicable to use the equation from the dislocation cluster model:

$$\sigma_r \quad \sigma_{Ifail} = \sigma_c \quad - \sigma_{\rho p} \qquad (5.2.4.)$$

where $\sigma_{\rho p} = (2Gb_L\sigma_c/\alpha\pi)^{1/2}\, d^{1/2}$.

Correspondingly, the smaller the grain size, the more dislocations of lower density accumulate at the particle/grain interface, and the greater the external stress is required for rupture at the matrix–particle grain boundary and the formation of a pore.

Destruction will occur through the formation and association of pores arising during deformation, and, therefore,σ_r defines σ_{Ifail} as:

$$\sigma_r \sim \sigma_{Ifail} \quad (5.2.5.)$$

It can be concluded that the simultaneous application of the dislocation pileup model with the Zener-Strote model helps to explain the increased true fracture stress for ultrafine-grained materials.

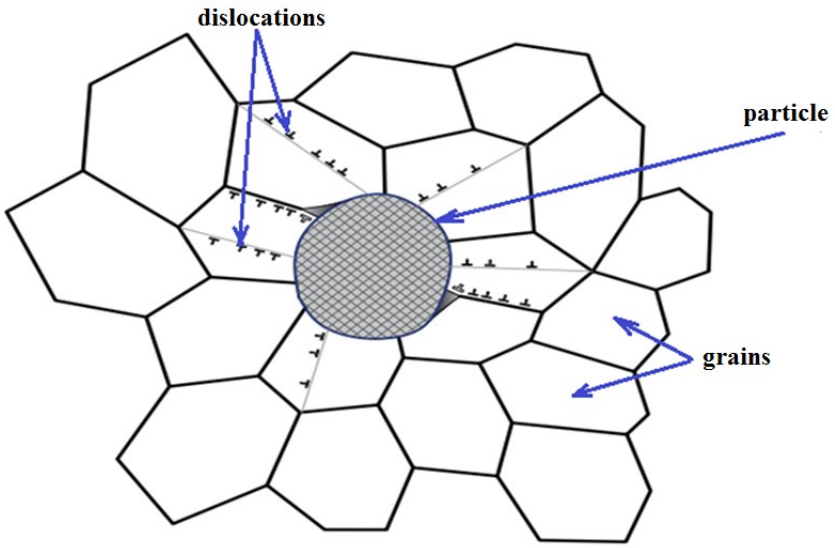

Figure 5.2.3. Diagram explaining the increased true fracture stress in materials with a smaller grain size.

Treatment of alloy 6101 by the ECAP-C method leads to an increase in strength and yield strength by 25% relative to the standard heat treatment of a coarse-grained alloy. The true strain to failure of the 6101 alloy in both states, taking into account the measurement error, is the same. In this case, the true fracture stress of samples with UFG with treatment is noticeably higher than the true fracture stress of samples in the short-circuit state. An explanation is proposed for the growth of the true fracture stress of samples during grain refinement based on the compilation of the Hall-Petch law and the Zener-Strote model: the smaller the grain size, the more dislocations accumulate at the particle/grain interface, and the greater the external stress is required to break at the interface. matrix grains - particle and pore formation

Publications on the research topic:

[87] Magomedova, DK Critical stresses determination in case of pores formation for coarse and ultra-fine grained Al-6101 under static tension / Magomedova DK, Efimov,

MA, Churakova, AA, Ryabokon, DV, Gunderov, DV // Journal of Physics: Conference Series. 2020. 1474. 012027.

[88] Gunderov, DV True fracture stress of UFG samples of Al 6101 alloy / Gunderov DV, Gunderova SD, Magomedova DK // Letters on Materials. 2022.12(4s). pp. 424-427.

[89] Polyakov, A.V. Influence of grain boundary misorientations on the mechanical behavior of a near-α Ti-6Al-7Nb alloy processed by ECAP // Polyakova V.V., Semenova I.P., Polyakov A.V.,Magomedova D.K., Huang Y, Langdon T.G.// Materials Letters. 2017. 190(4). pp 256-259.

Conclusion

In this study, the relationship between changes in the microstructure of the Al 6101 alloy of the Al-Mg-Si system and its physical and mechanical properties after deformation-heat treatment was looked into.

- On the basis of this investigation, it was confirmed that the grain structure of alloy Al 6101 is refined by Equal-Channel Angular Pressing (ECAP) to increase its strength.
- The analysis of the fracture surface spectrum reveals that the fracture surface of the CG state contains a high proportion of Fe, which is significantly higher than the alloy's average Fe content. Large particles of Al-Fe intermetallides are the regions of pore nucleation and subsequent fracture of the CG state under tension, and the fracture surface is rich in Fe-based intermetallide particles.
- The ECAP-C state fracture surface has a significantly lower Fe content. This is explained by the fact that the fracture character changes after ECAP-C, as the regions of pore nucleation and subsequent fracture may be structural elements such as areas of higher dislocation density, defects formed during ECAP-C, and iron intermetallides that no longer play a significant role in the formation of the fracture surface.
- Al-Fe intermetallic particles with a high content are located on the fracture surface at the depth of the fracture pits of Al alloys in the CG state under tension, and the fracture spectrum reveals an increased Fe content that is many times higher than the alloy's average Fe content. In other words, the previously fixed increased Fe content in the fracture pits in the fracture region is not due to SEM measurement error but to the increased content of Al-Fe particles at the bottom of the fracture pits, since Al-Fe particles are more likely to form pores during the initial stage of fracture and, consequently, after fracture.
- ECAP-C treatment refines the Al-Fe particles in alloy 6101 from 7 to 2 m, relative to the alloy's state in its coarse-grained form.
- This material's elongation to failure is confirmed to be 50% for all varieties of structures and geometries. The specimens with UGS structures exhibit 25% greater strength and 50% greater tensile strength than those in the CG state. Grain boundary

hardening - the result of grain refinement during ECAP-C - is added to dispersion hardening (the result of natural weathering after ECAP-C).

- The true fracture stress in the UFG state is significantly greater than the true fracture stress in the CG state.
- The enhanced resistance to crack formation in the UFG state determines the increased true stress of fracture.
- The fracture surface has a homogeneous structure that corresponds to uniaxial tension and is pitted. The extent of pits on the fracture surface of CG state specimens can be estimated to be up to 10 μm , while that of UFG state specimens can be estimated to be up to 5 μm. This suggests that a large number of microdefect nucleation centers participated in the UFG state during fracture.
- The particles of the coarse-grained state measure 3–7 m, while those of the UFG state measure 1-2 m. The area with the highest concentration of pores corresponds to the area with the greatest stress concentration.
- The qualitative analysis of experimental and theoretical results suggests that the critical stress value of pore formation in UFG material is higher.
- The increase in yield strength and related ultimate strength in the UFG state is explained by the Hall-Petch law: as grain size decreases, a greater external stress is required to set dislocation flow.

References

[1] Aluminium alloys / Moscow, Metallurgy, 1979.

[2] Murayama, M. Pre-precipitate clusters and precipitation processes in Al-Mg-Si alloys [Text] / M. Murayama, K. Hono // Acta Materialia. - 1999. - Vol. 47. - P. 1537-1548.

[3] Corrosion Aluminium /Ch. Vargel - ELSEVIER, 2004.

[4] Salischev, G. A. Formation of submicrocrystalline structure in titanium and titanium alloys and their mechanical properties / G. A. Salischev, R. M. Galeev, S. P. Malysheva [et al] // Metal science and technical treatment of metals. - 2006. - № 2. - C. 19-26.

[5] Segal V. M. Processes of plastic metal structure formation / Segal V. M., Reznikov V. I., Kopylov V. I. [et al.] //-Minsk: Nauka i tekhnika, 1994. -C. 232.

[6] Valiev R. Z. Nanostructured materials obtained by severe plastic deformation /Valiev R. Z., Aleksandrov I. V. // - M.: Logos, 2000. - C.272.

[7] Valiev, R. Z. Nanostructuring of Metals by Severe Plastic Deformation for Advanced Properties / R. Z Valiev // Nature Mater. - 2004. - 3. - p. 511.

[8] Equal-channel angular pressing of metallic materials: achievements and directions of development / Thematic collection of articles edited by V.M. Segal, S.V. Dobotkin and R.Z. Valiev // Metals, 2004. № 1,2.

[9] Murashkin, M.Y. Structure and mechanical properties of aluminum alloy 6061 subjected to equal-channel angular pressing in parallel channels/ m.y. murashkin, e.v. bobruk, a.r. kil'mametov, r.z. valiev. // The physics of metals and metallography, 2009.

[10] Murashkin, M.Y. Enhanced mechanical properties and electrical conductivity in ultrafine-grained Al alloy processed via ECAP-PC [Текст] / M.Y. Murashkin, I. Sabirov, V.U. Kazykhanov, E.V. Bobruk, A.A. Dubravina, R.Z. Valiev // Special Issue: Nanostructured Materials; Guest Editor: Yuntian T Zhu. 13 ed: Springer Netherlands; 2013. -pp. 4501-4509.

[11] Fakhretdinova, E.I. Structure and properties of aluminum alloy system Al-Mg-Si after processing by the method of Multi-ECAP-Conform / E.I. Fakhretdinova, E.V.

Bobruk, G.Yu. Sagitova , G.I. Raab// Letters on materials. -2015. -No.5 (2). -pp. 202-206.

[12] Bobruk, E.V. Aging behavior and properties of ultrafine-grained aluminum alloys of Al-Mg-Si system [Текст] / E.V. Bobruk, M.Y. Murashkin, V.U. Kazykhanov, R.Z. Valiev // Reviews on Advanced Materials Science. - 2012. - Vol. 31. - pp. 109-115.

[13] Mavlyutov, A.M. Effect of annealing on microhardness and electrical resistivity of nanostructured SPD aluminium [Текст] / A.M. Mavlyutov, A.S. Bondarenko, M.Y. Murashkin, E.V. Boltynjuk, R.Z. Valiev, T.S. Orlova // Journal of Alloys and Compounds. - 2017. - Vol. 698. - pp. 539-546.

[14] Raab, G.J. Continuous processing of ultrafine grained Al by ECAP–Conform [Текст] / G.J. Raab, R.Z. Valiev, T.C. Lowe, Y.T. Zhu // Materials Science and Engineering: A. - 2004. - Vol. 382. - pp. 30-34.

[15] Valiev, R.Z. A nanostructural design to produce high-strength Al alloys with enhanced electrical conductivity [Текст] / R.Z. Valiev, M.Y. Murashkin, I. Sabirov // Scripta Materialia. - 2014. - Vol. 76. - pp. 13-16.

[16] Strength and fracture mechanisms of bulk nanostructured metallic materials: textbook / [G.V. Klevtsov et al.] Ufa State Aviation Technical University. - Ufa: UGATU RIC, 2016.

[17] Dobatkin, S. V. Severe Plastic Deformation of Steels: Structure, Properties and Techniques / S. V. Dobatkin. // In Investigations and Applications of Severe Plastic Deformation, T. C. Lowe and R. Z. Valiev (eds.), Kluwer Publishers, NATO Science Series. - 2000. - 3(80). - pp. 13.

[18] Raab, G. I. Equal-channel angular pressing according to "Conform" scheme of long nanostructured semi-finished products from titanium / G. I. Raab, R. 3. Valiev // Forging and stamping production. The metal forming. -2008. -№1. - C. 21. [19] Susai, K. S. Development of aluminium wire for automotive harnesses [Текст] / K.S. Susai, S. Takamura // 60th IWCS Conference.

[20] Horikoshi, T. Development Of Aluminium Alloy Conductor with High Electrical Conductivity and Controlled Tensile Strength and Elongation [Текст] / T.

Horikoshi, H. Koruda, M. Shimizu, S. Aoyama // Hitachi Cable Review. - 2006. - Vol. 25. - pp.218.

[21] Nasu, S. Defects and phases of iron in aluminium [Текст] / S. Nasu, U. Gonser, R.S. Preston // Journal de physique Colloque. - 1979. - Vol. 41 Colloq C-1. - pp. 385-386.

[22] Aluminium and aluminium alloys. Chemical composition and form of blanks. //Part 3: Chemical composition and shape of articles. Chemical composition and form of products Effective date 01.10.2019.

[23] Aluminium and aluminium alloys. Extruded rods, tubes and profiles. // EN 755-2, Part 2. Mechanical properties. Date of entry into force: 01.10.2016/.

[24] Fadeeva, V.I. Amorphization and crystallization of Al-Fe alloys by mechanical alloying [Текст] / V.I. Fadeeva, A.V. Leonov // Materials Science and Engineering A. - 1996. - Vol. A206. - pp. 90-94.

[25] Tcherdyntsev, V.V. Effect of deformation by high pressure torsion on the phase composition and microhardness of mechanically alloyed and rapidly quenched Al-Fe alloys [Текст] / V.V. Tcherdyntsev, S.D. Kaloshkin, E.A. Afonina, I.A. Tomilin, Y.V. Baldokhin, E.V. Shelekhov et al // Defect and Diffusion Forum. - 2003. - Vol. 216-217. - pp. 313-322.

[26] Sasaki, T.T. Microstructure and mechanical properties of bulk nanocrystalline Al-Fe alloy processed by mechanical alloying and spark plasma sintering [Текст] / T.T. Sasaki, T. Ohkubo, K. Hono // Acta Materialia. - 2009. - Vol. 57. - pp. 3529-3538.

[27] Jablonski, M.K. New Aluminium Alloys For Electrical Wires Of Fine Diameter For Automotive Industry [Текст] / M.K. Jablonski, B. Smyrak // Archives Of Metallurgy And Materials. - 2009. - Vol. 54. - pp.671-676.

[28] Jablonski, M. Effect of iron addition to aluminium on the structure and properties of wires used for electrical purposes [Текст] / M. Jablonski, T. Knych, B. Smyrak // 5th International Conference on Light Metals Technology, July 19, 2011 - July 22, 2011. Luneburg, Germany: Trans Tech Publications Ltd; 2011. pp. 459-462.

[29] Kim, D.H. Structure and decomposition behaviour of rapidly solidified Al-Fe alloys [Текст] / D.H. Kim, B. Cantor // Journal of Materials Science. - 1994. - Vol. 29. - pp. 2884-2892.

[30] Shabashov, V.A. Mössbauer study of dissolution of iron aluminides under severe cold deformation [Text] / V.A. Shabashov, I.G. Brodova, A.G. Mukoseev, V.V. Sagaradze, A.V. Litvinov // Izvestia RAN, Physical Series. - 2005. - Ч. 10. - С. 1459-1464.

[31] Shabashov V.A. Structural transformations in Al-Fe system under severe plastic deformation [Text] / V.A. Shabashov, I.G. Brodova, A.G. Mukoseev, V.V. Sagaradze, A.V. Litvinov // Physics of metals and metallurgy. - 2005. - Ч. 4. - С. 66-67

[32] Cantor, B. Precipitation of equilibrium phases in vapour-quenched Al-Ni, Al-Cu AND Al-Fe ALLOYS [Текст] / B. Cantor, R.W. Cahn // Journal of Materials Science. - 1976. - Vol. 11. - pp. 1066-1076.

[33] Meagher, C. Increasing the Strength and Electrical Conductivity of AA6101 Aluminum by Nanostructuring Rilee / C. Meagher,Mathew L.// Hayne,Julie DuClos,Casey F. Davis,Terry C. Lowe,Tamás Ungár&Babak ArfaeiLight Metals, - 2019. -pp 1507–1513/

[34] Oravan, E. In Dislocations in Metals. / E. Oravan. – New York: AIME, 1954. – pp.103.

[35] Behr, L.B. Temperature-time-conversion (TTC) and temperature-time-property (TTP) aging diagrams of thermally hardenable aluminium alloys. Their use for development of stepwise aging regimes/ L.B. Behr. - Materials Science News. Science and Technology. - 2016. Series 3. - C. 46-61.

[36] Kolachev B.A. Metallurgy and heat treatment of non-ferrous metals and alloys: textbook for universities, 4th ed./ B.A. Kolachev, V.I. Elagin, V.A. Livanov / - MISIS Publishing House, Moscow, 2005.

[37] Behr, L.B. On the stages of aging of aluminum alloys / L.B. Behr. - Technology of Light Alloys, 2013, P. 66-76.

[38] Raab, G. I. Development of scientific bases of intensive plastic deformation technologies and creation of equipment according to the scheme of equal-channel

angular pressing for obtaining ultrafine-grained metal semi-finished products: Abstract of doctoral thesis ... D. in Technical Sciences: 05.03.05 / Raab George Iosifovich. - Ufa. 2009. - C. 36.

[39] Valiev, R.Z. Volumetric nanostructured materials [Text] / R.Z. Valiev, I.V. Aleksandrov // Moscow: Akademkniga. - 2007.

[40] Ultrafine-grained materials prepared by severe plastic deformation / ed. by R. Z. Valiev. - Annales de Chemie. Science des Materiaux, 1996. - 21(6-7). - pp. 369.

[41] Valiev, R.Z. A nanostructural design to produce high-strength Al alloys with enhanced electrical conductivity [Текст] / R.Z. Valiev, M.Y. Murashkin, I. Sabirov // Scripta Materialia. - 2014. - Vol. 76. - pp. 13-16.

[42] Langdon, T. G. Using equal-channel angular pressing for refining grain size / T. G. Langdon, M. Furukawa, M. Nemoto, Z. Horita // JOM. -2000. - 52(4). - pp. 30.

[43] Valiev, R. Z. Principles of equal-channel angular pressing as a processing tool for grain refinement / R. Z. Valiev, T. G. Langdon // Progress in Materials Science. - 2006.-51.-pp. 881.

[44] Segal, V. M. Severe plastic deformation: simple shear versus pure shear / V. M. Segal // Materials Science and Engineering. - 2002. - A 338. - pp. 331.

[45] Segal, V. M. Slip line solutions, deformation mode and loading history during equal channel angular extrusion / V. M. Segal // Materials Science and Engineering. - 2003. - A 345. - pp. 36.

[46] Valiev R. Z. Development of equal-channel angular pressing for obtaining ultrafine-grained metals and alloys / Valiev R. Z. 3. - Metals, 2004. №1. C. 15-22.

[47] Segal, V. M. Materials processing by simple shear / V. M. Segal // Mater. Sci. Eng.-1995.-A 197.-pp. 157.

[48] Valiev R.Z. Equal-channel angular pressing of long billets / Raab G.I., Valiev R.Z. - Tsvetnaya metallurgy, 2000. № 5. C. 50-53.

[49] Mackenzie, P.W.J. ECAP with back pressure for optimum strength and ductility in aluminium alloy 6016. Part 1: Microstructure. / Mackenzie, P.W.J.; Lapovok, R. // Acta Mater. – 2010. 58. pp. 3198–3211.

[50] Newman, W. Alchemical Laboratory Notebooks and Correspondence / Newman W., Principe L. M. — University of Chicago Press, 2004.— pp.352.

[51] GOST 6996-66. BIBLIOGRAPHIC REFERENCE. Welded joints (2008)// Methods for determination of mechanical properties. Moscow: Standartinform.

[52] GOST 1497-84. INTERSTATE STANDARD. Metals. Tensile test methods, 1986.

[53] Ivanova V. S. In the book: Structure and properties of heat-resistant metallic materials/ Ivanova V. S., Vorobyov N. A. //. Moscow, Nauka. -1967. C.- 249-255.

[54] Islamgaliev, R. K. Strength and fatigue of ultrafine grained aluminium alloy AK4-1 / Islamgaliev R. K. K., Nesterov K. M., Khafizova E. D., Ganeev A. V., Golubovsky E. R., Volkov M. E. // Bulletin of UGATU. 2012. T. 16, № 8 (53). C. 104-109.

[55] Valiev R. Z. Fracture mechanism and martensitic transformations in plastic zones of austenitic steel AISI 321 after equal-channel angular pressing / Valiev R. Z. Z., Klevtsova N. A., Klevtsov G. V., Feseniuk M. V., Kashapov M. R., Abramova M. M. -Formation and Fracture of Materials, 2010. № 10.- C. 14-18.

[56] Klevtsov, G. V. Strength and fracture mechanism of nanostructured AK4-1 aluminum alloy in a wide temperature range / G. V. Klevtsov, R. Valiev. Z., Islamgaliev R. K., Klevtsova N. A., Kashapov M. R., Feseniuk M. V. - Fundamental Researches, 2012. № 3. Ч. 2. - C. 391-395.

[57] Oding, N. A. Metallurgy and fuel"/ Oding, N. A. Liberov Y. P.// "Proceedings of the USSR Academy of Sciences, OTN. -1964.T № 6. -C. 125-128.

[58] Hall-Petch Law (nanomechanics)// Nanometr (date of accession: 01.08.2010).

[59] Carlton, C. E. What is behind the inverse Hall-Petch effect in nanocrystalline materials? E., Ferreira P. J. / Acta Materialia.- 2007. V. 55. -pp. 3749-3756.

[60] Trefilov V. I. Physical basis of strength of refractory metals / Trefilov V. I., Milman Yu. V., Firstov S. A. - Kiev, "Naukova Dumka", 1975. -C.315.

[61] Kolachev, B.A. Physical and chemical mechanics of materials / B.A. Kolachev, A. Malkov. V., Sedov V. I. - 1975. T. 11. № 6. C. 7-12.

[62] Nurislamova, G. Nanostructure and related mechanical properties of an Al-Mg-Si alloy processed by severe plastic deformation/ Nurislamova, G.; Sauvage, X.; Murashkin, M.; Islamgaliev, R.; Valiev, R. //Philos. Mag. Lett.- 2008.- 88.-pp. 459-466.

[63] Drits, M.E. "Science"/Dritz, M. E. et al. // .-1973.

[64] Mondolfo, L.F. Aluminum Alloys: Structure and Properties / Mondolfo, L.F.// Butterworths: London, UK. -1976.

[65] Hanson D., Gayler M. J. Inst. Met./ Hanson D., Gayler M. J. // -1923. Vol.29. - pp. 491 - 493.

[66] Magomedova, D.K. Influence of grain size and second phase particles on the process of void initiation / Magomedova D.K., Murashkin, M. Y.// Journal of Physics: Conference Series. 2018. 991. 1. 012055.

[67] Magomedova, D.K. Technique development for conducting mechanical tests to study the pore formation process in case of material fracture / Magomedova D.K., Efimov M.A., Murashkin, M. Y. // AIP Conference Proceedings. 2018. 1959. 070021.

[68] Sauvage, X. Optimization of electrical conductivity and strength combination by structure design at the nanoscale in Al-Mg-Si alloys / Sauvage, X.; Bobruk, E.V.; Murashkin, M.Y.; Nasedkina, Y.; Enikeev, N.A.; Valiev, R.Z.// . Acta Mater. 2015. 98. pp. 355–366.

[69] Sauvage, X. Atomic scale investigation of dynamic precipitation and grain boundary segregation in a 6061 aluminium alloy nanostructured by ECAP/ Sauvage, X.; Murashkin, M.Y.; Valiev, R.Z.//. Kov. Mater. Met. Mater. 2011. 49. pp.11–15.

[70] Sabirov, I. Nanostructured aluminium alloys produced by severe plastic deformation. New horizons in development. / Sabirov, I.; Murashkin, M.; Valiev, R.Z.// Mater. Sci. Eng. A. 2013. 560. pp.1–24.

[71] Sha, G. Strength, grain refinement and solute nanostructures of an Al-Mg-Si alloy (AA6060) processed by high-pressure torsion/ Sha, G.; Tugcu, K.; Liao, X.Z.; Trimby, P.W.; Murashkin, M.Y.; Valiev, R.Z.; Ringer, S.P. // Acta Mater. -2014. 63.- pp. 169–179.

[72] Bobruk, E.V. Enhanced strengthening in ultrafine-grained Al-Mg-Si alloys produced via ECAP with parallel channels/ Bobruk, E.V.; Kazykhanov, V.U.; Murashkin, M.Y.; Valiev, R.Z.// AEM.- 2015.

[73] Roven, H.J. Dynamic precipitation during severe plastic deformation of an Al-Mg-Si aluminium alloy/ Roven, H.J.; Liu, M.; Werenskiold, J.C. // Mater. Sci. Eng. A. -2008. -483–484. -pp. 54–58.

[74] Kashyap, B.P. Plastic flow properties and microstructural evolution in an ultrafine-grained Al-Mg-Si alloy at elevated temperatures/ Kashyap, B.P.; Hodgson, P.D.; Estrin, Y; Timokhina, I.; Barnett, M.R.; Sabirov, I.// Metall. Mater. Trans. A .-2009.- 40.- pp. 3294–3303.

[75] Hatch, J.E. Aluminum: Properties and Physical Metallurgy/ Hatch J.E. // ASM International: Metals Park.- 1984.- OH.- USA.

[76] Magomedova D.K., Efimov M.A., Ryabokon D.V. // Technical program and theses of school of young scientists "STRUCTURE AND PROPERTIES OF HIGH-EXTROPHY SPEEDS AND COATINGS". -2019 .- C.43-44.

[77] Magomedova, D.K. Mechanical behavior of coarse- and fine-grained Al-6101 samples of different geometry under tension / Magomedova D.K., Gunderov, D. V., Efimov, M. A. // IOP Conference Series: Materials Science and Engineering. 2019. 672.

[78] Magomedova D.K. Stress distribution under static tension of cylindrical samples of fine-grained and coarse-grained aluminum alloy 6101 / Magomedova D.K., Churakova, A.A. // Nanoindustrii.- 2021.- Issue 1.

[79] Magomedova D. K. Effect of geometry and grain size on the mechanical properties of Al 6101 under static tension of cylindrical samples / Magomedova D. K. // Materials. Technologies. Design, Ufa. Ufa. - Vol. 3.- № 2(4). - C.20-24.

[80] Magomedova, D.K. The dependence of mechanical properties of Al-6101 alloy on geometry of the samples with a groove during tensile tests / Magomedova D.K., Gunderov D. V. , Mavlutov A. M. // Journal of Physics: Conference Series. -2021.- 1967(1).- 012023.

[81] Magomedova D.K. Influence of grain size on process of grain formation in AL-6101 / D.K. Magomedova // THE FOURTH INTERNATIONAL RESEARCH FORUM "NEW MATERIALS AND PROSPECTIVE TECHNOLOGIES" -2018.- Volume 1.- P. 319-321.

[82] Magomedova, D. K. The study of mechanical properties and fracture surface of cylindrical samples Al-6101 under static tension / Magomedova, D. K., Churakova, A. A., Gunderov, D. V. // Proceedings of the VII International Conference "Actual problems of continuum mechanics".- 2021.- P.167-171.

[83] Magomedova, D.K. Investigation of mechanical properties and fracture surface of cylindrical samples Al-6101 under static tension / Magomedova D. K., Churakova A. A., Gunderov D. V. // Journal of Physics: Conference Series. -012023.

[84] Magomedova D. K. Influence of structure of alloy Al 6101 on pore formation under static tension as a structural change during deformation / Magomedova D. K. // Materials. Technologies. Design, Ufa. Ufa.- 2022.- Vol. 4.- No.1(7).- C. 24-29.

[85] Argon, A.S. Distribution of plastic strain and negative pressure in necked steel and copper bars / Argon A.S., Im J., Needleman A. // Metallurgical Transactions. - April 1975.- 824. -Volume 6A.

[86] Im ,J. Cavity formation from inclusions in ductile fracture/ J. Im, R. Safoglu // Metallurgical Transactions. -1975.- A.- Volume 6.- pp. 825.

[87] Magomedova, D.K. Critical stresses determination in case of pores formation for coarse and ultra-fine grained Al-6101 under static tension / Magomedova D.K., Efimov, M. A., Churakova, A. A., Ryabokon, D. V., Gunderov, D. V. // Journal of Physics: Conference Series.- 2020. - 1474. - 012027.

[88] Gunderov, D.V. True fracture stress of UFG samples of Al 6101 alloy / Gunderov D.V., Gunderova S.D., Magomedova D.K. // Letters on Materials.- 2022.- 12(4s).- pp. 424-427.

[89] Polyakov, A.V. Influence of grain boundary misorientations on the mechanical behavior of a near-α Ti-6Al-7Nb alloy processed by ECAP // Polyakova V.V., Semenova I.P., Polyakov A.V.,Magomedova D.K., Huang Y, Langdon T.G.// Materials Letters. 2017. 190(4). pp 256-259.